^{11}Be SPECTROSCOPY FROM THE FIRST INVERSE KINEMATICS TRANSFER REACTION MEASUREMENT BY THE AT-TPC IN SOLARIS

By

Michael Zachary Serikow

A DISSERTATION

Submitted to
Michigan State University
in partial fulfillment of the requirements
for the degree of

Physics—Doctor of Philosophy

2025

ABSTRACT

As evidenced by the field's existence surpassing a 100 years, nuclei are varied and immensely complex. New accelerator facilities are now able to produce rare isotopes that seldom appear in nature and whose properties must be measured to lead to a better understanding of the nuclear force. These facilities have naturally facilitated the need to switch to inverse kinematics. This, coupled with the low intensity of rare isotope beams, has lead to the creation of a new type of detector called an active target. These detectors are especially well-suited for rare isotope beams due to their high luminosity, theoretical 4π solid angle coverage, and ability to determine the vertex of a nuclear reaction.

One such active target is the Active Target-Time Projection Chamber (AT-TPC) housed at the Facility for Rare Isotope Beams. This thesis reports the results from the first transfer reaction measurement by the AT-TPC in inverse kinematics. Specifically, ^{11}Be spectroscopy was performed via the $^{10}\mathrm{Be}(d,p)$ reaction. ^{11}Be is an ideal candidate for such a commissioning measurement as the structure of its low-lying states is well known. Despite this, the parity of its fourth excited state at 3.40 MeV has been debated. This thesis measured the angular distributions of all states in ^{11}Be up to and including this state. Their spectroscopic factors were derived and compared to values in the literature and theoretical shell-model interactions. Reasonable agreement was found between the derived factors, literature, and YSOX interaction. Although the coverage of the 3.40 MeV state's angular distribution is too limited for a definitive parity assignment, it and the spectroscopic analysis tentatively support a positive parity. The implications of this assignment on the rotational structure, $0d_{3/2}$ single-particle energy, and spin-orbit splitting of the $0d$ orbitals in ^{11}Be are explored.

ACKNOWLEDGMENTS

Beginning in my childhood, my parents invested much of their time into not only my academic success but my future. My mom worked all day at home as a bookkeeper while simultaneously keeping the house clean, cooking for the family, and helping me study. Even in the evening after working since early in the morning, I remember her often quizzing me in preparation for exams. She worked so hard but never complained because she loved her family. I love her and them, too.

The University of Notre Dame set the trajectory for my nuclear physics tenure. Tan Ahn was pivotal in providing meaningful research experiences and a friendship that will last a lifetime. I am continually surprised by the strength of my connections I made there. I hope I can return a fraction of what has been given to me. It was also during this time that I studied under three different and remarkable physicists: Alexandre Zagoskin, Harvey Brown, and Craig Woody. I am sorry that I am not the best in keeping in touch. I will never forget you.

As a graduate student at Michigan State University, my advisor Daniel Bazin has given me more opportunities, connections, and experiences than I could have ever imagined. Growing up in northern Indiana among the cornfields never sowed the possibility of traveling the world and encountering people so like myself in cultures so different. Indiana is a special place, though. During my last two years at Michigan State, I become friends with Gordon McCann. The impact of his knowledge and guidance are not belied by his short period in my life, indicative of the magnitude of his impact.

To my fiancée Amy Dao and her family: I love you all. You fueled my ability to perform. You supported my well-being. These actions are eternal.

TABLE OF CONTENTS

LIST OF TABLES

LIST OF FIGURES

CHAPTER 1

INTRODUCTION

This chapter provides an introduction to experimental nuclear physics with beams. This is not an attempt to provide a complete picture, neither from a historical nor physics standpoint, but to create a story that this thesis will add to. As such, topics relevant to this thesis will be succinctly discussed as needed to understand the main results of this work.

1.1 Experimental nuclear physics with beams

For over a century, many nuclear physics experiments have been conducted using the same simple setup: a beam of nuclei is made to collide with a target of nuclei. Although how these beams and targets are produced, their stability, etc. have evolved over time, this core idea has not. The reason for this is because the collision of two nuclei in a nuclear reaction is analogous to a microscope, which is of course used to illuminate the structure of things too small for us to see with our naked eyes. As such, nuclear physicists turned to nuclear reactions to study the structure of nuclei. To make another analogy, just as the debris from a car crash reveals information about the two vehicles that collided, the products of a nuclear collision reveal information about the nuclei that collided. Such information includes the collision probability, what nuclei are produced, the spatial distribution of the products, their energies, their lifetimes, etc. Nuclear theory can use these observables to infer nuclear structure such as the distribution of protons and neutrons and their individual energies.

Experimentally, nuclear reactions can be divided into two categories: normal and inverse kinematics. Normal kinematics are the reaction type that have historically dominated laboratory use. In normal kinematics, the target is the heavier nucleus and the beam is the lighter nucleus. The main reason for their popularity was that nuclear physicists had been primarily interested in the study of stable nuclei. Stable nuclei can be made into targets that do not radioactively decay. Thus, one has the convenience of hitting this stable target with a beam made of a light nucleus that is relatively easy to produce. Another benefit of using a light nucleus is that its nuclear reactions are much easier to theoretically model as there are less degrees of freedom than reactions between

two heavy nuclei (this is still true in inverse kinematics). However, with the shift towards studying rare radioactive nuclei, this approach fails. It is not possible to build a target that would endure an experiment if it is made of a nucleus that has a lifetime many orders of magnitude smaller than a single second.

To overcome the limitation of building a radioactive target, the radioactive nucleus can be turned into the beam itself. When the beam nucleus is heavier than the target nucleus, the reaction is referred to as occurring in inverse kinematics. The production of rare-isotope beams is significantly more difficult than light stable beams and is only due to amazing advances in rare-isotope beam science in the past few decades that is now spearheaded by the Facility for Rare Isotope Beams at Michigan State University.

It is the age of rare-isotope beams. This is the context for my thesis work.

1.2 Active targets for radioactive beams

Radioactive beams provide unique challenges for the study of their constituent nuclei. First, they often are low intensity due to the complexity of producing such a beam. This is of experimental importance because it means that they must impinge upon thick targets if there is to be any hope of observing a reasonable amount of collisions in a reasonable amount of time. The problem with traditional passive targets is that by increasing their thickness to compensate for the low intensity of the beam, a larger and larger uncertainty in the energy of the collision is introduced as there is no way to know how deep in the target the reaction occurred. Another problem with passive targets is that it is impractical if not extremely expensive to surround the target with enough detectors to cover a large solid angle while simultaneously achieving a high angular resolution.

An elegant solution to the challenges posed by radioactive beams and passive targets is an active target. An active target serves as both the target of the nuclear reaction and detection medium. Gases are used for this purpose since an impinging beam can react with it as the target while the gas can simultaneously be used as an ionization chamber for detecting the reactants and products of the reaction. Active targets solve the problem of target thickness because the reaction vertex can be accurately determined in the gas by reconstructing the particle tracks using their electron-ion

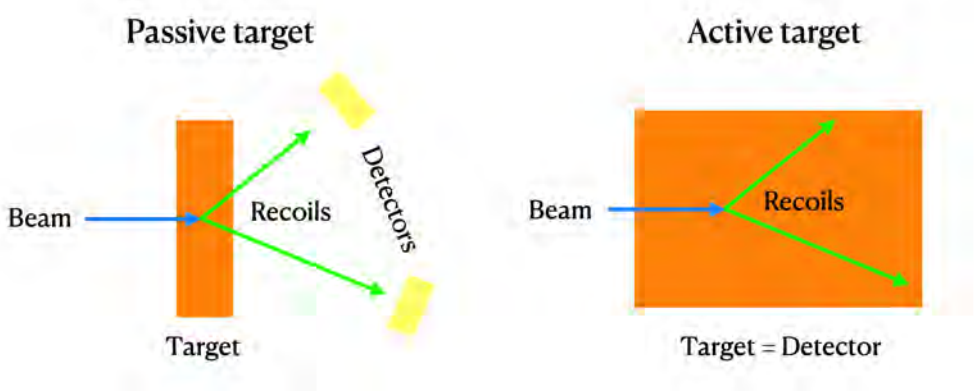

Figure 1.1 Comparison between a traditional passive target and an active target. Courtesy of Daniel Bazin.

pairs created ionizing the gas. Active targets theoretically provide a 4π solid angle coverage as the detecting gas completely encompasses the nuclei in the reaction.

Active targets are phenomenal detectors for use with rare-isotope beams, but they are not without their own drawbacks. Gas detectors are known to be slow since they must drift the electron-ion pairs generated by the ionizing radiation to a measuring device at a boundary of the detector. The time needed for electrons to drift these distances is long (electron drift velocities are on the order of $cm/\mu s$), thus the detector can only accept low beam intensities without experiencing a large pile up of events. There often is the problem that the gas, while chosen to study a certain nuclear reaction, is not very good for detection, i.e. it may not have a desirable amplification factor when used with micro-pattern gaseous detectors (MPGDs), too slow a drift velocity, etc. There is also the issue of energy loss. Because the reaction can occur anywhere in presumably a large gas volume, the incoming beam will experience significant energy loss. Depending on the depth in the detector, the reaction channel of interest may not be energetically allowed or lose detection efficiency. Finally, as will be evident from the analysis, data generated from active targets is quite non-trivially related to the physical observables of interest.

1.3 Active-Target Time Projection Chamber

The Active-Target Time Projection Chamber (AT-TPC) was designed and developed at the former National Superconducting Cyclotron Laboratory (NSCL) at Michigan State University, now known as the Facility for Rare Isotope Beams (FRIB). It is the marriage of an active target, as

described in Section 1.2, with a time projection chamber. As a time projection chamber, the AT-TPC records the tracks of particles inside of it. It is the active target used in this work and now will be described.

The AT-TPC is shown in Fig. 1.4. It is a large cylindrical active target with an approximately 1 m long active volume denoted in the figure by green. Its radius is 29.2 cm. The active volume houses the target gas. As shown, a beam of nuclei is shot into the active volume. The beam nucleus then has the length of the active volume to undergo a nuclear reaction with a nucleus of the gas. If a reaction occurs, the products fly off into the gas, ionizing it and creating electron-ion pairs along their paths. The AT-TPC is only interested in the electrons, not the ions, which encode information related to both the location and energy loss of the particle where they were created.

A uniform electric field is made between the cathode at one end of the active volume and the anode at the other to drift the liberated electrons towards the readout plane underneath the MPGDs (labeled in the image as "micromegas"). The uniformity of the field is ensured by a field cage made of rings connected to each other in series with a 20 MΩ resistor between consecutive pairs. In this way, the rings and resistors form a series of voltage dividers that create a uniform potential gradient. The active volume is encapsulated by an outer cylinder and the space between the two is filled with nitrogen gas. The outer cylinder prevents access to the high-voltage cathode while the gas prevents sparking between the two. The nitrogen gas is at a lower pressure than the target gas to ensure any leaks in the active volume result in gas flowing into the outer volume. This helps keep the target gas pure. The gases are controlled by the intricate gas handling system of the AT-TPC that continuously recycles the target gas to remove impurities.

The liberated electrons enter the MPGDs where the avalanche process occurs and orders of magnitude more electrons are emitted and induce signals on the readout plane. It is vital that the number of electrons is increased as the number of liberated electrons in the active volume is too low to create a detectable signal on the readout plane. A pad that records a signal reveals the x- and y-coordinates of the particle at the time those liberated electrons were created. Measuring how long those electrons took to induce a signal on the pad, with knowledge of how fast electrons drift

in the gas, is used to calculate the z-position of the particle at that time. A variety of MPGDs in different configurations can be used with the AT-TPC. This experiment used two multilayer thick GEMs (M-THGEMs) stacked on top of a micromegas. The readout plane is shown in Fig. 1.2 and comprised of 10,240 equilateral triangular pads. As the figure illustrates, the inner hexagonal region is made of smaller triangular pads with a height of 0.5 cm while the larger outer triangular pads have a height of 1 cm. The inner hexagonal region covers where the beam enters the AT-TPC and reacts with the gas, thus it contains the reaction vertex and the beginning of the products' tracks. A finer granularity is desirable in this region to better extract important kinematic variables such as the polar angle.

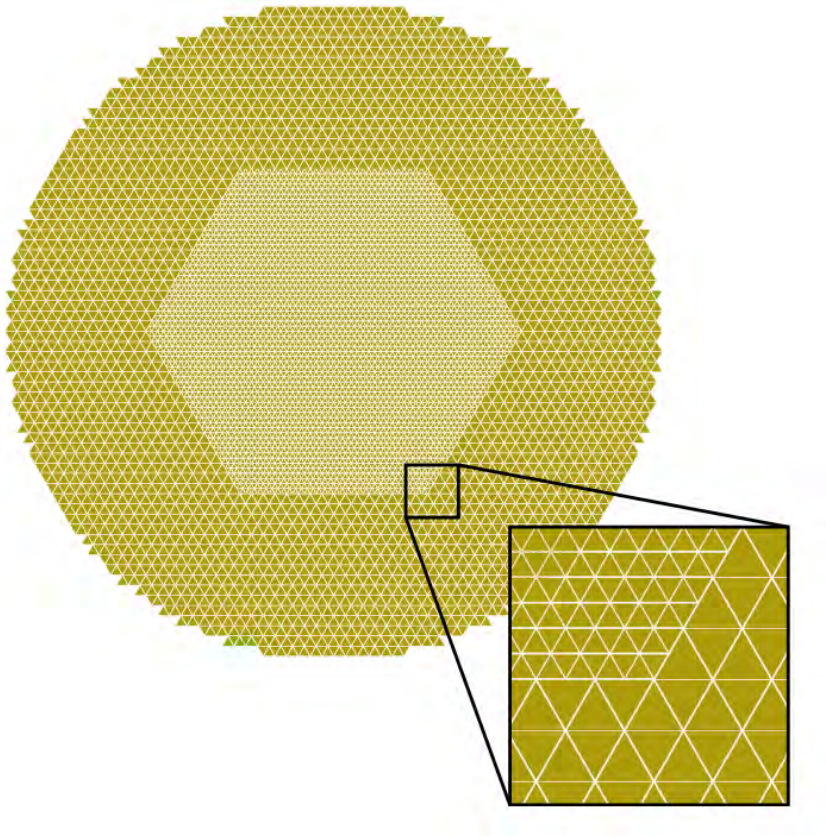

Figure 1.2 Illustration of the pad plane. All 10,240 pads are triangular, with the inner pads being smaller than the outer pads. Reproduced with permission from [2].

The AT-TPC uses the General Electronics for TPCs (GET) to readout the signals induced by the electrons on the readout plane. GET is a hierarchical data collection system, as seen in Fig. 1.3, where each pad on the readout plane is connected to a specific AGET chip, AsAd board, and CoBo

module. The specifics of GET will not be elaborated on further in this work unless necessary, but reference [5] provides more details.

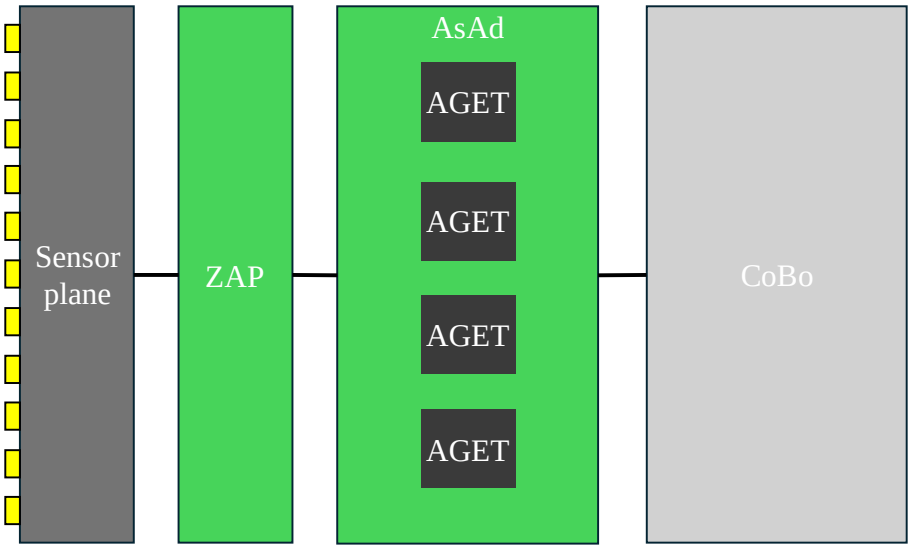

Figure 1.3 Illustration of GET electronics hierarchy connected to the sensor, or pad, plane that the electrons induce signals on.

1.3.1 Coupling the AT-TPC with the SOLARIS solenoid

The AT-TPC was previously described as a stand-alone detector. It certainly can be used this way to study nuclear reactions. However, there are considerable advantages in coupling the AT-TPC to a solenoid magnet as done for this experiment. The AT-TPC was placed inside the SOLARIS solenoid in the ReA6 vault of the NSCL. SOLARIS is a former MRI magnet that can reach a maximum field strength of 4 T. Fig. 1.5 shows SOLARIS with the AT-TPC inside.

The benefits of a solenoid come from the addition of a magnetic field that curves the trajectories of the charged particles in the AT-TPC. The trajectory lengths of the particles are effectively increased because they can spiral longer distances before hitting the walls of the AT-TPC. A longer trajectory means more information is gathered about the particle in the detector. The magnetic field also allows for the energy of particles to be directly calculated from the magnetic rigidity measured from their tracks. This is a significant advantage of the solenoid as without it the energy

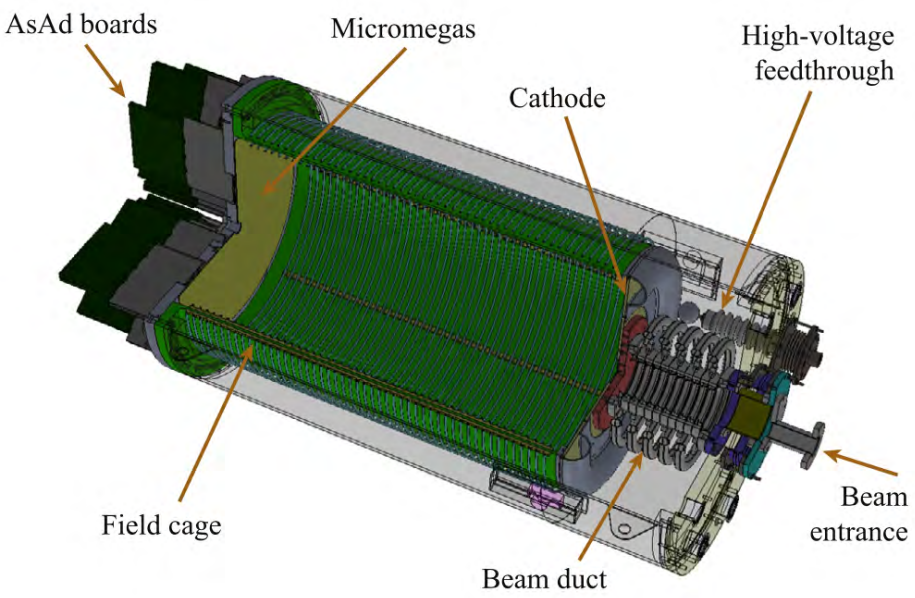

Figure 1.4 Schematic of AT-TPC with some key components indicated. Reproduced with permission from [2].

of a particle would be calculated from its range in the gas, which cannot be done if the particle does not stop in the AT-TPC active volume. Ensuring that particles deposit their entire energy in the detector requires careful tuning of other experimental parameters, such as the gas pressure, that may restrict the sensitivity of the AT-TPC to certain nuclear reactions and are altogether avoided by the solenoid. The magnetic field curves the trajectories of the electrons ionized by the particles as well. This has a focusing effect on the electrons as they drift through the detector and reduces their transversal diffusion. This is because their radii of curvature are extremely small in the fields typically used.

1.4 Physics with the AT-TPC

As previously described, the AT-TPC is well designed to study exotic radioactive nuclei. There is an assortment of physics measurements that can be extracted with the AT-TPC including differential and total cross sections, excitation functions, excitation energy spectra, etc. This section will provide a cursory overview of the physical measurements that were extracted from the experiment of this thesis using the AT-TPC.

Figure 1.5 Picture of the AT-TPC within the SOLARIS solenoid at FRIB. Courtesy of Daniel Bazin.

1.4.1 Cross section

Perhaps the most fundamental and important concept of nuclear reactions is the nuclear cross section. Cross sections are important for a multitude of reasons not least being that they provide a concrete observable for comparison with theoretical models.

In this context, the cross section is the probability that a nuclear reaction will occur. We can

define the experimental cross section by imagining a beam of nuclei impinging on a target. In this scenario, suppose that we have perfect detectors that always tell us when any reaction between the beam and target occurs. Let R represent the number of reactions per time per target volume hit by the beam. Suppose we also know the beam intensity I that has units of nuclei per area per time. We could say that the probability that a reaction occurred is given by the simple ratio R/I that has units of inverse length. This definition makes intuitive sense because we have simply taken the ratio of the number of reactions to the number of possible reactions. The problem with this definition is that the cross section is a property of the bulk target and not its constituent nuclei. This is clear by considering that we could arbitrarily change the cross section by adding or subtracting material to the target, hence altering R while keeping I the same. We thus need to convert this macroscopic cross section to a microscopic cross section. We want the cross section to be a property of the target nuclei. This can be accomplished by dividing out the number of nuclei in the volume of the target seen by the beam, denoted by n. The reaction cross section is then given by

$$\sigma = \frac{R}{In} \tag{1.1}$$

and has units of area. The condition that R includes all reactions can be restricted to only include certain reaction channels.

Typically our detectors will not be able to fully detect all reactions that occur because they do not cover a solid angle of 4π, hence some reaction products do not hit them. In this case, we introduce the differential cross section $d\sigma/d\Omega$. To derive this quantity, we acknowledge that R is now a function of the angles θ and ϕ measured with respect to the reaction vertex. Taking the derivative with respect to the solid angle yields

$$\frac{d\sigma}{d\Omega} = \frac{1}{In}\frac{dR(\theta,\phi)}{d\Omega}. \tag{1.2}$$

The azimuthal symmetry of scattering means that ϕ is irrelevant for extracting physics. We thus

restrict the differential solid angle $d\Omega$ to cones by integrating over all ϕ. This results in

$$d\Omega = \int_0^{2\pi} \sin\theta d\phi d\theta,$$
$$d\Omega = 2\pi \sin\theta d\theta. \tag{1.3}$$

Plugging Eq. 1.3 into Eq. 1.2 yields

$$\frac{d\sigma}{d\Omega} = \frac{1}{2\pi In \sin\theta} \frac{dR(\theta)}{d\theta}. \tag{1.4}$$

An actual experiment cannot measure angles to infinite precision, so we will recast the differential cross section as

$$\frac{d\sigma}{d\Omega} = \frac{1}{2\pi In \sin\theta} \frac{R(\theta, \Delta\theta)}{\Delta\theta} \tag{1.5}$$

where it is understood that $R(\theta, \Delta\theta)$ is the reaction rate measured by our detector at the nominal angle θ that also includes counts from the angles around it in the range $\pm\Delta\theta/2$. The differential cross section in this form is commonly called the angular distribution.

The cross section also has an energy dependence that can be made explicit by taking the derivative of Eq. 1.4 with respect to it. This experiment was only concerned with the differential cross section given by Eq. 1.5, though.

1.4.2 Spectroscopy

Nuclei are inherently quantum systems. They have excited states with quantized energies that carry quantum numbers such as spin and parity. This is evident from the shell model, the oldest and historically most successful nuclear structure theory. The basic shell model assumes the nucleons in a nucleus experience a mean-field force. Solving the Hamiltonian for this mean field gives rise to discrete quantum levels for the nucleons to populate, with large gaps in energy separating different shells (analogous to the shells electrons fill in atoms). In nuclear physics, a filled shell corresponds to a magic number, and the shell model was the first to accurately reproduce those known. Magic numbers are experimentally known from a variety of data. Fig. 1.6 shows the difference between experimental two-nucleon separation energies and those predicted by the semi-empirical mass model. In the figure, the data shows structure at the magic numbers.

Nuclear reactions provide a tool for extracting observables that can be used to benchmark nuclear structure models like the shell model. This includes measuring the spectrum of excited state energies of a nucleus, which is called spectroscopy. The spectroscopic method used depends on the nuclear reaction, measured nucleus, and detector. Here we discuss the missing-mass method used by the AT-TPC for the two-body reaction $a + b \rightarrow A + B$. Let a be the beam with momentum only in one direction and b be the stationary target. In the equations that follow the K are kinetic energies, m rest masses, and p momenta. Assume we are interested in the spectroscopy of nucleus B but only detect nucleus A. [1] The excitation energy E_{ex} of B is

$$E_{ex} = (m_B^* - m_B)c^2 \tag{1.6}$$

where m_B^* is the rest mass of B in its excited state and c is the speed of light. With the relativistic energy-momentum relation Eq. 1.6 becomes

$$E_{ex} = \sqrt{E_B^2 - (p_B c)^2} - m_B c^2 \tag{1.7}$$

where E_B is the total energy of B. Conservation of energy and momentum in the reaction requires

$$E_B = K_a + m_a + m_b - K_A - m_A, \tag{1.8}$$

$$p_B^2 = p_a^2 + p_A^2 - 2p_a p_A \cos\theta \tag{1.9}$$

where θ is the laboratory scattering angle of nucleus A. Notice that insertions of Eqs. 1.8 and 1.9 into Eq. 1.7 allow for the determination of E_{ex} without measuring m_B^*, hence the term "missing mass". The missing-mass method is powerful because it can measure the excitation energy of unbound states that prevent a direct measurement of their mass.

1.4.3 Spectroscopic factors

While the basic shell model is quite successful in describing stable nuclei near the magic numbers, it requires modifications for the vast majority of nuclei. The nuclear force has residual interactions the mean-field potential does not capture that play an important role in these nuclei. For

[1] This may sound contrived, but it is accurate for the AT-TPC. In inverse kinematics, the heavy product nucleus is constrained to small forward scattering angles where the pad plane is insensitive as described in Section 2.1. The light product nucleus does not have this constraint and is much easier to detect.

example, such residual interactions include the pairing and tensor forces. In this context, nuclear theory has attempted to modify and/or supplement the mean-field force to find potentials that better suit a nucleus or group of nuclei. To characterize the effectiveness of a particular nuclear model, spectroscopic factors were introduced. A spectroscopic factor $S_\alpha^{(+/-)}$ is the probability that adding ($^+$) a nucleon in state α to the nucleus χ^{A-1} or subtracting ($^-$) a nucleon in state α from the nucleus χ^{A+1} yields the nucleus ψ^A with A nucleons. Mathematically,

$$S_\alpha^+ = |\langle \chi^{A-1} | a_\alpha | \psi^A \rangle|^2, \quad S_\alpha^- = |\langle \psi^A | a_\alpha | \chi^{A+1} \rangle|^2. \tag{1.10}$$

The spectroscopic factors can be related to the theoretical nucleon single-particle energy (SPE) of α via

$$\epsilon_\alpha = \sum_N S_\alpha^+ (E - E_N) + \sum_n S_\alpha^- (E_n - E) \tag{1.11}$$

where E, E_N, and E_n are the energies of nuclei ψ^A, χ^{A-1}, and χ^{A+1}, respectively [6]. The summations are over the set of either all particle (χ^{A+1}) or hole (χ^{A-1}) nuclei. SPEs are one of the most important quantities in nuclear structure and Eq. 1.11 relates them to experimentally found excited states from spectroscopy.

Spectroscopic factors are not experimentally observable but can be experimentally derived. Imagine we have an ensemble of nuclei. We now add or subtract a nucleon in state α to each of them and record the final state of each resulting nucleus. From this information we could determine the probability to produce a certain final state and compare this to some model's spectroscopic factor prediction. The experimental way to add or subtract a nucleon to a nucleus is through pick-up or stripping reactions, respectively. For a reaction the probability to populate a certain state is given by its cross section. We thus suspect that this cross section is related to the spectroscopic factor. However, this cross section is not directly related to a pure nuclear matrix element and has kinematic contributions from scattering [7]. Theoretically, if we have a good handle on the reaction theory, we can divide out the kinematic dependence from our experimental cross section and be left with the pure spectroscopic factor. The spectroscopic factor is then related to the cross section

through

$$S_{experiment} = \frac{\sigma_{experiment}}{\sigma_{theory}} \tag{1.12}$$

where $S_{experiment}$ is the experimentally deduced spectroscopic factor, $\sigma_{experiment}$ is the experimental cross section, and σ_{theory} is the purely kinematic theoretical cross section (i.e. it involves no nuclear structure). Typically σ_{theory} is calculated using a reaction model like the distorted-wave Born approximation (DWBA). Eq. 1.12 makes apparent that $S_{experiment}$ depends on the nuclear reaction model used to calculate σ_{theory}, again illustrating that spectroscopic factors are not physically observable. Despite this, they have proven to be a powerful tool for examining nuclear structure, in particular when making relative comparisons with theory.

1.4.4 Angular momentum transfer in pick-up and stripping reactions

Pick-up and stripping reactions belong to a class of reactions called direct reactions and more specifically transfer reactions when the incident energy is close to the Fermi energy. Direct reactions are characterized by the nuclear reaction taking place at the surface of the nucleus over a very short period of time, on the order of 10^{-22} s [3]. It turns out that the angular distribution for a pick-up or stripping reaction reveals the quantized angular momentum of the transferred nucleon. The transferred angular momentum is a key quantity in these types of reactions as it can then be used to deduce the spin and parity of the nucleus that gained or lost a nucleon in the reaction. The following is a widely used semi-classical calculation that illustrates how the angular distribution is related to the transferred angular momentum and closely follows the treatment given by Krane [3].

Consider a stripping reaction where an incident nuclei with momentum $\vec{p}_a$ hits a target nucleus and transfers one nucleon to it. Denote the momentum of the transferred nucleon as $\vec{p}$ and the momentum of the outgoing nucleus that lost the nucleon as $\vec{p}_b$. See Fig. 1.7 for the geometry of the collision. The angular momentum of the transferred nucleon L is given by the classical formula

$$\vec{L} = \vec{R} \times \vec{p}$$

where $\vec{R}$ is the radial vector from the center of the target nucleus to the collision point. Because this is a direct reaction, we will assume that the transfer of the nucleon occurs at the surface of the

nucleus, i.e. $\vec{R}$ and $\vec{p}$ are perpendicular. This leads to

$$|\vec{L}| = |\vec{R}||\vec{p}|.$$

Quantizing the angular momentum yields

$$l\hbar = |\vec{R}||\vec{p}| \tag{1.13}$$

where l is the angular momentum quantum number and $\hbar$ is the reduced Planck constant. By conservation of momentum

$$\vec{p_a} = \vec{p} + \vec{p_b}$$

$$|\vec{p}|^2 = |\vec{p_a}|^2 + |\vec{p_b}|^2 - 2|\vec{p_a}||\vec{p_b}|\cos\theta \tag{1.14}$$

where θ is the angle of the scattered nucleus that lost a nucleon to the target. We can insert Eq. 1.13 into the left-hand side of Eq. 1.14 to result in a relation between the scattering angle and transferred angular momentum. We therefore expect that the angular distributions for pick-up and stripping reactions should contain information on the transferred angular momentum. This is seen in Fig. 1.8 where the value of the transferred angular momentum greatly influences the location of the first peak in each angular distribution and its overall shape. DWBA calculations are used to calculate the angular distributions in the figure. These are completely quantum-based calculations unlike the semi-classical example given and form the standard method for calculating the transferred angular momentum in a pick-up or stripping reaction by comparison of the calculation to the experimental cross section.

As previously mentioned, once the transferred angular momentum is determined, this information can be used in calculations related to the spin and parity of the nucleus that a nucleon was added to or subtracted from. Using the rules for the addition of angular momentum, we add the spin of the initial nucleus J_i, the angular momentum of the transferred nucleon l, and the spin of the transferred nucleon ($1/2$ for protons and neutrons) to yield

$$\left||J_i - l| - \frac{1}{2}\right| \leq J_f \leq J_i + l + \frac{1}{2} \tag{1.15}$$

where J_f is the final parity of the nucleus after a nucleon is added or subtracted. Considering that the parity of the final nucleus can only be changed by the angular momentum added to it or subtracted from it by the transferred nucleon (all nucleons have the same intrinsic parity, so this quantity does not matter for the calculation) results in the relation

$$\pi_i \pi_f = (-1)^l \tag{1.16}$$

where π_i is the parity of the initial nucleus and π_f is that of the final nucleus.

1.5 ^{10}Be + *d* experiment with the AT-TPC

The AT-TPC was used for the first time in the experiment of this thesis to measure a transfer reaction in inverse kinematics in the ReA6 vault at the former NSCL. The nuclear structure of the low-lying ^{11}Be states was investigated via the $^{10}\mathrm{Be}(d, p)$ reaction and the physics measurements described in Section 1.4 performed. ^{11}Be is an ideal nucleus for a transfer commissioning experiment because the structure of its low-lying states is well understood with many experimentally derived spectroscopic factors [1, 8, 9, 10]. The exception is its fourth excited state at 3.40 MeV whose parity is debated. A $^{9}\mathrm{Be}(t, p)^{11}$Be reaction performed by Liu *et al.* concluded that this state has a negative parity [11]. The same assignment was given by Hirayama *et al.* using ^{11}Li β-decay measurements [12]. However, Coulomb breakup of ^{11}Be on a carbon target done by Fukuda *et al.* indicated that this state has a positive parity [13]. Recent *ab initio* calculations on Be isotopes performed by Caprio *et al.* predict the 3.40 MeV state in ^{11}Be to be either the second member of the $\mathrm{K}^P = 1/2^+$ rotational ground state band if the parity is positive or the $\mathrm{K}^P = 3/2^-$ band-head if the parity is negative [14]. A positive parity is supported by the rotational analysis of Bohlen [15]. A definitive party assignment to the 3.40 MeV state would determine the rotational band it belongs to as well as the location of the $0d_{3/2}$ effective single particle energy (ESPE) in ^{11}Be.

All ^{11}Be states up to 3.40 MeV were populated in this experiment. The spectroscopic factors were derived by comparing the experimentally measured angular distributions to theoretical DWBA calculations. They were compared to those in the literature and shell-model calculations using the WBT [16], YSOX [17], and FSU [18] interactions. Generally, reasonable agreement was found with the literature and the YSOX interaction. Despite a limited angular coverage for the 3.40

MeV state, a tentative positive parity assignment was made and a lower limit for the $0d_{3/2}$ ESPE calculated. The $0d_{5/2}$ ESPE was also extracted using the 1.78 MeV state, enabling exploration of the $0d$ spin-orbit splitting in ^{11}Be and a comparison to that of the $N = 7$ isotone ^{13}C.

The success of this experiment demonstrates the ability of the AT-TPC to investigate nuclear structure via transfer reactions and opens the door to future investigations of exotic areas of the nuclear landscape using rare-isotope beams.

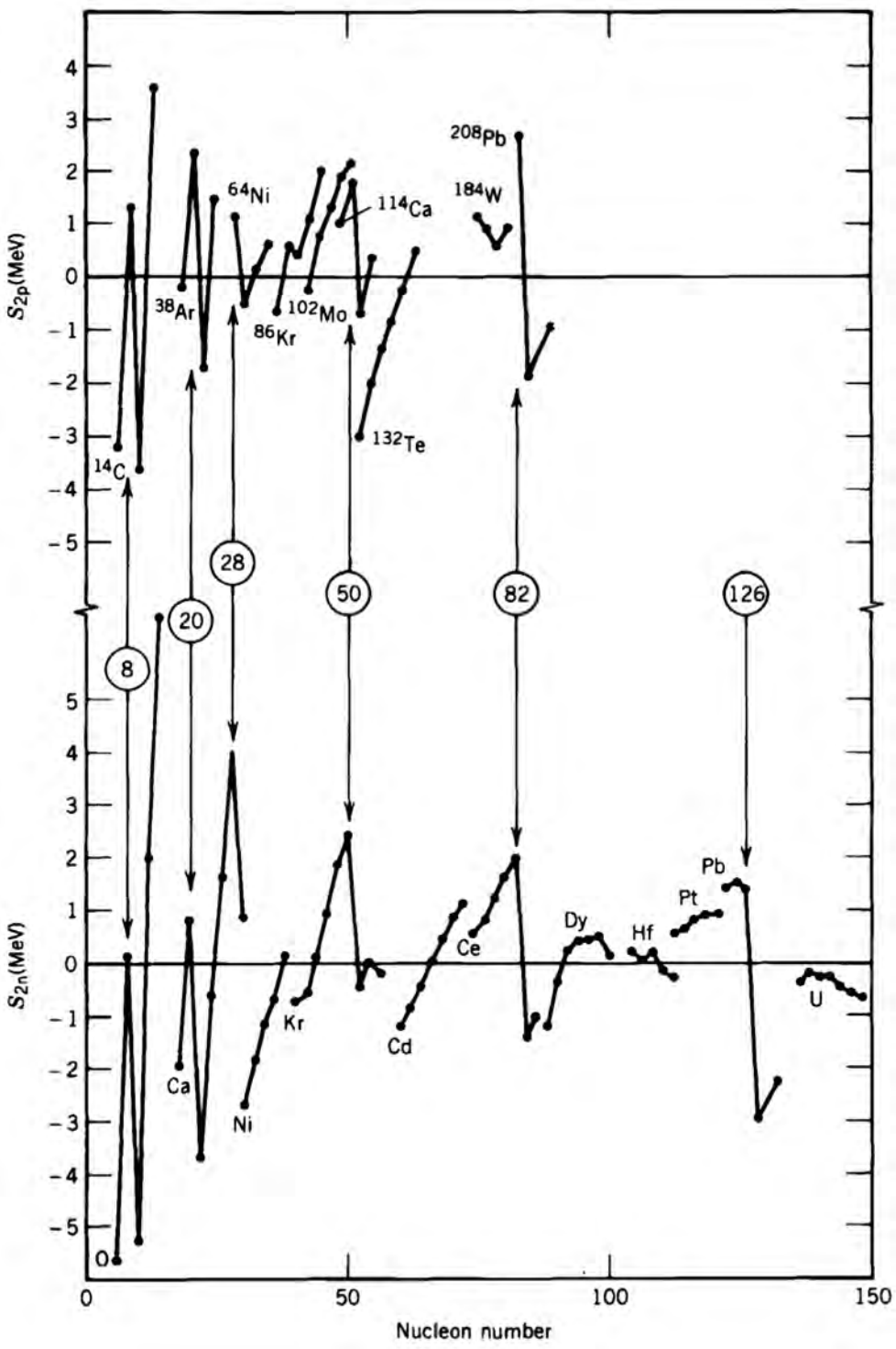

Figure 1.6 The difference between experimental two-proton and two-neutron separation energies and those predicted by the semi-empirical mass formula for sequences of isotones and isotopes, respectively. Note large spikes in the difference at the magic numbers. Reproduced with permission from [3]. Copyright © 1988 by John Wiley & Sons, Inc.

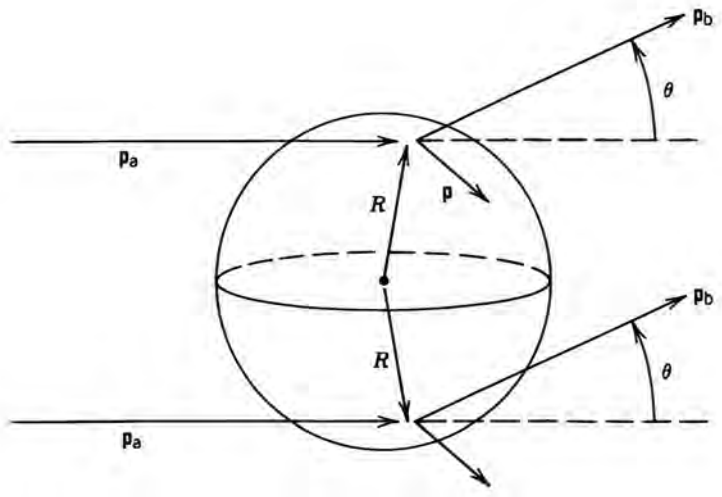

Figure 1.7 Geometry for the semi-classical stripping reaction considered. Note that collisions are shown on both sides of the target nucleus as these result in a diffraction pattern (a series of minima and maxima) in the angular distribution as seen in the experimental data shown in Fig. 1.8. Reproduced with permission from [3]. Copyright © 1988 by John Wiley & Sons, Inc.

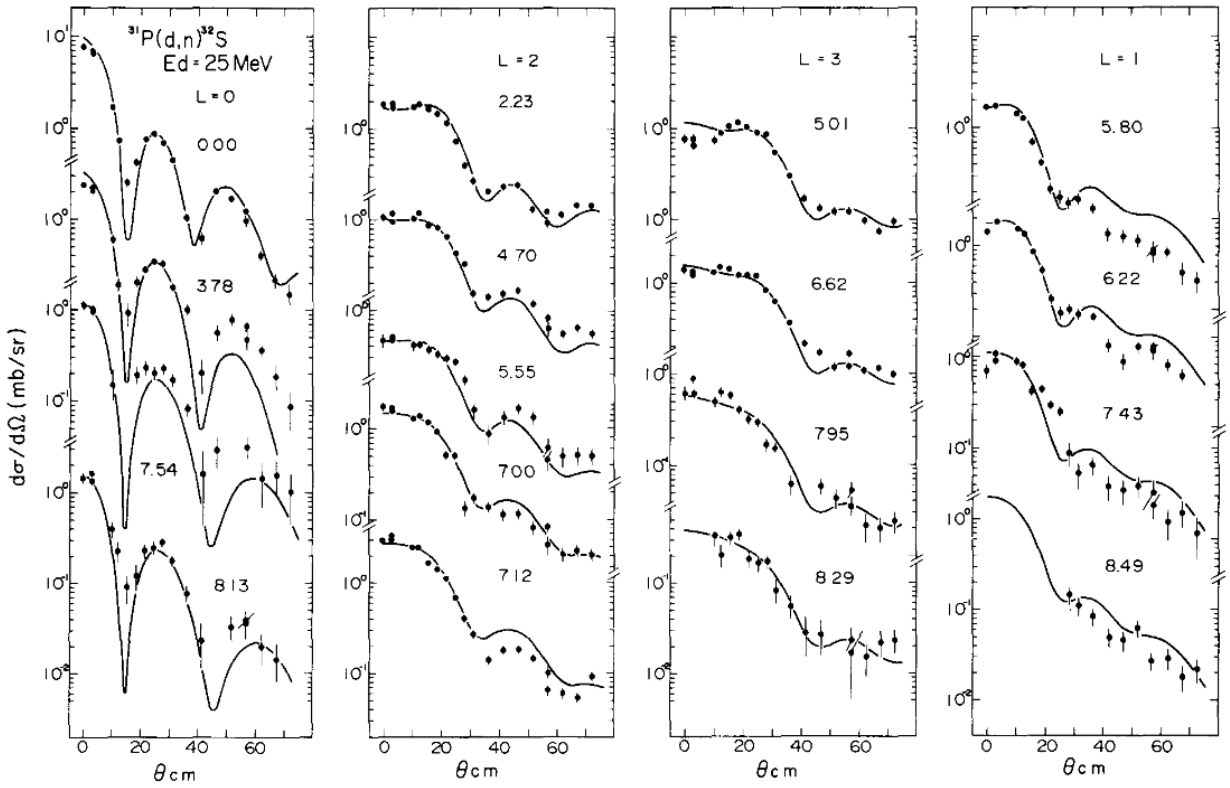

Figure 1.8 Angular distributions from the ^{31}P$(d,n)^{32}$S reaction that populate different final states in ^{32}S. They are compared to DWBA calculations with the indicated transferred angular momentum values. The transferred angular momentum is clearly correlated to the shape of the angular distribution and location of the first peak. Reproduced with permission from [4].

CHAPTER 2

EXPERIMENTAL SETUP

2.1 Setup of the AT-TPC

As described in Section 1.3.1, the AT-TPC was coupled to the SOLARIS solenoid. It was inserted and locked inside the solenoid such that the central axes of both were aligned. The AT-TPC was oriented so that the readout plane was on the far end of the detector relative to where the beam entered. The AT-TPC uses GET to record data and the only components of this hierarchical system not directly attached to the AT-TPC are the CoBos and back-end computers. Cables were used to connect the AsAd front-end boards, protruding from behind the readout plane on the AT-TPC, to the CoBos kept on a nearby rack. The same rack had power cables connected to the AsAd boards, which were connected to the pad plane via so-called ZAP boards. The "simple" ZAP board is a printed circuit board (PCB) that connects each pad on the readout plane to a grounded 100 MΩ resistor and capacitor in parallel. The purpose of this protection circuit is to prevent large currents from damaging the expensive GET modules downstream of it. The AT-TPC was also equipped with "smart" ZAP boards that provide extra functionality through an onboard Arduino Nano. The Arduino Nanos are programmed to provide a biasing voltage to the innermost pads of the pad plane that see a large amount of liberated electrons from the beam. The centers of these beam pads lie within a circle of radius 2 cm from the center of the pad plane. The biasing voltage effectively reduces the gain in this region by reducing the induced signals on the pads. Reducing the gain in the beam region is a necessity for the way the trigger was constructed, as described in Section 2.2.

The setup of the AT-TPC includes three electronics racks pictured in Figs. 2.1-2.3. One rack houses the CoBos, Mac Minis, MuTAnT module, power supplies for the AsAd front-end boards, and NIM modules for the trigger logic. The MuTAnT ensures the timestamps of each CoBo are synchronized and distributes the trigger. This is necessary because each CoBo, which corresponds to a particular region of the pad plane, has its own data acquisition system (DAQ); every CoBo starts and stops recording data on its own and saves the raw data to its own connected Mac Mini. Each Mac Mini reads a configuration file that controls the GET parameters for its electronic channels

including their sampling frequency, amplifier gain, and shaping time. These values were the same for each pad across all CoBos and are given in Table 4.2. Each CoBo has 1,024 channels, so ten CoBos were used during the experiment for the full 10,240 pads of the pad plane. An eleventh CoBo was installed to record auxiliary signals such as those from the ion chamber (IC), which is described in the next paragraph. Another rack houses the high-voltage power supply for the MPGDs and a computer. The computer controls the gas-handling system and the high voltages applied to the MPGDs and the cathode via two different programs designed by the AT-TPC collaboration. The final rack contains the cathode high-voltage power supply and the gas handling systems for the AT-TPC and IC.

The IC was installed upstream of the AT-TPC. Pictured in Fig. 2.4, it is a small cylindrical volume that houses a gas that the beam nuclei ionize. The liberated electrons are drifted to the anode via an electric field and the signal is read out. The energy loss of the beam nucleus that traveled through it is proportional to the detected signal making the IC crucial for determining the composition of the cocktail beam used in this experiment (see Section 2.4). It also provided the time reference the AT-TPC needed for accurate position reconstruction of particle tracks.

For a summary of the experimental parameters see Table 2.1.

	Parameter	Value
AT-TPC	Gas	Deuterium
	Gas pressure (Torr)	600
	Cathode voltage (kV)	60
	Field cage ring voltage (V)	100
	Micromegas voltage (V)	420
	E-trans voltage (V)	100
	M-THGEM voltage (V)	850
	Smart ZAP bias voltage (V)	130
IC	Gas	CF_4
	Gas pressure (Torr)	≈ 200
	Voltage (V)	50
SOLARIS	Magnetic field (T)	3

Table 2.1 Experimental parameters.

2.2 Trigger

A detailed schematic of the trigger is presented in Fig. 2.5 and will now be described. At the highest level, the AT-TPC uses the micromegas mesh signal to determine whether or not to record data. The liberated electrons that drift towards the micromegas, which have already been multiplied by the M-THGEM above it, induce a current on the micromegas mesh that is read out. This signal is sent through a preamplifier and shaper before a single channel analyzer (SCA) determines if the amplitude of the signal passes the set threshold to trigger data recording. As seen in Fig. 2.5, if the mesh signal generates a trigger, the resulting signal from the SCA is then stretched to form an AND gate with the signal from the IC. The IC signal is used in coincidence with the mesh signal to provide a time reference for when beam particles enter the AT-TPC. This time reference is later used to reconstruct the absolute positions of the particle. Like the mesh signal, the IC signal is passed through a preamplifier and shaper before a SCA determines if the signal amplitude is above a set threshold to trigger. If both the IC and mesh signals trigger, then the AND gate is triggered. Before this is described, let us consider why the IC signal has a delay and the mesh signal is stretched.

The AND gate between the mesh and IC signals requires their signals to overlap to trigger. In a slow gas detector like the AT-TPC, this condition will not happen without modifying the signals. The mesh signal is generated by the liberated electrons from the ionizing particles that drift through the AT-TPC at relatively slow speeds (on the order of μs/cm). Without any modification, the IC signal will always be faster than the mesh signal and no coincidence can be made between the two signals. To remedy this, a modification must be made to the timing of each signal. The IC signal is delayed by slightly more time than it would take an electron to drift the entirety of the AT-TPC. This is done because the mesh signal can be created by electrons liberated anywhere inside the AT-TPC. Delaying the IC signal ensures that the mesh signal has seen all the electrons liberated in the entire AT-TPC volume belonging to an event. This delay still does not guarantee an overlap between the IC and the mesh signals, though. It is possible to have liberated electrons slightly above the MPGDs that would cause the mesh signal to trigger the SCA much earlier than the now delayed IC signal. No coincidence would occur. To always ensure a coincidence between the two

signals, the mesh signal is stretched slightly longer than the delay on the IC signal.

The AND gate from the mesh and IC signals is proceeded by another AND gate. It checks if the GET DAQ is busy writing data from a previous event to prevent interrupting it. If the DAQ is not busy, an OR gate is encountered and the MuTAnT is triggered to record the data from the current event. If a nuclear reaction occurs and is detected, the path hitherto described is the most likely route its signals take to result in its data acquisition. We will now describe the uppermost path of Fig. 2.5 in relation to unreacted beam events and how it may be taken for nuclear reactions.

An unreacted beam event occurs when the beam particle traverses the entirety of the AT-TPC without undergoing a nuclear reaction. Recording unreacted beam events over the course of an experiment is crucial for determining the intensity of the beam to measure cross sections. As described in Section 3.2.3, they can also be used to calculate the electron drift velocity. The IC signal of an unreacted beam event will trigger but the mesh signal will not. This is because the electrons liberated by the beam induce signals on the central pads of the pad plane that have a reduced gain from the smart ZAPs. Following the IC signal after the SCA, it is still delayed and then sent to a downscaler. Because nuclear reactions have small cross sections, it is exceedingly likely that the beam will not undergo a reaction in the AT-TPC. Recording all of these unreacted beam events would overload the DAQ and be a waste of disk space as they all share the same features. To avoid this, the downscaler recorded only one in every thousand presumably unreacted beam events. “Presumably” is used as it is possible that a normal nuclear reaction may coincide with the thousandth recorded event that is downscaled and recorded as an unreacted beam event.

The signal from the downscaler goes to an AND gate that checks if the DAQ is busy writing. If not, a LEMO signal is generated that the current event is a beam event and the MuTAnT triggers, recording its data. The LEMO signal is readout by the auxiliary eleventh CoBo mentioned in Section 2.1 and uses a specially modified simple ZAP board equipped with LEMO connectors connected to an AsAd front-end board.

2.3 Ion chamber multiplicity

The ion chamber may see multiple incoming beam nuclei within a single event. Unfortunately, these events cannot be used. The AT-TPC lacked auxiliary detectors to identify the beam particle that reacted when the multiplicity was greater than one. The time reference is also always with respect to the beam particle that resulted in a trigger, as described in Section 2.2. Thus, for events with ion chamber multiplicity greater than one, the z-coordinates of the reconstructed particle trajectories may be wrong. The ion chamber multiplicity restriction was applied in the analysis, not the physical trigger.

For this experiment, the characteristics of the beam were such that it was common for the ion chamber see multiple beam nuclei for a single event. Of the 6,131,566 detected events, only $\approx 34\%$ of them had a multiplicity of one.

2.4 Beam

The ^{10}Be beam for this experiment was provided by the ReA6 facility of the NSCL. It had an energy of 9.6 MeV/u and a rate of approximately 1000-2000 pps. ^{10}B and ^{15}N contaminants were present. Fig. 2.6 is a histogram of the energy loss of the unreacted beam particles through the IC and clearly shows three nuclei in the beam.

The energy of the beam as it entered the AT-TPC was less than the 9.6 MeV/u provided by ReA6 as it lost energy traveling through the IC and the window of the AT-TPC. The pressure of the CF_4 gas used in the IC along with the thicknesses of its two windows and that of the AT-TPC were not exactly known. This made theoretical calculations of its energy loss unreliable. However, the beam energy was not a free parameter. It did not enter the analysis and was only needed for the calculation of the excitation spectra described in Section 5.3. Because the only unknown quantity in calculating the excitation spectra was the beam energy, it was adjusted until the peaks in the measured ^{11}Be spectrum aligned with their known energies (see Fig. 5.4). This required the beam energy right after the window of the AT-TPC to be approximately 9.3 MeV/u.

Figure 2.1 Rack housing the CoBos, Mac Minis, MuTAnT module, power supplies for the AsAd front-end boards, and NIM modules for the trigger logic.

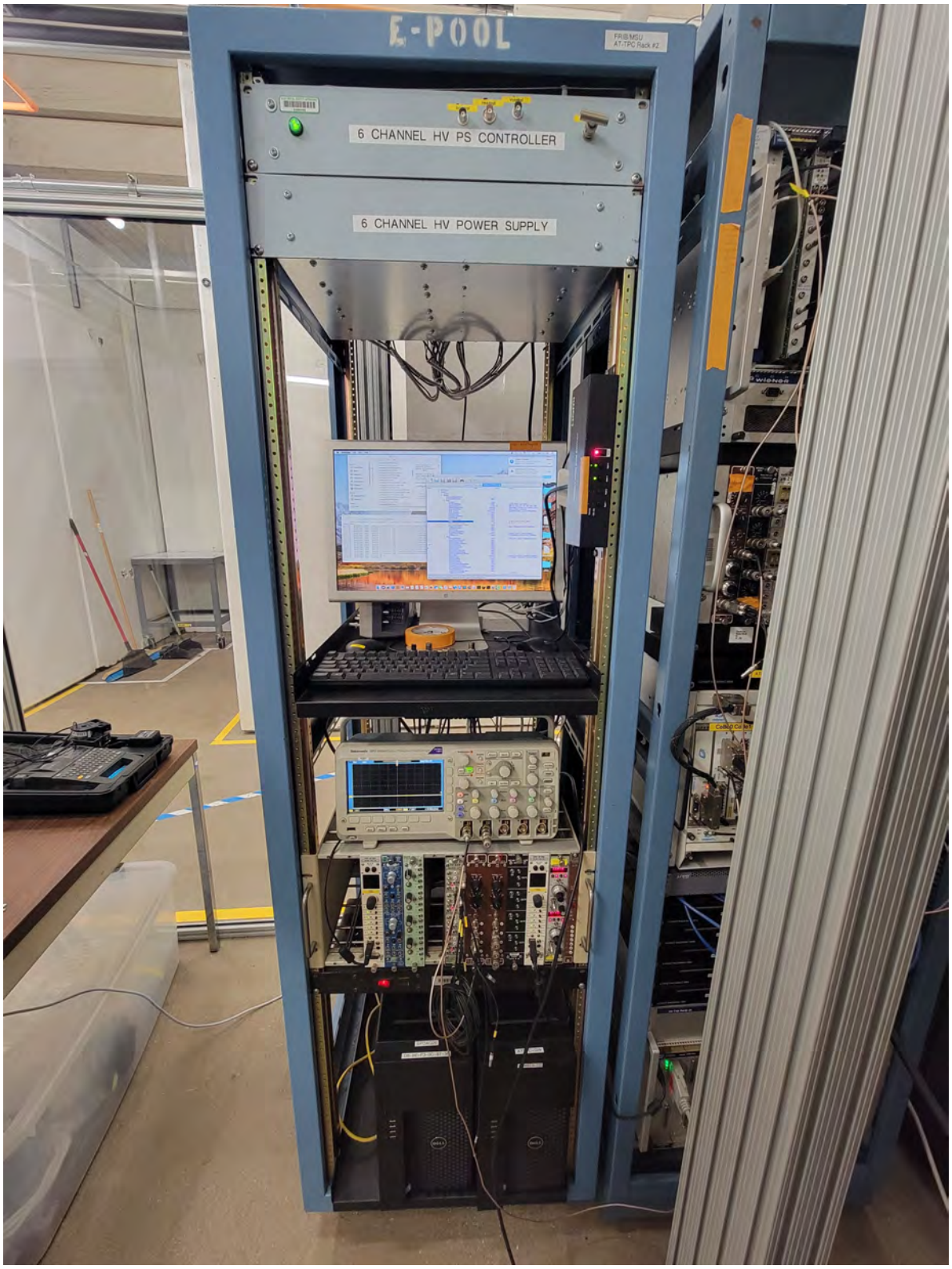

Figure 2.2 Rack housing the computer that controls the gas-handling system and the high voltages applied to the MPGDs and the cathode. It also contains the MPGD high voltage supply itself.

Figure 2.3 Rack housing the cathode high-voltage power supply and gas-handling systems for the AT-TPC and IC.

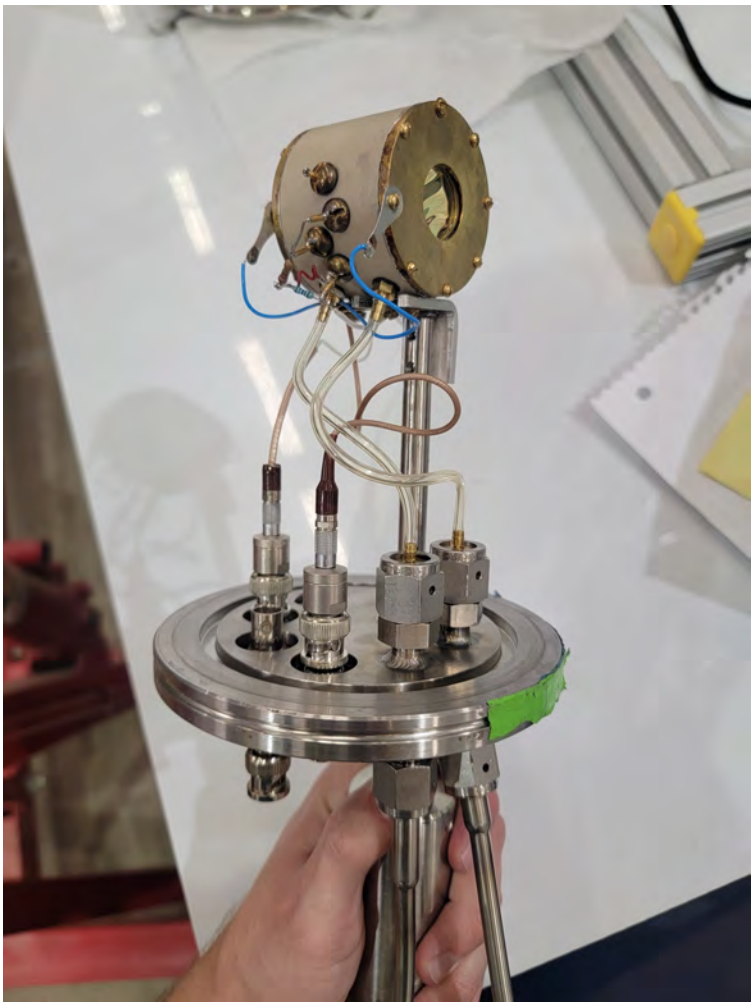

Figure 2.4 The IC is the cylinder atop the vacuum flange. Its electrical and gas leads can be seen.

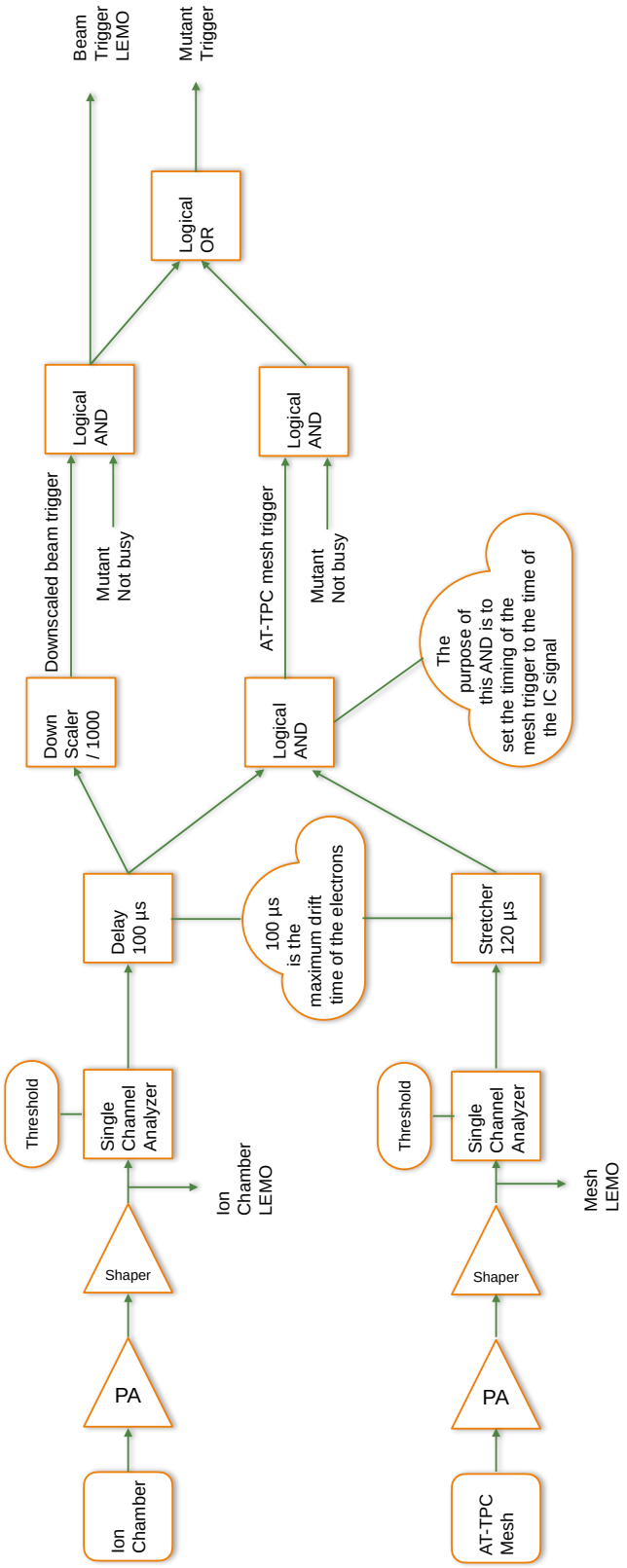

Figure 2.5 Trigger logic for the experiment of this thesis. Courtesy of Daniel Bazin.

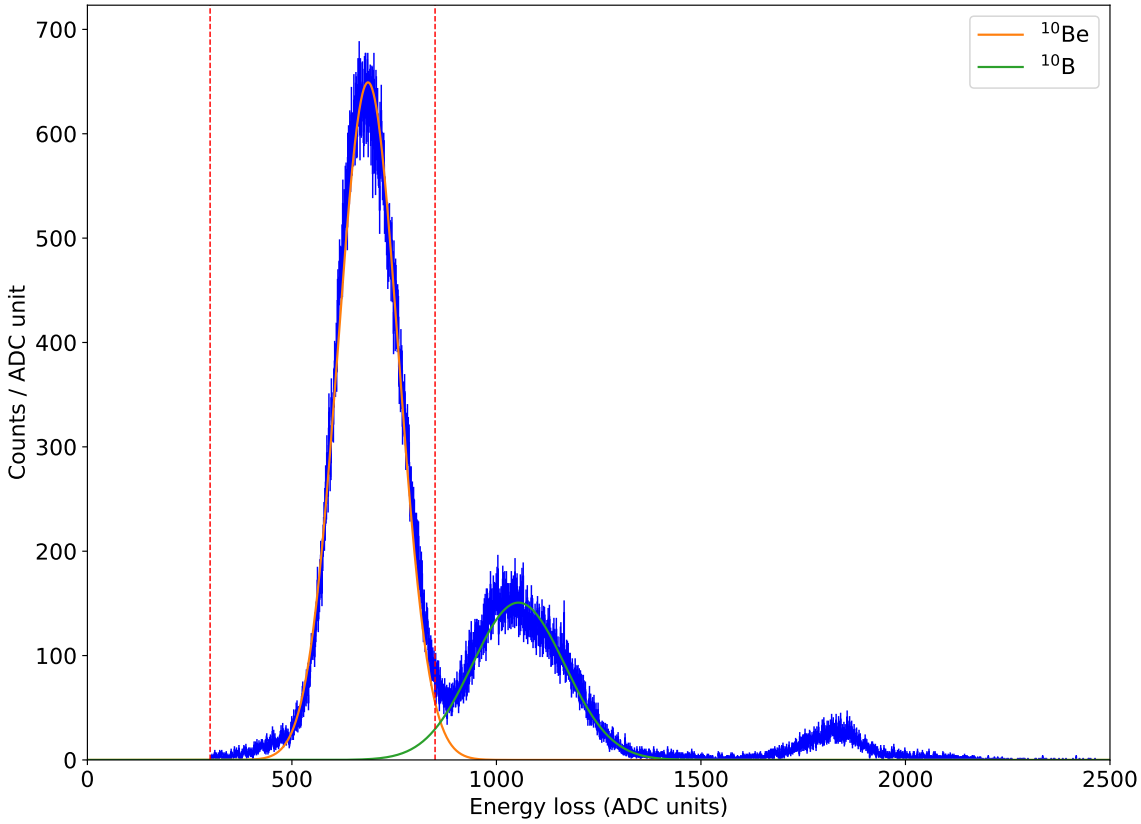

Figure 2.6 Histogram of the energy loss of incoming unreacted beam particles seen over the course of the entire experiment. The dotted vertical dotted lines correspond to the gate used to select ^{10}Be events. The Gaussian fits used to subtract the ^{10}B contamination from the ^{10}Be counts in the gate are shown. The small peak short of 2000 ADC units belongs to ^{15}N.

CHAPTER 3

ANALYSIS OF AT-TPC DATA

This chapter is dedicated to describing the arduous process of analyzing AT-TPC data. For the experiment of this thesis, the data was analyzed using a modified version of the Python package SPYRAL [19]. There is no attempt here at detailing the coding specifics of this package. Instead, the main concepts of the analysis will be illustrated with references to the relevant portions of SPYRAL where necessary. Due to this, the SPYRAL parameters used in each step of the analysis will be given but not all of them may be discussed in the text. They are included for completeness.

3.1 Data structure

As mentioned in Section 1.3, the AT-TPC uses the GET system for data acquisition. For each event of a run, a CoBo records a pad's trace only if it had charge deposited above a threshold set in the CoBo's configuration file. A trace is composed of 512 time buckets. A time bucket in GET does not represent an instantaneous measurement but rather the sum of measurements within the time width of that bucket. A trace from this thesis' experiment is shown in Fig. 3.1. GET is highly flexible and the length of a time bucket can be changed via the sampling frequency. For this experiment, the sampling frequency was set to 3.125 MHz so that each time bucket sampled 0.32 μsec. With 512 time buckets, the total time range covered by the GET system was 163.84 μsec, enough to record the longest drift time of the electrons (about 100 μsec).

All events an AsAd records traces for in a run are output to a single binary file called a graw file. The graw files from all AsAds, each representing a different group of pads on the pad plane, are merged together into a single HDF5 file to form a complete record of each event in a run. This is accomplished using a merger program. HDF5 is ideal for AT-TPC data because it is a hierarchical data format that functions like a folder directory. The traces of all pads from each event are stored together in one HDF5 file under what is called a group (the data itself is called a dataset in HDF5). The merged HDF5 files have sizes on the order of tens of gigabytes as they contain tens of thousands of events that each contain hundreds of pad traces that are 512 time buckets long. The large size of the HDF5 files make them somewhat cumbersome to work with, but transforming the data from

traces to point clouds drastically reduces their size.

3.2 Creating point clouds

The first major step of analyzing AT-TPC data is converting an event from traces to a point cloud. As a time projection chamber, the AT-TPC visualizes the trajectories of ionizing radiation within it. The points along the trajectories are extracted from the traces of the pads that recorded signals during an event. These are the trajectories that are analyzed. The Spyral parameters for this phase are listed in Table 3.1.

3.2.1 Baseline correction

Before any peaks are extracted from a trace, the signal baseline is first removed. Correctly removing the baseline is key for accurately calculating the total charge deposited on a pad. This is needed to accurately determine the energy deposited by a particle over the pads that make up its track. The best method found for calculating the baseline is applying a moving average to the raw trace, as pointed out by Bradt [20]. The idea is to perform a discrete convolution of the raw trace with a rectangle function over its 512 time buckets,

$$(f * g)(t) = \sum_{\tau=0}^{511} f(\tau) g(t - \tau) \tag{3.1}$$

where $(f * g)(t)$ is the discrete convolution yielding the noise in the raw trace at time t. f is the raw trace of the pad and g is the rectangle function divided by its length a

$$g(t) = \frac{1}{a} \begin{cases} 1, & |t| \leq \frac{1}{a} \\ 0, & \text{elsewhere.} \end{cases} \tag{3.2}$$

a is an integer controlling how many time buckets are taken for averaging and was set to 20. The convolution theorem allows the discrete convolution to be calculated as

$$(f * g)(t) = \mathcal{F}^{-1}\{\mathcal{F}\{f\}\mathcal{F}\{g\}\} \tag{3.3}$$

where $\mathcal{F}$ is the Fourier transform. This has the benefit of being extremely fast due to the speed of the fast Fourier transform. It is also convenient that the Fourier transform of g is given by the normalized sinc function provided in many fast Fourier transform libraries.

One correction is needed for this procedure to work. The peaks in the raw trace must be masked before applying the convolution to avoid them influencing the baseline correction. Bradt masked any time bucket with a value larger than 1.5 standard deviations of the average value of the raw trace with the trace's average. The same procedure is used in SPYRAL. After masking the peaks and calculating the discrete convolution, the result is subtracted from the raw trace. This yields the baseline-corrected trace (see Fig. 3.1).

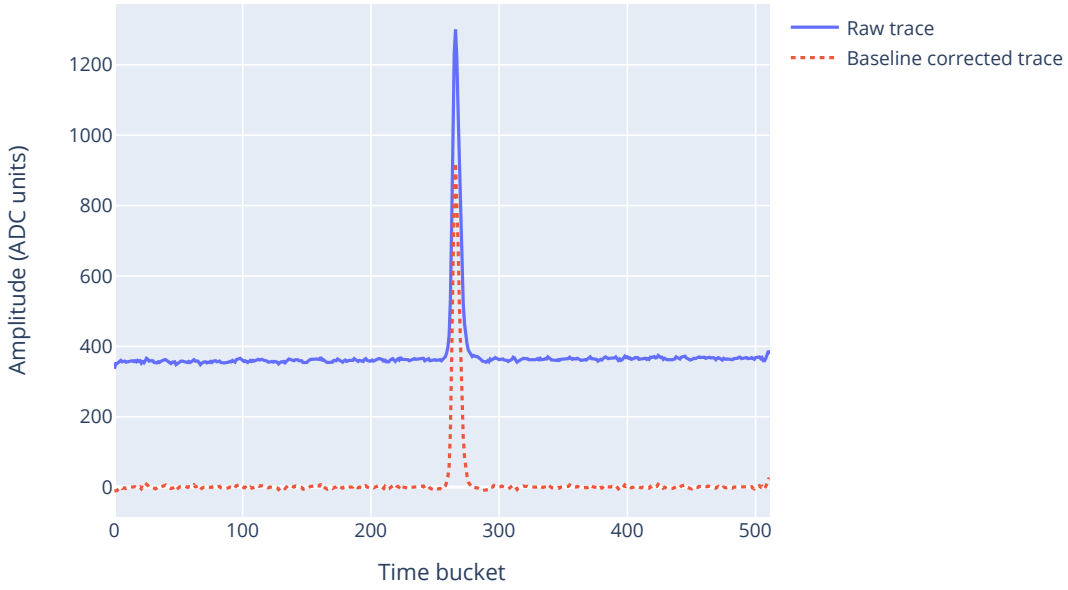

Figure 3.1 A pad's trace taken from an event during the experiment shown in solid blue. The baseline of the trace is removed using the outlined procedure to produce the corrected trace shown in dotted red.

3.2.2 Pulse extraction

The baseline-corrected trace is used to extract information related to the electrons that induced a signal on a pad. Peaks in a trace correspond to signals induced by the electrons. A peak contains two valuable pieces of information: its location in time and amplitude. A peak finding algorithm is able to provide both of these pieces of information, and the SciPy find_peaks function was used

[21]. The location is related to how long the electrons drifted in the AT-TPC, and its amplitude is proportional to the number of electrons detected at that time. The location cannot be measured to finer accuracy than a time bucket because a time bucket is an integrated sampling and not an instantaneous measurement. To account for this uncertainty, the peak location was randomly chosen within its measured time bucket. This implies an error taken as half a time bucket's width

$$\sigma(t) = \frac{1}{2}. \tag{3.4}$$

The trajectory of the ionizing particle lives in 3D Euclidean space, so each point in the point cloud of an event is described by three position coordinates. The coordinate system used for this analysis has the origin at the center of the AT-TPC window with the positive z-direction towards the pad plane. Two coordinates are immediately known from the pad the trace belongs to. The pad plane of the AT-TPC is completely mapped out and each pad is assigned an x- and y-position according to its centroid. The uncertainty in the xy-position can be characterized by the size of the pads. The AT-TPC pad plane is composed of triangles of two different sizes (see Section 1.3). The error is estimated by circumscribing each triangle with a rectangle. The error in the the x- and y-directions is simply half the length of the respective side of the circumscribed rectangle. Explicitly:

$$\sigma(x) = \begin{cases} 0.0025, & \text{small pad} \\ 0.0050, & \text{big pad} \end{cases}, \qquad \sigma(y) = \begin{cases} 0.0029, & \text{small pad} \\ 0.0058, & \text{big pad} \end{cases} \tag{3.5}$$

where the standard deviations are in meters.

The z-coordinate is calculated from the location in time of a peak. Combining the peak time bucket t with the drift velocity v_e of the electrons (in units of meters per time bucket) allows the z-coordinate z (in meters) to be reconstructed via

$$z = v_e(w_{edge} - t) \tag{3.6}$$

where w_{edge} is the time bucket of the AT-TPC window in the GET electronics. Eq. 3.6 has $z = 0$ at $t = w_{edge}$ as required by our coordinate system. Section 3.2.3 will explain how v_e and w_{edge} are

calculated, but in theory the point cloud can now be fully constructed with each point consisting of x- and y-coordinates given by the pad that detected the electrons and the z-coordinate by Eq. 3.6. Fig. 3.2 shows a point cloud of an event from the experiment.

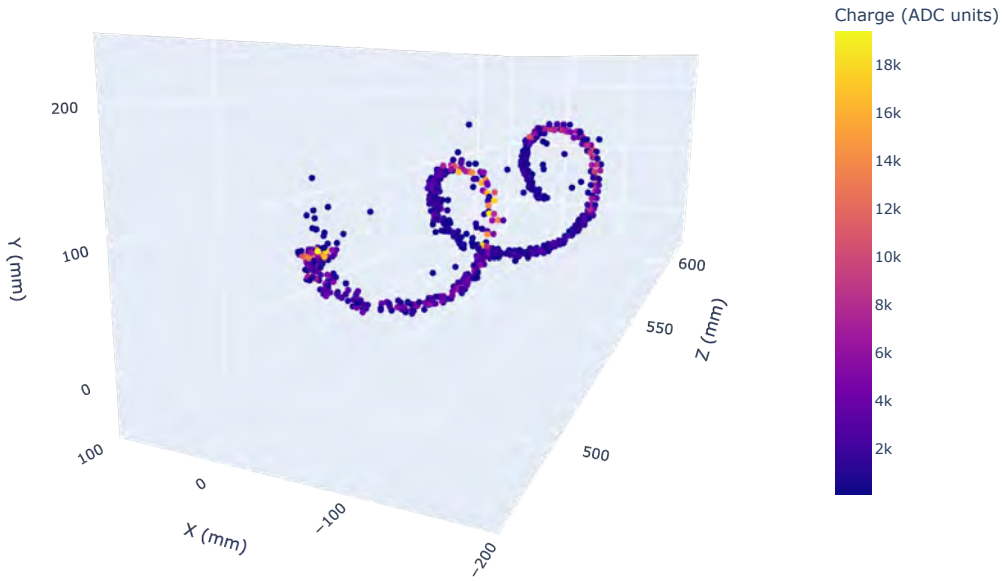

Figure 3.2 Point cloud of an event from the experiment. The spiral track was identified as originating from a proton.

3.2.3 Electron drift velocity measurement

Construction of the point cloud requires knowledge of the electron drift velocity, as seen in Eq. 3.6. Ideally, the drift velocity would be experimentally measured continuously over the course of an experiment with a laser or some other device. This experiment did not have such a device, so the drift velocity was calculated on a run-per-run basis using unreacted beam events.

Fig. 3.3 shows the reconstructed beam-region mesh signal of an unreacted beam event. The leftmost edge corresponds to the micromegas edge m_{edge} and the rightmost edge to the window edge w_{edge}. The micromegas edge is created by the detection of liberated electrons immediately

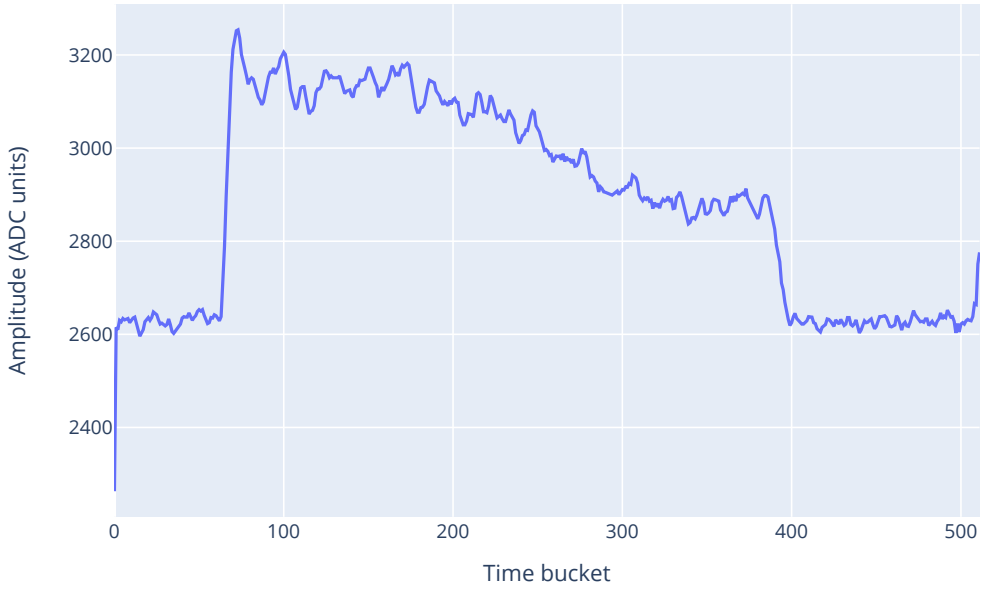

Figure 3.3 Reconstructed beam-region mesh signal from an unreacted beam event. The micromegas edge near 60 time buckets is from liberated electrons near the MPGDs and the window edge near 400 time buckets is from liberated electrons near the window.

above the stack of MPGDs. These electrons drift the shortest distance to the MPGDs and hence are detected first. The window edge corresponds to the detection of electrons from near the window of the AT-TPC and are detected last. m_{edge} and w_{edge} are the temporal locations of their respective physical extremity of the AT-TPC. Subtracting them yields the time it took for electrons to drift the entirety of the detector. The drift velocity is then

$$v_e = \frac{l}{w_{edge} - m_{edge}} \tag{3.7}$$

where l is the length of the AT-TPC.

m_{edge} and w_{edge} were found for multiple unreacted beam events in each run. The unreacted beam events were gated to ensure that only one beam particle was present and that the beam particle ionized the gas along its entire trajectory through the AT-TPC. These requirements helped ensure a reconstructed beam-region signal like that of Fig. 3.3. The average of both edges for each run

were calculated. The errors on the average micromegas edge $\sigma(m)$ and window edge $\sigma(w)$ were respectively found by the standard error of their mean

$$\sigma(m/w) = \frac{s}{\sqrt{n}} \tag{3.8}$$

where n is the number of unreacted beam events and s is their sample standard deviation. Fig. 3.4 shows the drift velocity as a function of the run over the course of the experiment.

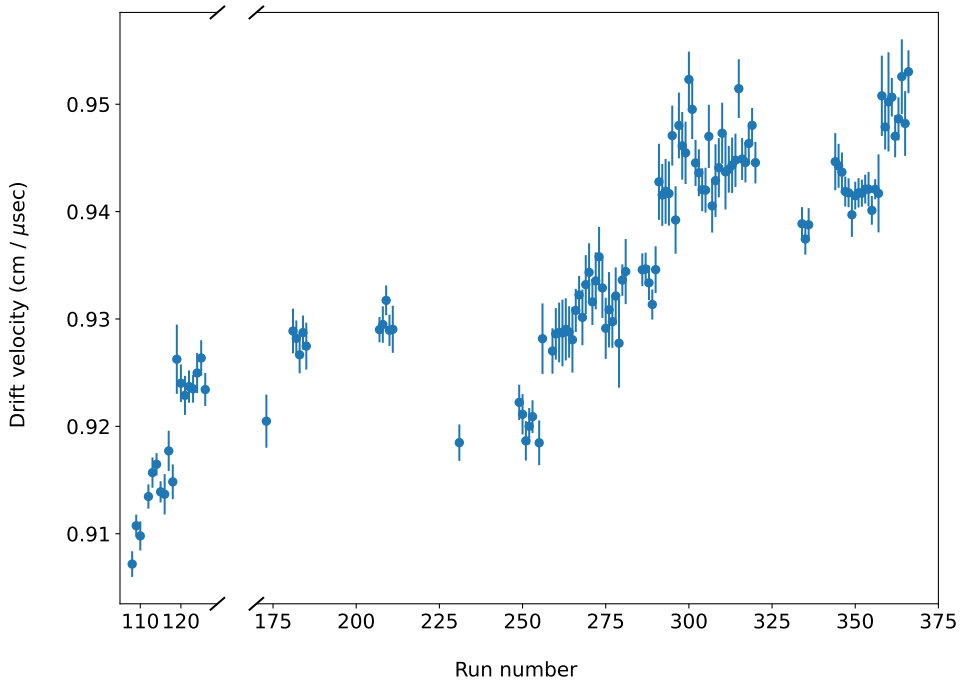

Figure 3.4 Drift velocity of experimental runs used in the analysis.

3.2.4 GET time correction

Despite the electronics for each pad being theoretically the same, their response functions differ due to known bugs in the CoBo firmware. Thus, if two signals are induced at exactly the same time on two different pads, the signals are not guaranteed to peak at the same time bucket. This leads to systematic offsets in the calculated z-positions of points determined from each pad that need to be corrected.

To characterize the time correction of each pad, a pulse generator was used to pulse the micromegas mesh. Each pulse uniformly induced a signal on each pad, thus any difference in the

time bucket of the signal's peak between pads was due to their dissimilar responses. Multiple runs were taken each with a different voltage ranging from 100-500 mV. The data from these pulser runs had the same format as the real data and their point clouds were created using the same SPYRAL analysis except that $peak\_max\_width = 300.0$ and $peak\_threshold = 100.0$ in the GET parameters (see Table 3.1). For each event in a pulser run, the time bucket of the earliest peak in each pad's trace was recorded and its average t_{pad} calculated. The error on t_{pad}, $\sigma(t_{pad})$, for each pad was found from the standard error of the mean of its distribution (see Eq. 3.8). The average time bucket of the earliest peak in that pulser run, t_{avg}, was found from the inverse-variance weighted average of each t_{pad}. Its error $\sigma(t_{avg})$ is given by the standard error of the weighted mean

$$\sigma(t_{avg}) = \sqrt{\frac{1}{\sum_i \sigma_i(t_{pad})^{-2}}} \tag{3.9}$$

where the summation is taken over all pads. The time correction factor c_{pad} of each pad in a run is then

$$c_{pad} = t_{avg} - t_{pad} \tag{3.10}$$

with an error $\sigma(c_{pad})$ given from the standard error propagation formula as

$$\sigma(c_{pad}) = \sqrt{\sigma(t_{pad})^2 + \sigma(t_{avg})^2}. \tag{3.11}$$

The time correction factor of each pad was found for each pulser voltage. Fig. 3.5 shows the time correction factor for a pad as a function of its average signal amplitude. It is not plotted as a function of the voltage. At higher voltages the pads saturate their analog circuits and ADCs, producing distortions in their electronic responses; saturation is only evident in a pad's signal amplitude. There is an error associated with the calculated average signal amplitude of a pad for each voltage, but they were found to be smaller than 1% of the signal amplitude on average and are negligible. Fig. 3.5 is well described by a linear fit with a very small slope. The final time correction factor used for each pad was the the y-intercept of its linear fit.

3.2.5 Electric field correction

Due to a limitation of the maximum high voltage available on the MPGD high-voltage supply, the electric field was non-uniform, altering the drift paths of the liberated electrons close to the

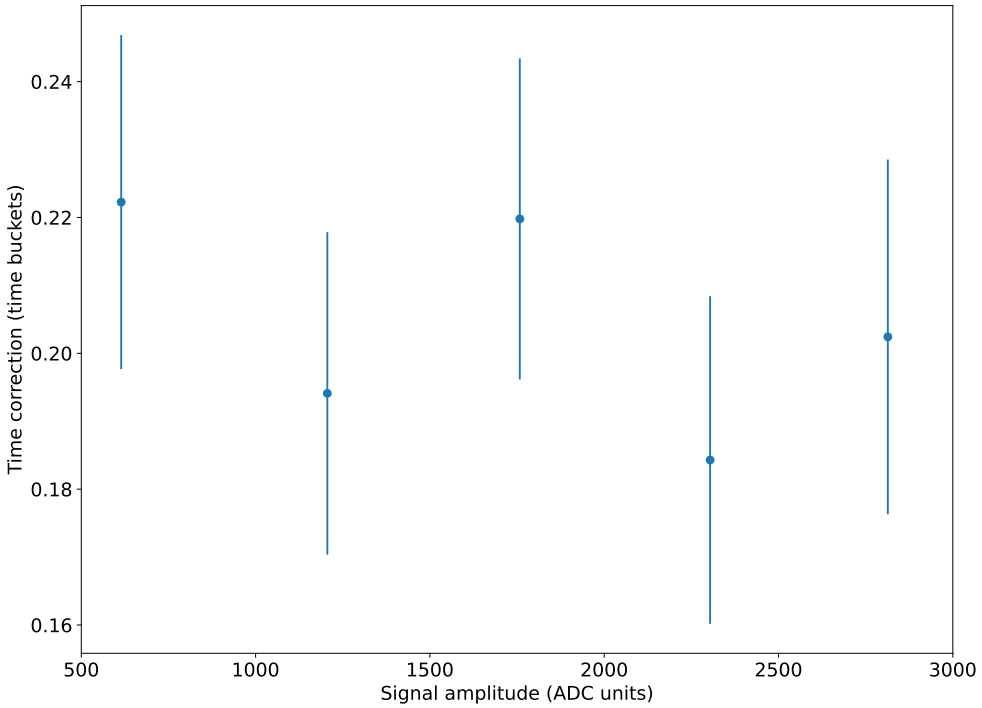

Figure 3.5 Time correction factor for pad 4632 as a function of its average signal amplitude for various pulser voltages. The errors on the average signal amplitudes are shown but are very small. Within error, the correction factor is well described by a constant value.

outer diameter of the field cage. Specifically, the voltage on the final ring of the field cage was too low, which created a different voltage gradient between it and the top M-THGEM. The net effect of this non-uniformity was that the reconstructed trajectories may not accurately represent the true paths of the ionizing particles in this region.

This non-uniformity of the electric field was corrected by performing a simple Garfield++ calculation. The electric field was modeled with the rings of the field cage and its volume filled with deuterium gas. The field cage was subject to the same magnetic field as in the experiment. The inner volume of the field cage was meshed and stationary electrons were placed at each point. The electrons were drifted through the gas by the electromagnetic fields and their intersections with the AT-TPC pad plane recorded. This allowed for the creation of a mapping between initial and final electron positions, which was used to correct the electric field non-uniformity. To avoid a large and very fine mesh, this mapping was interpolated upon to estimate the correction for arbitrary points.

The electric field correction grows with increasing distance from the center of the AT-TPC and

Parameter	GET	Ion chamber
baseline_window_scale (time buckets)	20	100
peak_separation (time buckets)	5	5
peak_prominence (ADC units)	20	30
peak_max_width (time buckets)	100	20
peak_threshold (ADC units)	30	300
low_accept (time buckets)	N/A	60
high_accept (time buckets)	N/A	411

Table 3.1 SPYRAL point cloud phase parameters for the experiment of this thesis.

was found to minimally impact the reconstructed proton tracks due to their low magnetic rigidity. It heavily modified the deuteron tracks, though. Deuterons have twice the magnetic rigidity of protons of the same velocity and can reach the fringes of the AT-TPC electric field with much less energy. Figs. 3.6 and 3.7 show the effect of the correction on tracks identified as created by a proton and deuteron, respectively.

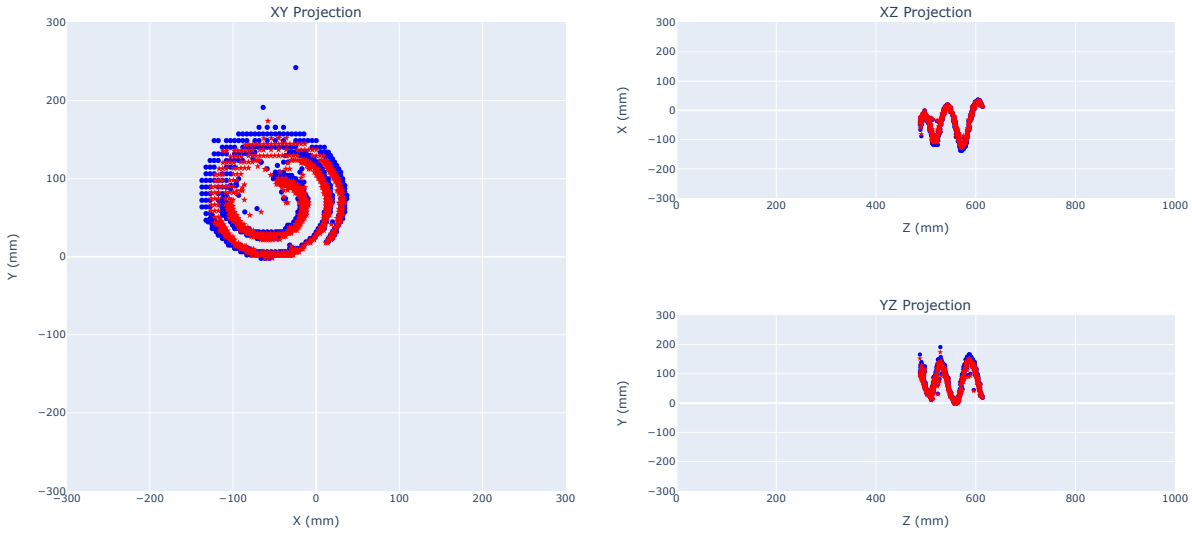

Figure 3.6 Track identified as originating from a proton shown without the electric field correction (blue circles) and with it (red stars).

3.3 Clustering tracks

Reconstructing the point cloud for an event is not sufficient to analyze it. Multiple particle trajectories can be recorded, as well as noise. Points must then be grouped together, or clustered, into tracks based on the particle trajectory they belong to. This section details this process as done

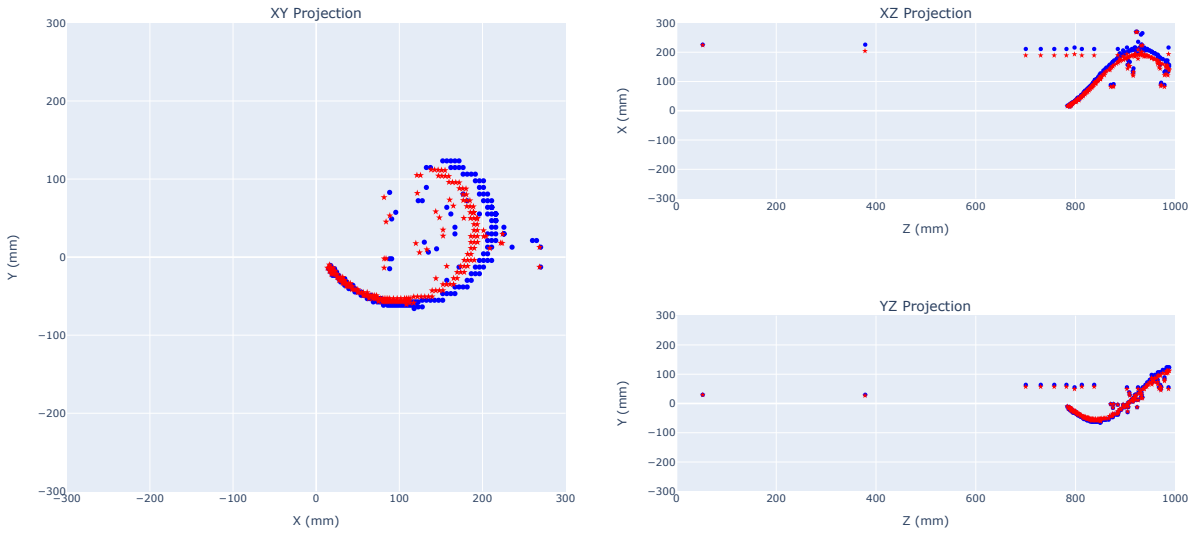

Figure 3.7 Track identified as originating from a deuteron shown without the electric field correction (blue circles) and with it (red stars).

by the cluster phase of SPYRAL. The parameters for this phase used in this analysis are shown in Table 3.2.

3.3.1 Pre-clustering

A point cloud must meet certain conditions and undergo some dimensional scaling before being clustered. To begin, illegal points are removed from the cloud. These points are outside of the active volume of the AT-TPC and can occur because the AT-TPC time recording window is longer than the maximum drift time of the electrons. After removing the illegal points, a point cloud must contain a minimum number of points, which, for this experiment, was chosen to be 20. This is to prevent noisy events with small numbers of points and small broken tracks from being analyzed. These types of events typically arise when a beam particle scatters outside the beam region ("leaky beam" events), or when a target-like recoil has just enough energy to emerge from the beam region and stops not far from it (e.g. elastic scattering close to 90°).

The clustering algorithm used (described in Section 3.3.2) clusters points based on a distance metric. However, there is a very large physical asymmetry in the AT-TPC: the length of the cylindrical active volume is about twice its diameter! The z-coordinate can take on a much larger

range of values than the x- and y-coordinates. For spatial clustering, we want our data to be unified to the same range to prevent biasing. This is accomplished by normalizing the z-coordinate of the points in the cloud to the diameter of the AT-TPC.

3.3.2 HDBSCAN clustering

After pre-clustering, a point cloud is clustered using the Hierarchical Density-Based Spatial Clustering of Applications with Noise (HDBSCAN) [22] algorithm. As the name suggests, HDBSCAN clusters the points in the cloud based on their densities. Instead of clustering based on the Euclidean distance between points, it defines a new metric called the mutual reachability distance. This metric is beneficial because it is chosen to push sparsely populated areas that more likely correspond to noise away from more densely populated areas that more likely correspond to real data [23]. After calculating the mutual reachability distance for all combinations of points in the cloud, HDBSCAN finds its clusters that can be of varying local densities. This feature is needed for the AT-TPC because the pad plane is not made of uniformly sized pads. The details of the HDBSCAN algorithm can be found in Refs. [22, 23].

HDBSCAN in Spyral is controlled by four parameters listed in the "Clustering" section of Table 3.2. minimum_points is related to how conservative the clustering is, with larger values resulting in fewer clusters in only the densest areas. [23] (it is actually the algorithm's smoothing factor m_{pts} described in Ref. [22]). minimum_size_scale_factor and minimum_size_lower_cutoff determine the minimum required number of points to form a cluster, denoted as m_{clSize}. Because the number of points in an AT-TPC cloud, n_{points}, can wildly vary, this minimum is determined on a per cloud basis as

$$m_{clSize} = \max\{\text{minimum\_size\_scale\_factor} * n_{points}, \text{minimum\_size\_lower\_cutoff}\}. \quad (3.12)$$

cluster_selection_epsilon sets a minimum distance between two clusters for them to be considered unique. If the two clusters are within this distance, they are merged. This parameter is useful because it allows for m_{clSize} to be small but prevents HDBSCAN from breaking up areas with high densities of points into many small clusters [23]. Fig. 3.8 shows the clustering of a track produced by HDBSCAN.

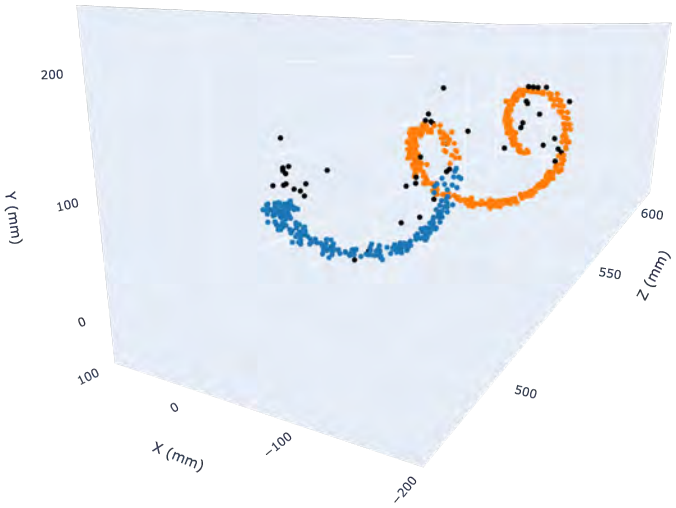

Figure 3.8 HDBSCAN clustering of the point cloud shown in Fig. 3.2. Black points are noise while blue and orange points belong to two distinct clusters.

3.3.3 Merging clusters

A common occurrence with clustering AT-TPC point clouds is that a particle track will be broken up into smaller clusters instead of being correctly identified as a single cluster. This can occur because some tracks travel through the beam region that records highly suppressed signals. HDBSCAN sometimes will also fragment a single track. The clustered fragments of a single particle track must then be merged together into a single cluster.

The particle tracks in the AT-TPC curve due to the magnetic field of the solenoid. The projections of the track fragments on the plane perpendicular to the beam (the sensor plane) should then appear circular and all be concentric, sharing a common center point. Each fragment can be fit with a circle and if the centers of two fragments are close, they are merged together. This method works well but introduces an arbitrary parameter for how close two fragment centers must be that depends on the geometry of the track, i.e. this method is scale dependent [24]. A scale independent method is found by merging two clusters if the overlap area of their circle fits is greater than a set

percentage of the smaller circle's area, which was chosen to be 0.25 for this analysis. However, to avoid merging small clusters of noise with an actual track, a minimum number of points must be present in a cluster. 15 points were required for a cluster to be able to merge in the analysis.

3.3.4 Cluster cleanup

The final operation applied to the clusters is the scikit-learn LocalOutlierFactor function [21]. This function compares "the local density of a sample to the local densities of its neighbors" to identify outliers in a cluster [25]. It is the last attempt at removing noise from a cluster. A scale factor, outlier_scale_factor, is used for determining how many neighbors n_{neigh} are compared to in the calculation due to the fact that the number of points in an AT-TPC cloud wildly vary. n_{neigh} is calculated as

$$n_{neigh} = \max\{\text{outlier\_scale\_factor} * n_{points}, 2\} \tag{3.13}$$

where n_{points} is the number of points in the cluster. The identified outliers are removed from the cluster. Fig. 3.9 shows the final cluster from the point cloud of Fig. 3.2 after the merging and cleanup steps were performed on its initial HDBSCAN clustering shown in Fig. 3.2.

	Parameter	Value
Pre-clustering	min_cloud_size	20
Clustering	min_points	3
	min_size_scale_factor	0.05
	min_size_lower_cutoff	10
	cluster_selection_epsilon	10
Merging	min_cluster_size_join	15
	circle_overlap_ratio	0.25
Cleaning	outlier_scale_factor	0.05

Table 3.2 SPYRAL clustering phase parameters used for the analysis of this experiment.

3.4 Estimating clustered track kinematic parameters

After an event has been clustered, the kinematic parameters of its tracks are estimated. These estimations will be feed to an optimizer afterwards for refinement, described in Section 3.6. This section describes the process done by the SPYRAL estimation phase and the parameters used are shown in Table 3.3.

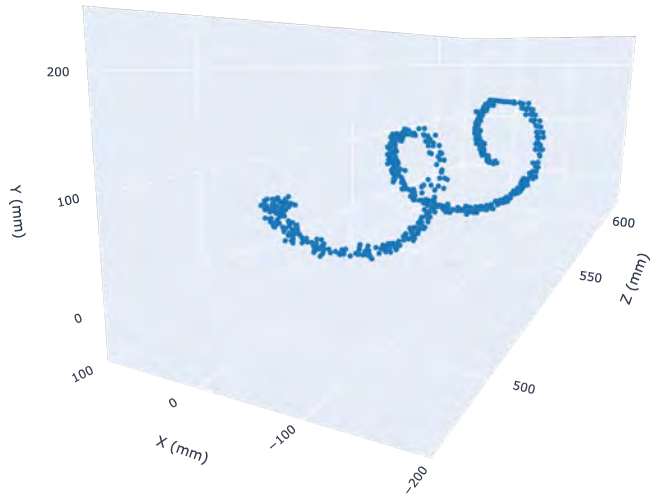

Figure 3.9 Final clustering of the point cloud from Fig. 3.2 after the initial clustering in Fig. 3.8 underwent merging and cleanup. All points belong to the same singular cluster.

As the reader goes through this section, there may be points in the following methodology that they believe are not completely correct. For example, they might feel that an assumption is made unjustly or conceive of an alternative method. Remember, what is done here is merely an estimation. The hope is that no matter what method is used to guess the kinematic parameters of a clustered track, they are close enough to their real values for the optimizer to converge to the lowest value of the objective function.

3.4.1 Smoothing splines

As the clustered tracks currently stand, they are not ideal to work with. They are diffuse due to the diffusion of charge and may have noise accidentally appended to them from poor clustering. The net effect is that a clustered track depicts a blurry image of a particle's trajectory. This is undesirable for algorithms to estimate its kinematic parameters because they can be heavily influenced by non-central and noisy points. To best estimate the actual path of the particle, its clustered track can be smoothed using smoothing splines. The SciPy function make_smoothing_spline [21] is used to

independently spline the x- and y-coordinates as a function of their z-coordinates. These splines are then used to create a smoothed track by evaluating the splines at the z-coordinates of each point in the original clustered track.

The splining can fail if the clustered track does not contain enough points or has multiple points with the same z-coordinate. Such tracks are discarded. Importantly, the splined track is merely a copy of the clustered track and does not replace it. The final optimization is done on the original clustered track, which is what the AT-TPC actually records.

3.4.2 Vertex position

The first kinematic parameter to be extracted is a particle's initial position. It is given by the reaction vertex of its event. This experiment could not measure the reaction vertex directly because the signals of the beam region pads were highly suppressed. This means that the reaction vertex had to be extrapolated from the characteristics of each track. The assumption is made that the beam entered the AT-TPC perfectly straight and parallel to the z-axis (see Section 3.2.2 for an explanation of the coordinate system used). This information can be used to guess whether the particle's splined track went forward or backward by calculating the distance of its two endpoints to the z-axis; the endpoint with the smallest distance is taken as being closer to the vertex and thus defines the track direction. The direction of the track is needed because it determines which points in the cluster compose its first arc. The first arc of a splined track is defined as all points from its endpoint closest to its vertex to its point farthest from the z-axis. The xy-projection of this first arc is fit with a circle and the point on the fit closest to the z-axis gives the estimates for the x- and y-coordinates of its vertex.

The z-coordinate of the vertex is estimated by applying a linear regression to a small segment of the first arc. The regression includes either its first 10 points or half its total points, whichever is larger, and is done in cylindrical coordinates. The distance ρ of each point in the first arc from the vertex is linearly fit as a function of the z-coordinate. The linear fit provides the slope m and intercept b of the line defined by

$$\rho = mz + b. \tag{3.14}$$

The vertex has $\rho = 0$ and its z-coordinate is given by

$$z = \frac{-b}{m}. \tag{3.15}$$

With the vertex fully estimated, its distance from the z-axis is calculated. If this distance is larger than the beam region radius the splined track is discarded. Either the vertex algorithm failed or it did not originate from a beam reaction.

A self-consistency check can be performed with the slope of the fit and the estimated direction of the splined track. Recall that we have defined the coordinate system of the AT-TPC with the window at $z = 0$ m and the micromegas at $z = 1$ m. This implies that $m > 0$ corresponds to forward-going tracks and $m < 0$ to backward-going tracks. Failing this check sends the track through the Spyral estimator again with the opposite direction.

3.4.3 Polar angle

The linear regression to find the z-coordinate of the vertex is also used to estimate the laboratory polar angle θ of the splined track. θ is found from trigonometry as

$$\theta = \begin{cases} \arctan(m), & m > 0 \\ \arctan(m) + \pi, & m < 0. \end{cases} \tag{3.16}$$

In the highly unlikely situation that $m = 0$, the splined track is discarded.

3.4.4 Azimuthal angle

The azimuthal angle ϕ is estimated from the vertex and circle fit to the splined track's first arc. It can be found from the geometry shown in Fig. 3.10 and is given by the blue angle to the tangent line of the circle fit at the estimated vertex. The dotted red radial line is perpendicular to the tangent line. With this knowledge, the angle in red, denoted as α, is related to the azimuthal angle by

$$\phi = \begin{cases} \alpha + \frac{\pi}{2}, & \alpha < \frac{3\pi}{2} \\ \alpha - \frac{3\pi}{2}, & \alpha \geq \frac{3\pi}{2}. \end{cases} \tag{3.17}$$

α is found as

$$\alpha = \begin{cases} \beta, & \beta \geq 0 \\ \beta + 2\pi, & \beta < 0 \end{cases} \tag{3.18}$$

with

$$\beta = \text{arctan2}\,(y_v - y_c,\ x_v - x_c), \tag{3.19}$$

where (x_c, y_c) and (x_v, y_v) are the xy-coordinates of the circle fit center and the vertex, respectively.

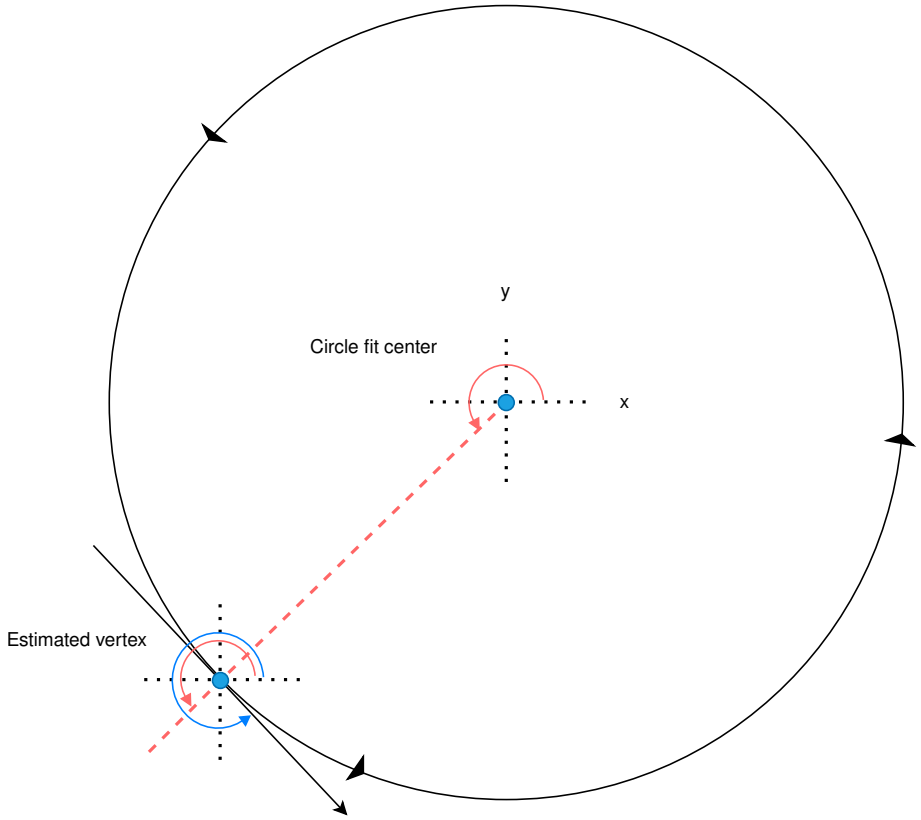

Figure 3.10 Geometry of the circle fit to the first arc of a splined track oriented with the beam coming out of the page. The arrows on the circle show the direction the track curves due to the magnetic field. The azimuthal angle shown in blue is measured to the tangent line to the circle at the estimated vertex. The angle shown in red is given by Eq. 3.18 and is measured to the radial line connecting the circle's center and the estimated vertex.

3.4.5 Energy ($B\rho$)

Classically, a particle of mass m, charge q, velocity $\vec{v}$, and angle θ with respect to a magnetic field of strength B curves with a radius ρ. Its $B\rho$ is given by

$$B\rho = \frac{|\vec{v}|m \sin\theta}{|q|}. \tag{3.20}$$

The Lorentz force used to derive Eq. 3.20 makes explicit that the particle curves in the plane perpendicular to the magnetic field. This means that ρ is measured in the plane parallel to the pad

plane for the AT-TPC. Although the AT-TPC does have an additional electric field, because it is parallel to the magnetic field, Eq. 3.20 is still correct. For general orientations of magnetic and electric fields Eq. 3.20 is not true.

Using the non-relativistic equation for kinetic energy E, we have

$$B\rho = \frac{\sqrt{2Em}\sin\theta}{|q|}. \tag{3.21}$$

Since $B\rho$ is proportional to the particle's kinetic energy and the scattering angle gives the particle's initial direction of motion, these two quantities are equivalent to the particle's initial velocity vector. $B\rho$ is straightforward to estimate for a track. B is an experimentally known parameter; only ρ must be extracted. ρ is given by the radius of the circle fit to the first arc of the splined track.

3.4.6 Energy loss and particle identification (PID)

Measuring the particle's initial position, polar angle, azimuthal angle, and $B\rho$ actually do not exhaust its kinematic variables. This is because its species is still unknown. This information is encoded in its $B\rho$ that depends on its mass and charge. However, neither of these variables can be found without another relationship as the problem is underdetermined.

The well-known solution to determining the species of a particle whose kinetic energy is known is to also measure its energy loss dE/dx. This can be understood as follows. The energy loss of a particle is given by the Bethe-Bloche formula, which for non-relativistic particles reduces to

$$\frac{dE}{dx} \propto \left|\frac{q}{\vec{v}}\right|^2 \tag{3.22}$$

where q is the charge and $\vec{v}$ the velocity of the particle [3]. Multiply this by the non-relativistic kinetic energy E to find

$$E * \frac{dE}{dx} \propto q^2 m \tag{3.23}$$

where m is the particle's mass. As q and m are fixed for each nucleus, the right-hand side of Eq. 3.23 is constant. Plotting E as a function of dE/dx gives hyperbolic curves as in Fig. 3.11.

The only hiccup with this approach is that the AT-TPC does not measure the kinetic energy of a particle from its splined track, but its $B\rho$. Despite this, let us multiply $B\rho$ by the energy loss. This

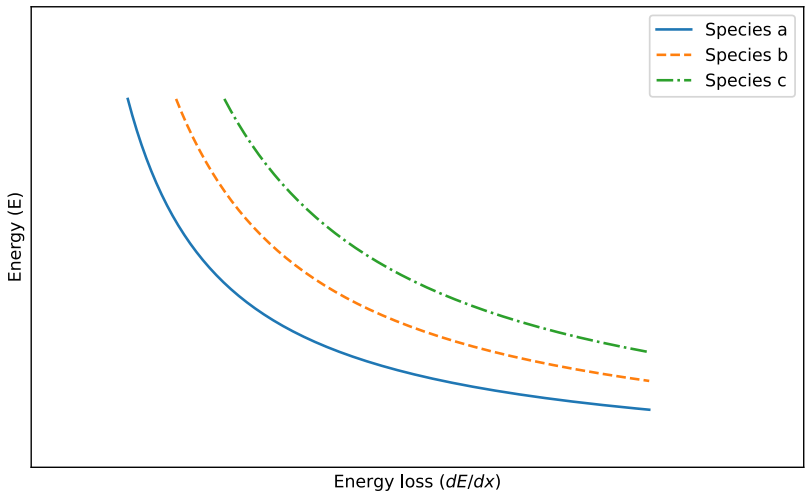

Figure 3.11 Example particle identification plot constructed by plotting energy vs. energy loss.

yields

$$B\rho * \frac{dE}{dx} \propto \left|\frac{q}{\vec{v}}\right| m \sin\theta. \tag{3.24}$$

Notice that the right-hand side would be constant if we removed the polar angle and velocity dependencies. Taking the square root of Eq. 3.22 and plugging it in along with some rearranging yields

$$\frac{B\rho}{\sin\theta} * \sqrt{\frac{dE}{dx}} \propto m. \tag{3.25}$$

Plotting $B\rho/\sin\theta$ as a function of $\sqrt{dE/dx}$ will result in hyperbolic curves that correspond to particles of the same mass. This is the particle identification plot used for this experiment (Fig. 3.12). Thus, to fully constrain the kinematics of a particle, its dE/dx must be estimated using its track.

The energy loss of a splined track is calculated by summing the deposited charge of each point in its first arc as defined in Section 3.4.2. The only caveat is that points from large pads on the pad plane are not included in the sum. The large pads have a different capacitance and collect more charge due to their increased surface area, leading to a higher effective gain compared to the small pads. The net effect is that large pads would not have the same weight in the sum as the small pads, and this problem is avoided altogether by not including them. The length of the first arc up to its

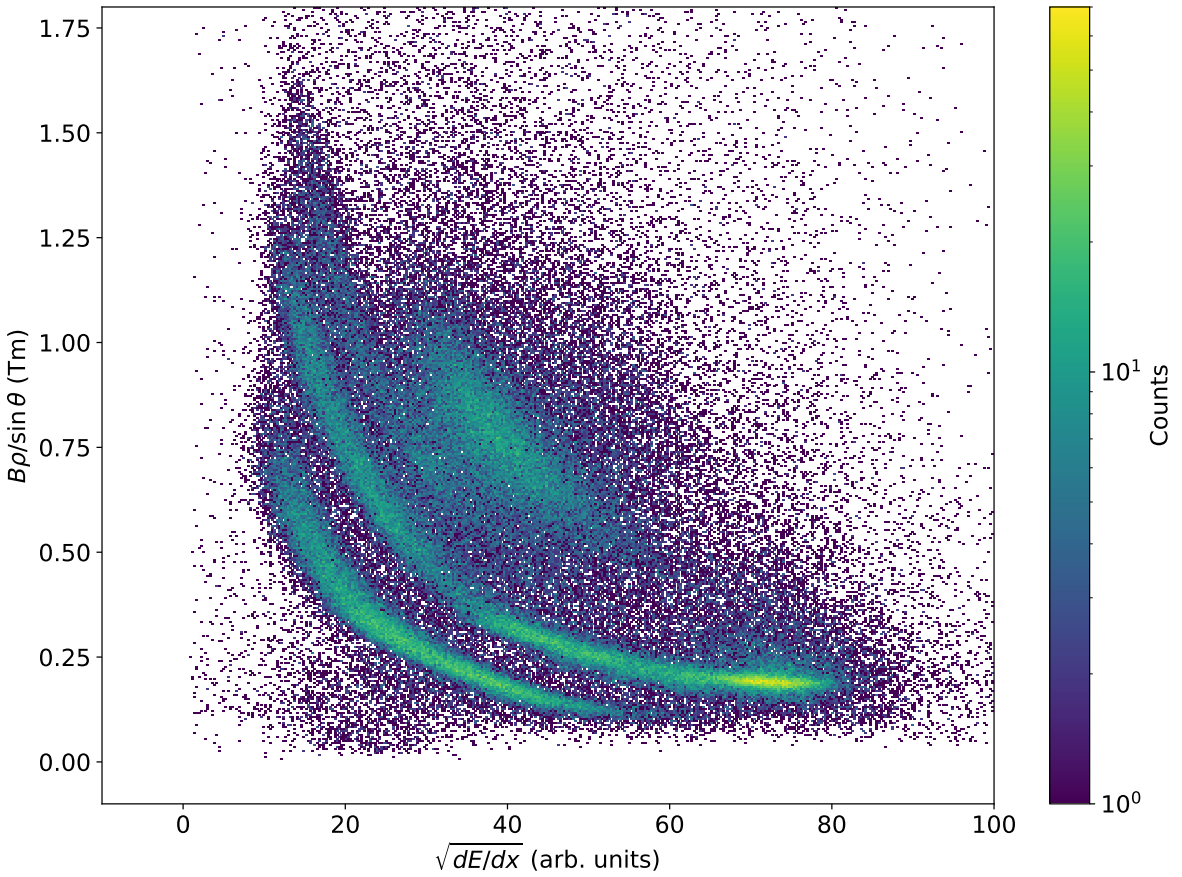

Figure 3.12 PID plot constructed from a subset of this experiment's data. The bottom-most band is made of protons while the band above it is made of deuterons. The other bands correspond to heavier species.

transition to the large pads is estimated from a fine line integral using 1000 points generated from the splined track's smoothing splines. Its dE/dx is found by dividing the deposited charge along the arc by this length.

Parameter	Value
min_total_trajectory_points	20
smoothing_factor	100.0

Table 3.3 SPYRAL estimation phase parameters used for the analysis of the experiment of this thesis.

3.5 Gain matching

While creating the PID plot for different runs of the experimental data, it became apparent that the measured energy loss changed as seen in the PID plots of the two runs shown in Fig. 3.13. This is due to the gain on the MPGDs changing, although it is not clear exactly why it did as their

experimental settings remained constant. One hypothesis is that impurities were introduced into the deuterium gas from the gas-recycling system. Regardless, this was corrected by normalizing the energy loss of each run to one selected run, which was run 347 for this analysis.

The normalization factor for each run was determined using a scheme proposed by Joseph Dopfer [26]. The deuteron band in the PID (Fig. 3.12) shows a hot spot for deuterons that deposited the most charge near $\sqrt{dE/dx} = 80$. Projecting the PID onto the $\sqrt{dE/dx}$ axis results in a histogram with a peak in this region. The centroid of this peak can be found for each run and the multiplicative factor to align it with that of the chosen run derived. The normalization factors were found to range within $5 - 30\%$ of the normalized value of 1.

3.6 Optimizing clustered track kinematic parameters

The estimated kinematic parameters from the estimation phase are fed into an optimizer for refinement to find the combination of their values that produce a track closest to the one observed. The optimizer produces solutions to the equations of motion of the particle in the AT-TPC and determines the solution that matches a track the best via an objective function it attempts to minimize. This is done by the interpolation phase of Spyral, whose parameters used in this analysis are given in Table 3.4.

3.6.1 Equations of motion

Particle trajectories are generated by solving the equations of motion of the particle in the AT-TPC. The relativistic equations of motion of a charged particle in the AT-TPC for this experiment are given by the Langevin equation

$$\frac{d\vec{p}}{dt} = q(\vec{E} + \vec{v} \times \vec{B}) - \vec{\eta}(t) \tag{3.26}$$

where $\vec{E}$ is the AT-TPC's electric field, $\vec{B}$ the SOLARIS solenoid's magnetic field, and q, $\vec{v}$, and $\vec{p}$ are the particle's charge, velocity, and three momentum, respectively. $\vec{\eta}(t)$ is a time-dependent damping force on the particle due to its energy loss through the target gas and modeled using the Python package pycatima [27] that interfaces with the well-known CATIMA energy loss library. Eq. 3.26 undergoes a large simplification as $\vec{E}$ and $\vec{B}$ each have only one component that is

anti-parallel to the incoming beam. It is solved using a numerical ODE solver with the initial kinematic parameter estimates found from the estimation phase in Section 3.4 and constrained to the physical boundaries of the AT-TPC. The solver terminates when the linear distance the particle would penetrate the target gas is 1 mm or less.

3.6.2 Interpolation mesh

Solving Eq. 3.26 for a particle in the AT-TPC is a well-posed problem, but how to do it efficiently is not. Explicitly, there is a very large computational cost associated with optimizing the solutions of an ODE. The optimizer will typically call the ODE solver many times while it is searching for its minima, and numerical ODE solvers can be slow. The problem is exacerbated by the fact that this experiment recorded terabytes of data. To analyze the data in any reasonable amount of time required a different method for generating ODE solutions. Here we describe the novel interpolation mesh method developed by Daniel Bazin.

To begin, we first recognize that two symmetries exist in subsets of solutions to Eq. 3.26. Suppose a subset of all solutions is given by those that share the same species, energy, scattering angle, and azimuthal angle in the AT-TPC. The trajectories of this subset must be the same except that they begin at different vertices; they are translationally invariant. We now remove the constraint that all trajectories have the same azimuthal angle. All trajectories of the resulting subset are rotationally invariant in the azimuthal angle if they are first translated to the same vertex. With these two observations, a drastic reduction in the space of solutions is achieved: solutions can be generated at a fixed vertex with a fixed azimuthal angle and translated/rotated as needed. This reduction in initial values needed to solve Eq. 3.26 strengthens the brute force option of simply generating a set of many solutions that the optimizer will draw from to compare to the actual data. The accuracy of this method heavily depends on the set size, and we would like it to be as large as possible. We thus interpolate between members of this set to infer solutions that are not part of it, effectively increasing its size.

For an input species and lists of energies and polar angles (the only two initial parameters of importance), SPYRAL generates solutions to Eq. 3.26 for all their combinations evaluated at the

same time steps. These time steps are logarithmically spaced with more steps at the earlier times. The x-, y-, and z-coordinates at each time step have their own interpolation mesh with axes given by energy and polar angle. Tracks are made by bilinearly interpolating each position coordinate at each time step for the desired energy and polar angle.

3.6.3 Optimizer and objective function

A plethora of optimizations algorithms exist, but, for the analysis of this thesis experiment, the limited-memory Broyden–Fletcher–Goldfarb–Shanno algorithm with box constraints (L-BFGS-B) [28] was chosen. L-BFGS-B was employed over a more traditional least-squares algorithm, like Levenberg-Marquardt, because of its significantly greater computational speed.

The optimizer requires an objective function whose output value is minimized. For the analysis of AT-TPC data, the objective function performs a comparison between the set of points T of a clustered track, with each point's total positional error a member of set $\sigma(\text{position})$, to the set of points D of a generated particle trajectory. Explicitly, the objective function is

$$f(T, D, \sigma(\text{position})) = \left(\sum_i \sigma_i(\text{position})\right)^{-1} \sum_j \frac{d_{min}(T_j, D)}{\sigma_j(\text{position})} \tag{3.27}$$

where T_j is the j-th point of T with total positional error $\sigma_j(\text{position})$ and $d_{min}(T_j, D)$ is the shortest Euclidean distance between T_j and some point in D.

The total positional error assigned to point j is

$$\sigma_j(\text{position}) = \sqrt{\sigma(x)^2 + \sigma(y)^2 + \sigma_j(z)^2}. \tag{3.28}$$

The uncertainty in the x- and y-coordinates of the point is given by Eq. 3.5. The uncertainty in the z-position is determined from propagating the errors in the point's measured time bucket, window edge time bucket, and micromegas edge time bucket through Eq. 3.6 with the drift velocity given by Eq. 3.7. The error of a time bucket is given by Eq. 3.4 and that of the micromegas and window edges by Eq. 3.8. The total error on the z-coordinate $\sigma_j(z)$ is then

$$\begin{aligned}\sigma_j(z) = l\sqrt{\left(\frac{1}{w_{edge} - m_{edge}}\right)^2 \sigma(t)^2 + \left(\frac{(t - m_{edge})}{(w_{edge} - m_{edge})^2}\right)^2 \sigma(w)^2 + \\ \left(\frac{(w_{edge} - t)}{(w_{edge} - m_{edge})^2}\right)^2 \sigma(m)^2.}\end{aligned} \tag{3.29}$$

Fig. 3.14 shows an optimized track produced using the L-BFGS-B optimizer with tracks generated from the interpolation mesh and the aforementioned objective function.

Parameter	Value	
	Proton	Deuteron
ic_min_val (ADC units)	300.0	300.0
ic_max_val (ADC units)	850.0	850.0
n_time_steps	1300	1300
interp_ke_min (MeV)	0.01	0.01
interp_ke_max (MeV)	40.0	80.0
interp_ke_bins	800	1600
interp_polar_min (°)	0.1	0.1
interp_polar_max (°)	179.9	89.9
interp_polar_bins	500	250

Table 3.4 SPYRAL interpolation phase parameters used for the analysis of this experiment. The proton parameters were used for the transfer reaction while the deuteron parameters were used for the elastic and inelastic reactions.

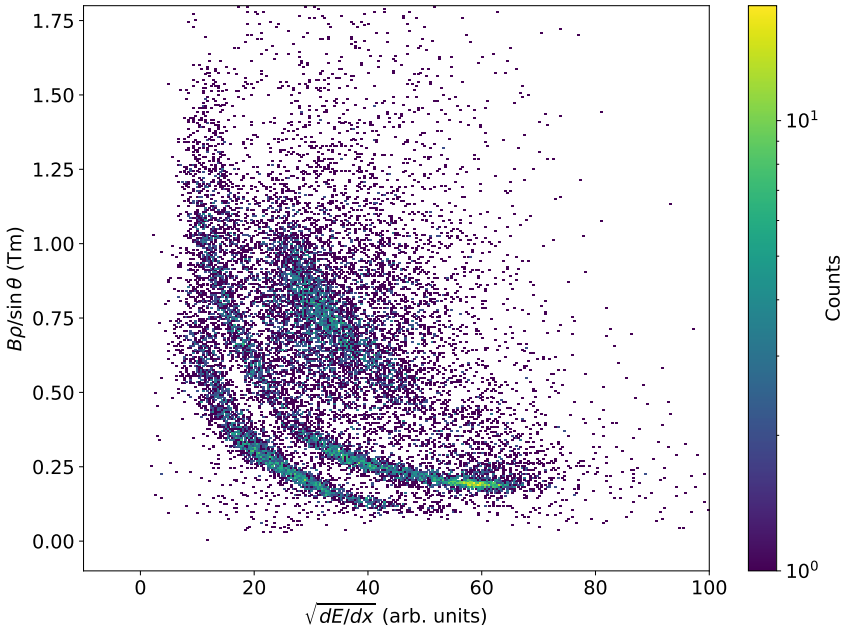

(a)

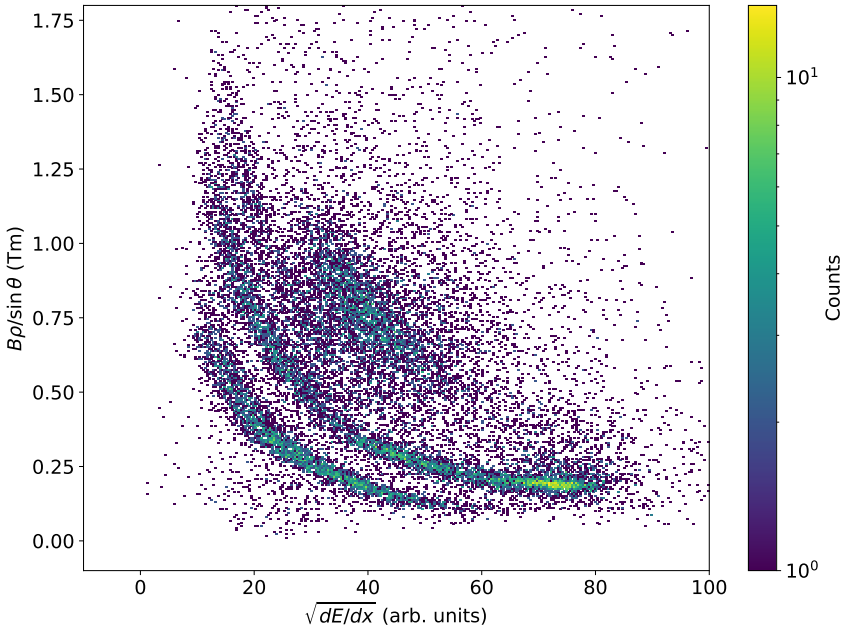

(b)

Figure 3.13 PID plots for run 302 (a) and run 347 (b). Notice the clear difference in the location of the energy loss hot spot of the two deuteron bands. The gain of the MPGDs apparently changed over the course of the experiment.

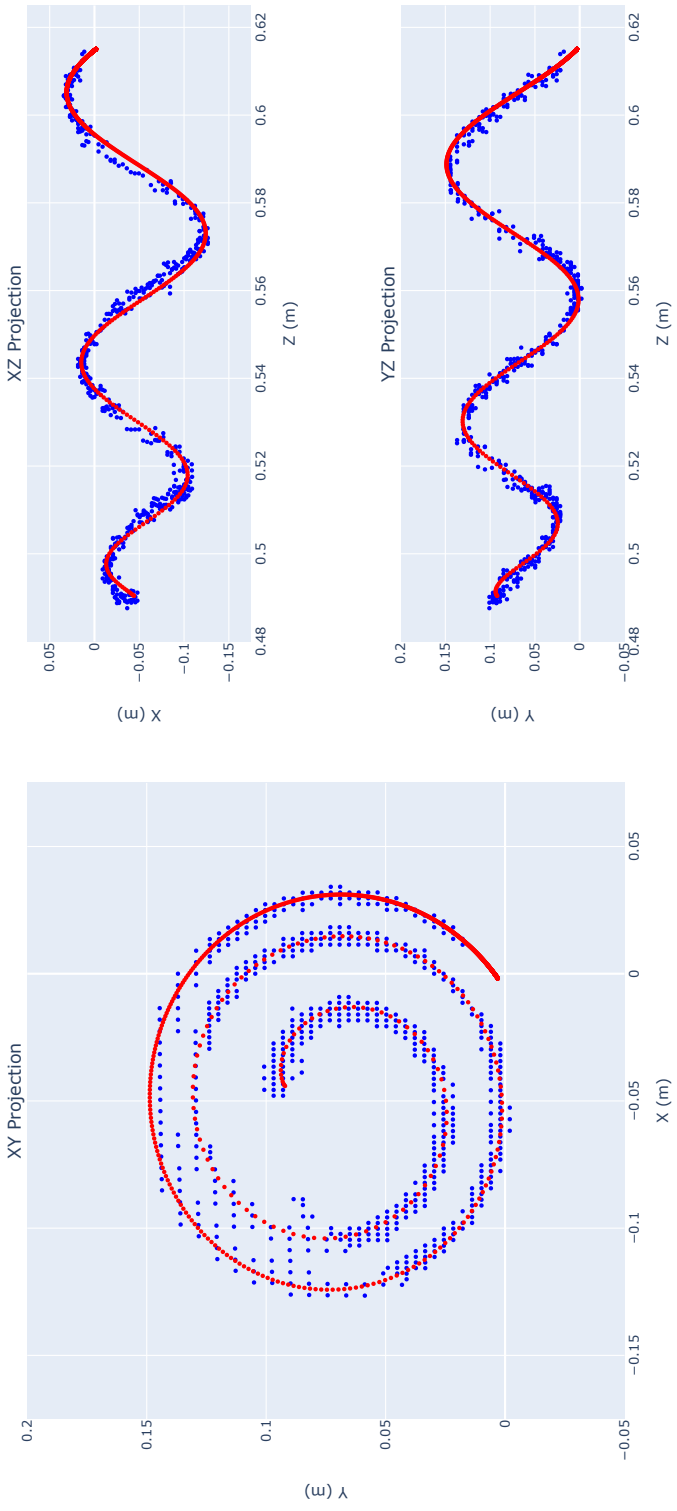

Figure 3.14 L-BFGS-B track optimization to the cluster shown in Fig. 3.9. The blue points form the cluster, while the red points make up the optimized trajectory.

CHAPTER 4

AT-TPC SIMULATIONS

The geometry of the AT-TPC imposes efficiency loses on the detection of specific trajectories from certain reactions. For example, very forward or backward scattered particles will not escape the beam region. The process of analyzing AT-TPC data is novel and complex, as described in Chapter 3, and also introduces efficiency losses. To ensure that SPYRAL produces accurate results, an AT-TPC simulation framework called ATTPC_ENGINE [29] was developed by Gordon McCann and the author in Python with the primary focus of extracting efficiency factors. ATTPC_ENGINE is divided into two halves: a kinematics generator and a detector simulator. This chapter discusses the core operating principles of each while leaving out coding specifics.

4.1 Kinematics generator

ATTPC_ENGINE is designed for two-body nuclear reactions with a stationary target where one of the products can undergo a decay chain. Decays are modeled to happen instantaneously with two nuclei in the exit channel, so three-body or more decays can only be modeled sequentially and not democratically. ATTPC_ENGINE randomly samples the kinematic phase space in the center-of-momentum (CM) frame of the reaction and decay products.

The reaction vertex is first sampled before any kinematic parameters. The z-coordinate is restricted to be within the length of the AT-TPC and is taken from a uniform distribution. The kinetic energy of the beam nucleus is corrected by subtracting the energy lost traveling through the gas to reach this z-coordinate using the Python package PYCATIMA [27]. The x- and y-coordinates are restricted to the beam emittance whose boundary is modeled as a circle. The xy-position is found by normally sampling r along the circle's radius and uniformly sampling an angle Θ from $0 - 2\pi$. The x- and y-coordinates are then

$$x = r \cos\Theta, \tag{4.1}$$

$$y = r \sin\Theta. \tag{4.2}$$

The kinematic parameters are not all sampled for the same reaction or decay product. The

reaction and each decay only require one product be specified while the other is inferred from the conservation of proton and neutron numbers. The input product of each step has the cosine of its polar angle uniformly sampled to ensure the reaction is isotropic in 3D space. Its azimuthal angle is uniformly sampled from $0 - 2\pi$ as well. The inferred product has its excitation energy sampled from the input distribution, e.g. a Gaussian. These constitute all the sampled parameters for the input reaction and decays.

Reaction and decay products cannot have any arbitrary combination of energies due to energy conservation of the system. Because the excitation energy of products are sampled in ATTPC_ENGINE, it is possible that a reaction/decay is illegal by violating conservation of energy. For an n-body reaction, the total CM energy E_{cm} must be greater than or equal to the sum of the product rest energies. In ATTPC_ENGINE we have the reaction $a + b \rightarrow A + B$ where a is the projectile with kinetic energy K_a and b is the stationary target. For this reaction

$$E_{cm} \geq (m_A + m_B)c^2 \tag{4.3}$$

where the m denote rest masses and c is the speed of light. E_{cm} can be calculated from the rest masses of the reactants and the sampled kinetic energy of the beam as

$$E_{cm} = \sqrt{(m_a + m_b)^2c^4 + 2m_bc^2K_a}. \tag{4.4}$$

The energy condition of a decay requires the rest mass of the parent to be greater than or equal to the sum of its daughters' rest masses. Denoting the decay as $c \rightarrow D + E$, the condition is

$$m_c \geq m_D + m_E. \tag{4.5}$$

If the sampled excitation energies do not satisfy Eq. 4.3 and/or Eq. 4.5 for each appropriate step, the reaction and decays are sampled again.

Assuming a valid reaction and decays were sampled, ATTPC_ENGINE calculates the laboratory four-momentum of each nucleus for all steps excluding the parent nuclei of a decay since they are not part of the final products. The four-momentum of the target nucleus and beam nucleus are trivial: the target is stationary and only has an energy component equal to is rest mass while the

beam nucleus has momentum only in the z-direction that is found from its input kinetic energy. If A is the angle-sampled reaction product, it has a CM energy E_A given by

$$E_A = \frac{1}{2E_{cm}}(m_A^2c^4 - m_B^2c^4 + E_{cm}^2) \tag{4.6}$$

where m_B includes the sampled excitation energy. The magnitude of A's three-momentum $|\overrightarrow{p_A}|$ is found using the energy-momentum relation and its components are

$$\overrightarrow{p_A} = \begin{pmatrix} |\overrightarrow{p_A}| \sin\theta\cos\phi \\ |\overrightarrow{p_A}| \sin\theta\sin\phi \\ |\overrightarrow{p_A}| \cos\theta \end{pmatrix} \tag{4.7}$$

where θ and ϕ are its sampled polar and ϕ azimuthal angles, respectively. Together, eqs. 4.6 and 4.7 compose the four-momentum of A in the CM frame. These equations also work for the angle-sampled decay product D. The Python package VECTOR [30] transforms both to the laboratory frame, using the beam and target four-momenta for reaction products and the parent four-momentum for a decay product. VECTOR then uses four-vector math to determine the laboratory four-momentum of the other energy-sampled reaction/decay product. The kinematics generator writes the four-momenta of the beam, target, and products along with the reaction vertex location to a dataset in an output HDF5 file for each generated event.

4.2 Detector simulation

The detector simulation of ATTPC_ENGINE takes an HDF5 file of generated events from the kinematics generator and applies AT-TPC detector effects to them. The output is the simulated point cloud of each generated event in the SPYRAL format for easy and guaranteed compatibility with the SPYRAL analysis.

For a generated event, the trajectory of each nuclear product in the AT-TPC is determined by solving the equations of motion given by Eq. 3.26 with initial conditions defined by the product's four-momentum. The track is constrained by the physical boundaries of the AT-TPC and has a similar stopping condition to that described in Section 3.6.1. The energy lost at each point in the trajectory must be calculated. The ODE solver returns the velocity $\vec{v}$ of the nucleus at a point n in

its trajectory that is related to its kinetic energy E_n via

$$E_n = mc^2(\gamma - 1) \tag{4.8}$$

where

$$\gamma = \frac{1}{\sqrt{1 - (|\vec{v}|/c)^2}}. \tag{4.9}$$

The energy lost at point n, ΔE_n, is defined as

$$\Delta E_n = E_{n-1} - E_n. \tag{4.10}$$

We write "defined" because, strictly speaking, this is not correct. Energy loss occurs stochastically between the points $n-1$ and n whereas this definition implies it all occurred at n. In reality this is not a problem since we can make the time step of the ODE solver very small. From this definition it is also apparent that the first point in the trajectory does not have any energy loss.

The number of electrons made at point n in the nucleus' trajectory is found by sampling a normal distribution with mean μ and standard deviation σ given by

$$\mu = \frac{\Delta E_n}{w}, \tag{4.11}$$

$$\sigma = \sqrt{f\mu} \tag{4.12}$$

where w is the W-value of the gas and f is the Fano factor. The W-value is the average energy needed to create an electron-ion pair in the gas, so μ is the expected number of electrons. The formation of electrons by the nucleus losing energy is statistical and we should not expect exactly μ electrons to be created, hence the sampling of a normal distribution. It turns out the number of electrons liberated deviates from purely statistical predictions [31]. The Fano factor attempts to capture this behavior by modifying the statistically predicted standard deviation and depends on the gas [31]. After sampling, the number of electrons made at each point is multiplied by the gain factor of the MPGDs.

The electric field of the AT-TPC drifts the electrons made at point n towards the pad plane. We define the spatial coordinates of n, in meters, as (x_n, y_n, z_n) and use the same coordinate system as

the analysis described in Section 3.2.2. Thus, z_n is given relative to the window of the AT-TPC and is converted to exact time buckets t via

$$t = \frac{l - z_n}{v_e} + m_{edge} \tag{4.13}$$

where l is the length of the AT-TPC in meters, v_e is the electron drift velocity in meters per time bucket, and m_{edge} is the micromegas edge time bucket. ATTPC_ENGINE determines the pad each electron hits depending on the input ratio of the transverse diffusion to the charge mobility, d_t, of the gas. If the transverse diffusion is zero, then all electrons made at point n are projected onto the pad plane with xy-coordinates given by (x_n, y_n). If d_t is not zero, the electrons made at point n are smeared onto the pad plane according to a discretized uniform 2D Gaussian distribution. Its mean is at (x_n, y_n) and its standard deviation is

$$\sigma_t = \sqrt{\frac{2 d_t v_e t}{|\vec{E}|}} \tag{4.14}$$

where $\vec{E}$ is the electric field of the AT-TPC. Electrons that hit the beam pads are not recorded because these pads were suppressed and not used in the experimental data. Regardless of the value of d_t, the discrete time bucket of each electron recorded by GET is found by flooring Eq. 4.13.

Transporting the liberated electrons from all recorded nuclear products in the event to the pad plane results in the raw trace for each pad. The raw trace of a pad consists of the number of electrons that hit it in each of its 512 time buckets. Actual AT-TPC pad traces do not output how many electrons a pad saw in each time bucket but rather their induced signal in ADC units. Here an important choice has been made with ATTPC_ENGINE. To faithfully create the point cloud requires convolution of the raw trace with the GET response function and performing the point cloud phase of SPYRAL on the result. This is not an attractive option. First, it requires explicitly coupling ATTPC_ENGINE to SPYRAL. Changes in SPYRAL might require changes in ATTPC_ENGINE. Second, the point cloud phase of SPYRAL is the slowest portion of the analysis pipeline. Hundreds of thousands of events may need to be simulated to adequately explore the phase space of a reaction, which is orders of magnitude more than the the number of events actually measured. For these

reasons, ATTPC_ENGINE does not perform the full convolution and peak finding analysis of the point cloud phase; instead, it estimates their results.

Every time bucket in a trace that sees electrons is made a point in the point cloud. Its z-position is found from Eq. 3.6 using a randomly sampled time within its time bucket (see Section 3.2.2) and its x- and y-coordinates are found from its pad's centroid. The charge deposited at the point is estimated from the amplitude of the GET theoretical response function

$$r(t) = A \exp\left(-3\frac{t}{\tau}\right)\left(\frac{t}{\tau}\right)^3 \sin\left(\frac{t}{\tau}\right) \tag{4.15}$$

where A converts from electrons to ADC units and τ is the peaking time of the electronics [32]. A is explicitly given by

$$A = 4095\frac{eN_e}{g_{amp}} \tag{4.16}$$

where e is the electron charge, N_e is the number of electrons in the time bucket, and g_{amp} is the GET amplifier gain in units of Coulombs. τ is found from

$$\tau = t_{shaping} \cdot f_{clock} \tag{4.17}$$

where $t_{shaping}$ is the GET shaping time and f_{clock} is the GET clock frequency. For each point in an event's cloud, ATTPC_ENGINE writes the position, deposited charge, and any other required SPYRAL attributes, like the size of a point's pad, to a dataset in an HDF5 file. This is done for each simulated event that has a point cloud of at least one point.

4.3 Efficiency factors

ATTPC_ENGINE was used to simultaneously correct efficiency losses due to the geometry of the AT-TPC and the SPYRAL analysis. ATTPC_ENGINE simulated 3 million ^{10}Be+d events for both the elastic and first inelastic states of ^{10}Be and 1.5 million ^{10}Be+d events for each state of ^{10}Be. The standard deviation of the normal distribution for sampling the xy-coordinates of the reaction vertices was one-third of the beam region radius, which was 2 cm. Tables 4.1 and 4.2 list the detector and electronics parameters used by ATTPC_ENGINE, respectively. The window and micromegas edge time buckets chosen were the average of those across all the experimental runs. For each event, the

polar angle was simulated from $0 - \pi$ in the CM frame. The excitation energy of the Be species was sampled from a Gaussian distribution for states with intrinsic widths less than 1 eV and a relativistic Breit-Wigner for those with larger widths.

The simulated point clouds were analyzed using Spyral with the same parameters as for the experimental data given in Chapter 3. For each reaction channel, a histogram of the CM scattering angles of its Be isotope was then created from the Spyral analysis (see Section 5.4 for more details). Denote such a histogram by P and its i-th bin by $P(i)$. Similarly, let S represent the histogram of simulated Be CM scattering angles and its i-th bin by $S(i)$. To be clear, S is made from all the attpc_engine simulated events produced from the kinematics generator, and P are those that then survived the detector effects of attpc_engine and the Spyral analysis. To compute the efficiency factors, P and S both must have the same number of bins over the same angular range. The efficiency factor of the i-th bin $e(i)$ is given by

$$e(i) = \frac{P(i)}{S(i)}. \tag{4.18}$$

For the efficiency factors to be accurate, S must be made with the same gates used in the actual analysis. These are detailed in Section 5.1. The error of each efficiency factor $\sigma(e(i))$ results from propagating the statistical error of the counts in each histogram bin through Eq. 4.18. Thus,

$$\sigma(e(i)) = e(i)\sqrt{\frac{1}{P(i)} + \frac{1}{S(i)}}. \tag{4.19}$$

Figs. 4.1 and 4.2 show the relevant subset of the efficiency factors for the states of ^{10}Be and ^{11}Be seen in this experiment, respectively. A dip in efficiency occurs for low CM scattering angles for all states, although at different places, due to the detected target-like product becoming less energetic (this dip is off the graphs for the ground and 0.32 MeV states of ^{11}Be). Decreasing the target-like product's energy shrinks its phase space to leave the beam region and be detected. The angular threshold where detection ceases depends on the reaction channel. For the 1.78 MeV state and above in ^{11}Be, another efficiency drop is seen for larger CM scattering angles. In these regions, the target-like product scattered at and near 90° with velocities perpendicular and nearly perpendicular to the magnetic field, confining its motion to a plane. The pre-fitting process described in Section

3.4 fails for such trajectories, namely the vertex z-coordinate extraction from the linear regression given by Eq. 3.14 as z is constant or almost so. Where the scattering angle of the target-like product approaches 90° depends solely on the reaction channel.

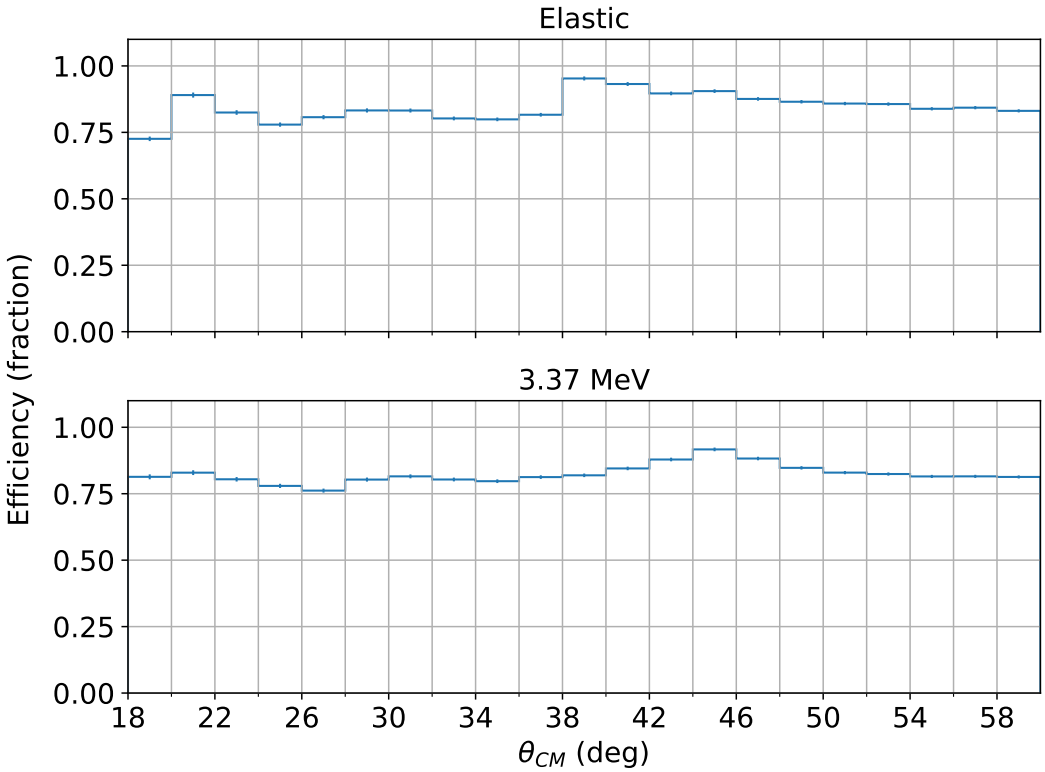

Figure 4.1 Efficiency factors per bin for the angular distributions of the observed states in ^{10}Be seen in this experiment. They were found using ATTPC_ENGINE simulations. Errors are plotted but small.

4.4 CM scattering angle error

Accurate reconstruction of the CM scattering angle of the Be isotope, θ_{CM}, is needed to create its angular distribution (see Eq. 1.5). The ATTPC_ENGINE calculations used for the efficiency factors described in Section 4.3 were also used to calculate the error on its reconstruction. Fig. 4.3 shows a 2D histogram of the reconstructed versus simulated θ_{CM} for the elastic scattering of ^{10}Be+d. Despite a few regions of strange behavior, the reconstruction is generally good but the width of the diagonal line is not constant; the error in θ_{CM} clearly evolves and degrades at larger angles.

Using the language of Section 4.3, the error on θ_{CM} was calculated for the i-th bin of its

respective histogram P and is denoted as $\sigma(\theta_{CM}(i))$. Recall that P is the histogram of all the analysis reconstructed θ_{CM}. If $C(i)$ is the set of the simulated θ_{CM} for all the reconstructed θ_{CM} in $P(i)$, then

$$\sigma(\theta_{CM}(i)) = \text{IQR}(C(i))/2 \tag{4.20}$$

where IQR stands for interquartile range. Graphically, $\sigma(\theta_{CM}(i))$ is half the IQR of all the elements in the horizontal band corresponding to the i-th bin of P in Fig. 4.3. The IQR is a robust measure of dispersion in a data set and is better than the standard deviation in this case because of large outliers seen in Fig. 4.3 away from the diagonal.

Parameter	Value
length (m)	1
efield (V/m)	60,000
bfield (T)	3
mpgd_gain	175,000
diffusion (V)	0
fano_factor	0.2
w_value (eV)	34

Table 4.1 Detector parameters used for the ATTPC_ENGINE simulations of this experiment.

Parameter	Value
clock_freq (MHz)	3.125
amp_gain (fC)	900
shaping time (ns)	1000
micromegas_edge (time buckets)	62
windows_edge (time buckets)	396
adc_threshold (ADC units)	30

Table 4.2 Electronics parameters used for the ATTPC_ENGINE simulations of this experiment.

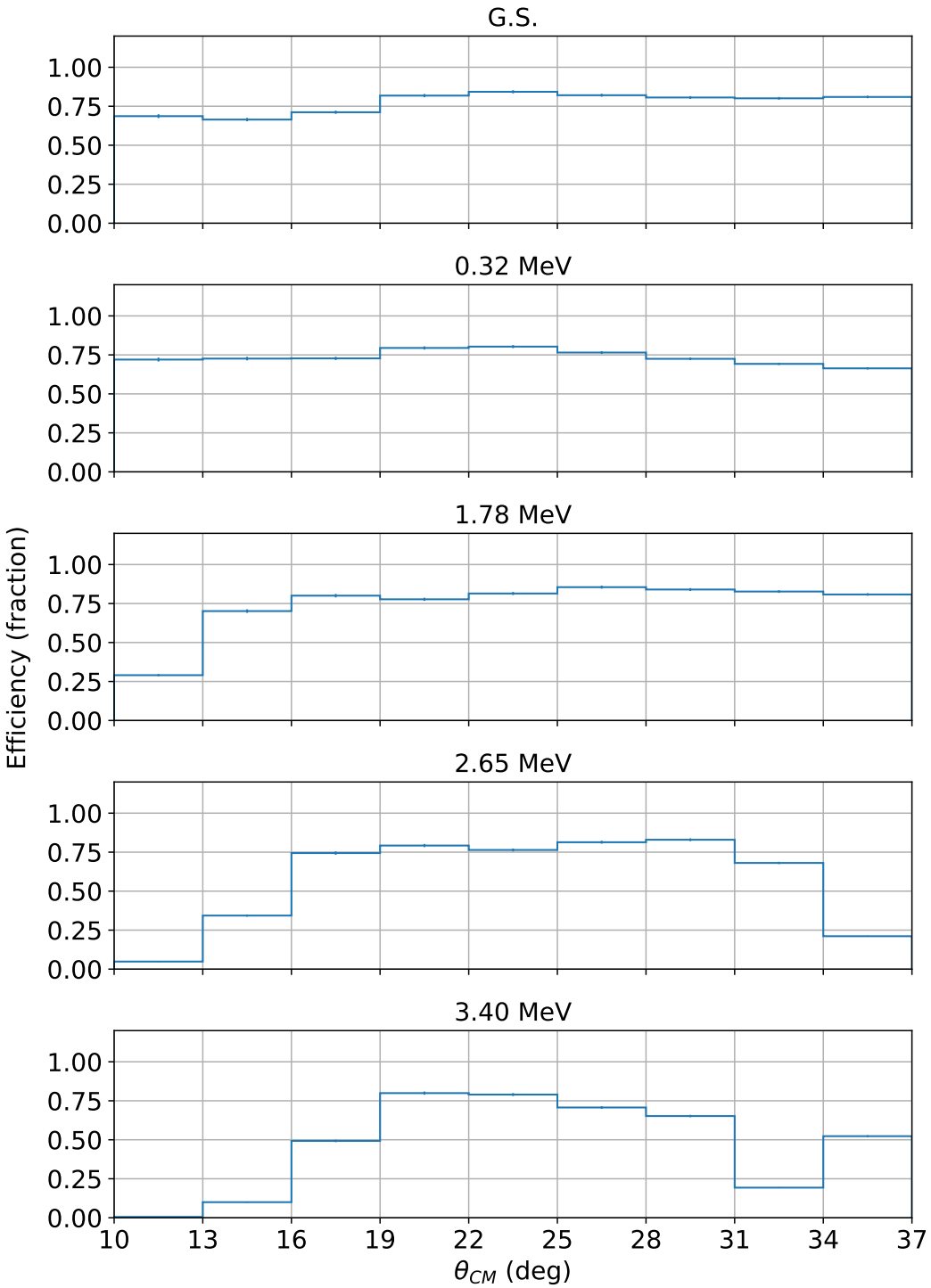

Figure 4.2 Efficiency factors per bin for the angular distributions of the observed states in ^{11}Be seen in this experiment. They were found using ATTPC_ENGINE simulations. Errors are plotted but small.

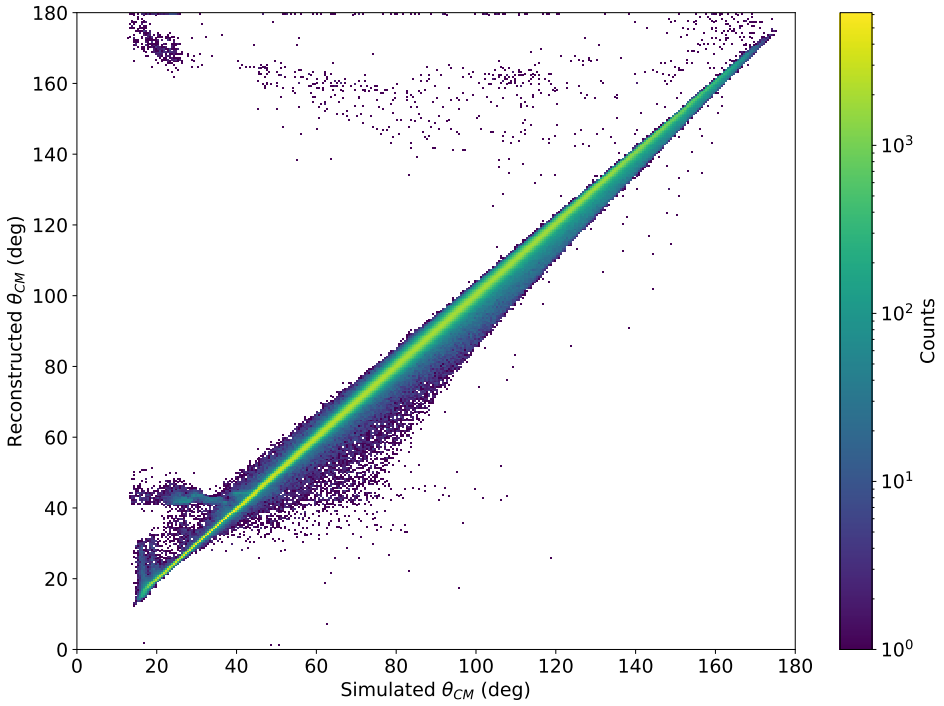

Figure 4.3 Spyral reconstructed θ_{CM} vs. ATTPC_ENGINE simulated θ_{CM} of ^{10}Be elastically scattering on deuterons. The same ATTPC_ENGINE simulated data to determine the elastic scattering efficiency factors was used. Note that there are clearly regions of the phase space where the analysis does worse, such as simulated θ_{CM} near 20°. The width of the hot central band also changes as a function of simulated θ_{CM}, indicating that the resolution is not constant and degrades at larger angles.

CHAPTER 5

EXPERIMENTAL RESULTS

This chapter derives and presents the results from the ^{10}Be(d, p) reaction measured by the AT-TPC. It also discusses results from the ^{10}Be(d, d') reaction that was simultaneously recorded. Elastic cross sections are well known and provide a benchmark to ensure the accuracy of the analysis. They, along with inelastic cross sections, can also provide input for theoretical calculations used to extract spectroscopic factors.

5.1 Gates

Only one gate was applied to the data. The vertex z-position was constrained to 0.004 m $\leq z \leq$ 0.958 m. This range was chosen to exclude nuclear reactions from the two extremities of the AT-TPC on the window and MPGDs.

Another natural gate to consider is on the minimized objective function value returned by the optimizer for each clustered track, which is a figure of merit for the goodness of the minimization. In the case of the SPYRAL analysis, this is the average distance between the points in the clustered track and the generated trajectory. However, the implementation of such a gate is not straightforward. The first problem is determining the limits of a gate on the returned objective function value. We have observed that seemingly small changes in its limits can result in large differences in certain bins of the angular distributions for certain reaction channels. Another problem is propagating this gate to the simulated data used for the determination of the efficiency factors and error on θ_{CM}. As expected, the distribution of minimized objective function values from simulated data is different from that of real data. The values are also typically much smaller. A transformation of this gate from the real to the simulated data would need to be devised, and it is not obvious how to do so.

Still, the minimized objective function value does provide relevant information [1]. If changing the limits of its gate produces drastic differences for some bins in a reaction channel's angular distribution, this implies that the optimizer has difficulties in those regions for that channel and their points should be assigned a larger systematic error. This idea was applied to the angular

[1] We will sidestep the issue of transforming the gate from the real to simulated data by assuming they are the same.

distributions in Section 5.4.

5.2 Kinematics

Figs. 5.1 and 5.2 are kinematic plots of the kinetic energy of the target-like product vs. its laboratory scattering angle for the $^{10}\mathrm{Be}(d,p)$ and $^{10}\mathrm{Be}(d,d')$ reactions, respectively. The

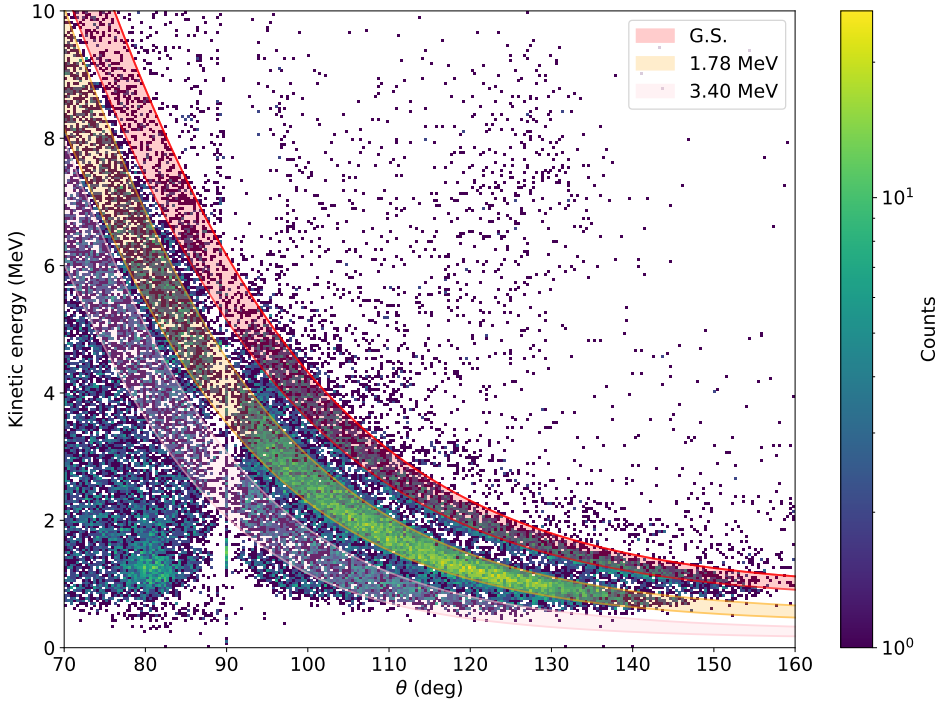

Figure 5.1 Measured kinematics for the $^{10}\mathrm{Be}(d,p)$ reaction. The theoretical kinematic bands are overlaid for the ground, 1.78 MeV, and 3.40 MeV states. The bands for the 0.32 MeV and 2.67 MeV states lie between those shown with significant overlap.

scattering angle of the target-like product was found from its optimized trajectory while its kinetic energy K was calculated from

$$K = \sqrt{(pc)^2 + (mc^2)^2} - mc^2 \tag{5.1}$$

where m is its rest mass, p its momentum from Eq. 3.20, and c the speed of light. The theoretical kinematic lines for some of the states are shown in the figures and are derived from the relativistic conservation of energy and momentum for a two-body reaction. Notice that they are not kinematic lines but bands. This is due to the variety of beam energies present in the AT-TPC that come from the energy lost by the beam particle as it travels through the gas to its reaction vertex.

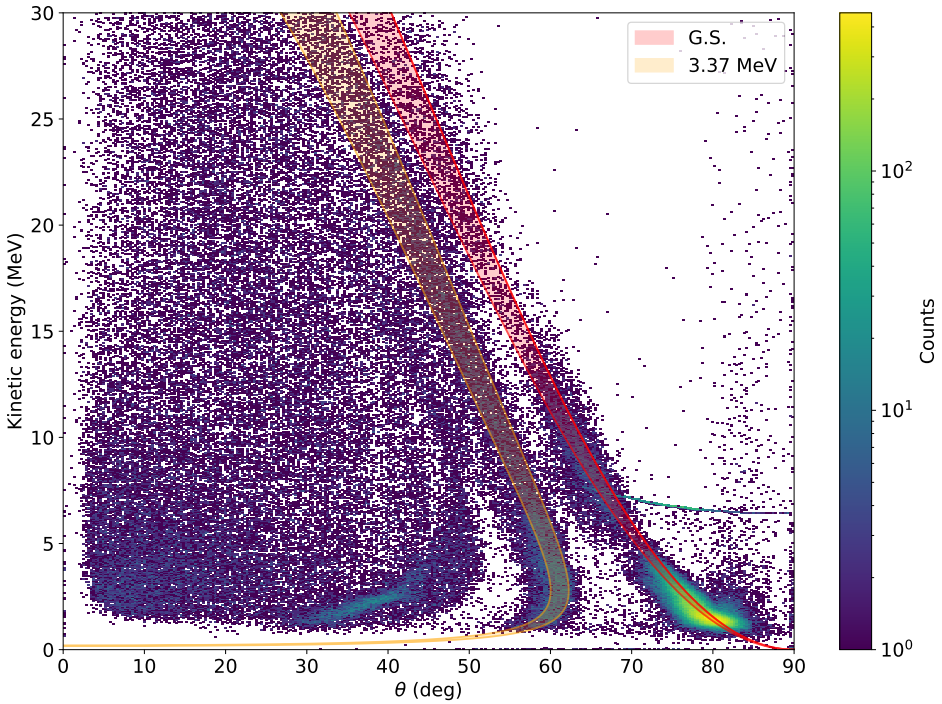

Figure 5.2 Measured kinematics for the ^{10}Be(d, d') reaction. The theoretical kinematic bands are overlaid for the elastic and first inelastic channels.

5.3 Excitation spectra

The ^{10}Be and ^{11}Be excitation spectra were found using Eqs. 1.7-1.9 with the extracted kinematic parameters and are shown in Figs. 5.3 and 5.4, respectively. PYCATIMA corrected the beam energy at the AT-TPC window by the energy lost to reach the vertex position. States are observed in ^{10}Be up to 7.3 MeV [2] and in ^{11}Be up to 3.4 MeV. The full width at half maximum (FWHM) of these states evolves as a function of θ_{CM}, as evident from the kinematic plots shown in Figs. 5.1 and 5.2 (see also the discussion in Section 4.4). The evolution of the FWHM is a manifestation of the complex interplay between the geometric shapes of tracks and how their closest calculated trajectory is optimized by the analysis. The dynamic range of the AT-TPC is incredibly large, recording nuclei from multiple reaction channels with energies ranging from MeV to tens of MeV. Unsurprisingly, and unfortunately, not all regions in this phase space have tracks as equally optimized. FWHM is not a useful metric for the AT-TPC.

[2]The ^{10}Be spectrum was limited to 5.25 MeV because only the elastic and first inelastic states would be fit to determine optical model parameters for reaction calculations as discussed in Section 5.5. However, higher-lying states are observed and their kinematic lines can be seen in Fig. 5.2.

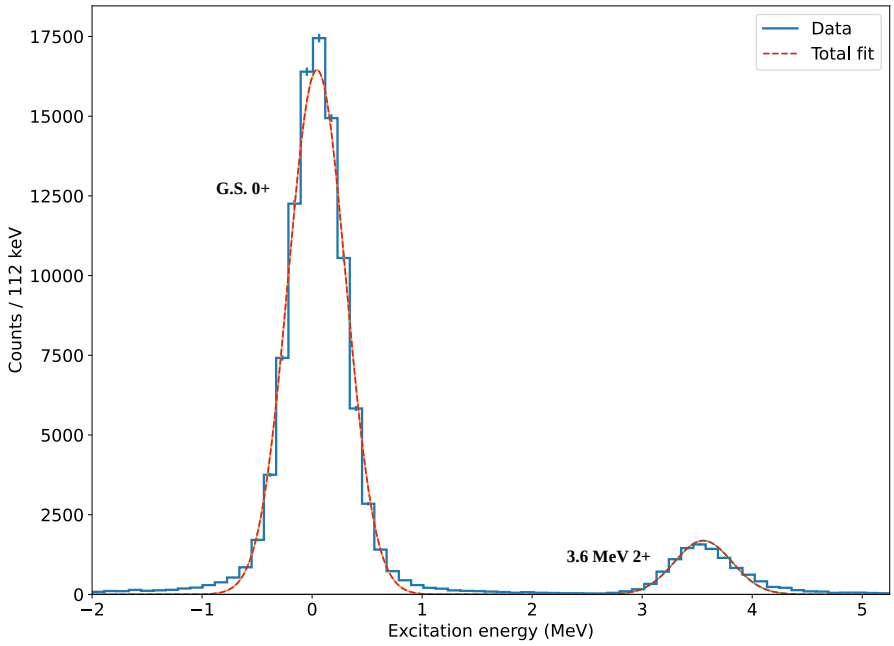

Figure 5.3 ^{10}Be excitation spectrum from 18-60°, inclusively, in the CM frame. The individual fits for each observed state and the total fit to the spectrum are shown, but their heavy overlap makes them hard to distinguish. Indicated energies are from the centroids of the fit.

5.4 Angular distributions

Angular distributions were made using Eq. 1.5. The number of counts per angular bin, $R(\theta_{CM}, \Delta\theta_{CM})$, were found by fitting the bin's excitation spectrum and integrating the counts contained within the state of interest. Figs. 5.5 and 5.6 show the fit to each angular bin for the ^{10}Be(d, d') and ^{10}Be(d, p) reactions, respectively. The excitation energy was restricted to $-2.0\,\text{MeV} \leq E_x \leq 5.25\,\text{MeV}$ for ^{10}Be and $-1.0\,\text{MeV} \leq E_x \leq 4.3\,\text{MeV}$ for ^{11}Be. States with lifetimes greater than a femtosecond were fit with Gaussians while those with less were fit with Voigts. The long-lived states have a shape dominated by the Gaussian-like response of the detector/analysis and the short-lived states have a shape made from the convolution of their intrinsic Breit-Wigner shape with this Gaussian-like response. The excitation spectra for ^{10}Be and ^{11}Be in Figs. 5.3 and 5.4, respectively, show the total fits with the aforementioned profiles for each state. For the ^{11}Be spectrum, a Voigt term was added above the 3.40 MeV state to capture possible counts from the 3.89 MeV and 3.96 MeV states. However, because these states cannot be separated by the

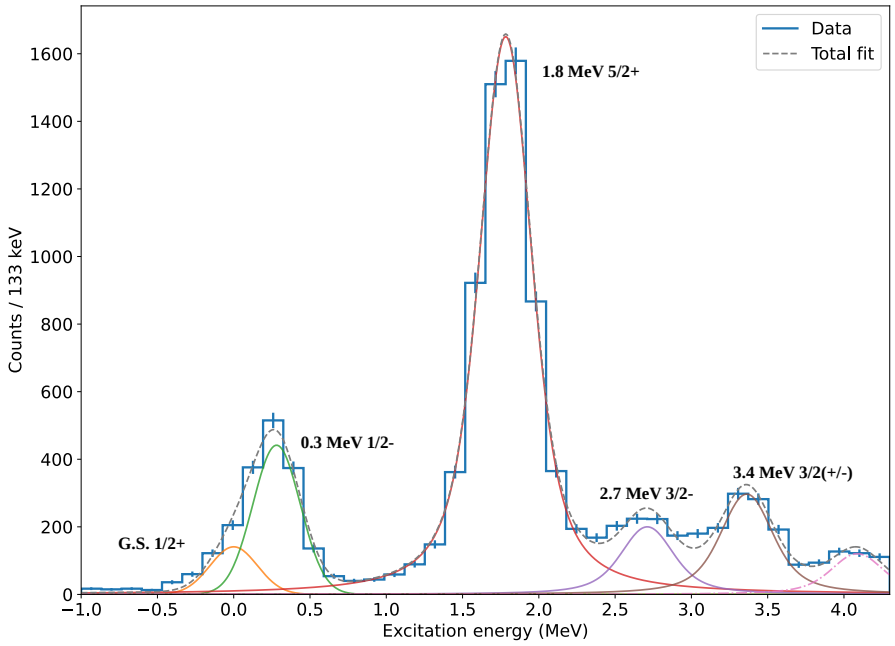

Figure 5.4 ^{11}Be excitation spectrum from 19-31°, inclusively, in the CM frame. The individual fits for each observed state, a term for states above 3.40 MeV, and the total fit to the spectrum are shown. Indicated energies are from the centroids of the fit.

resolution of the AT-TPC and lie near the edge of the experimental acceptance, no conclusions are drawn from them.

For convenience, we will move units around in the denominator of Eq. 1.5 so that I is the number of ^{10}Be beam particles per time and n is the areal density of the target nuclei seen by the beam. I was found using unreacted beam events. The counts in the ^{10}Be peak of Fig. 2.6 were summed from 300-850 ΔE. Note this same IC gate was applied to the data during the interpolation phase of the analysis described in Section 3.6 (see Table 3.4). The areal density of the gas n was trivially determined from the ideal gas law and the length of the AT-TPC active volume. It is apparent from Fig. 2.6 that the ^{10}Be and ^{10}B peaks were not completely separated. To estimate the amount of ^{10}B that leaked into the ^{10}Be gate, these two peaks were fit with Gaussians and the one corresponding to ^{10}B was integrated over the gated region. The leakage was less than 1.3% of the total summed ^{10}Be counts and was subtracted.

Figs. 5.7, 5.8, and 5.9 show the measured angular distributions for the indicated states of

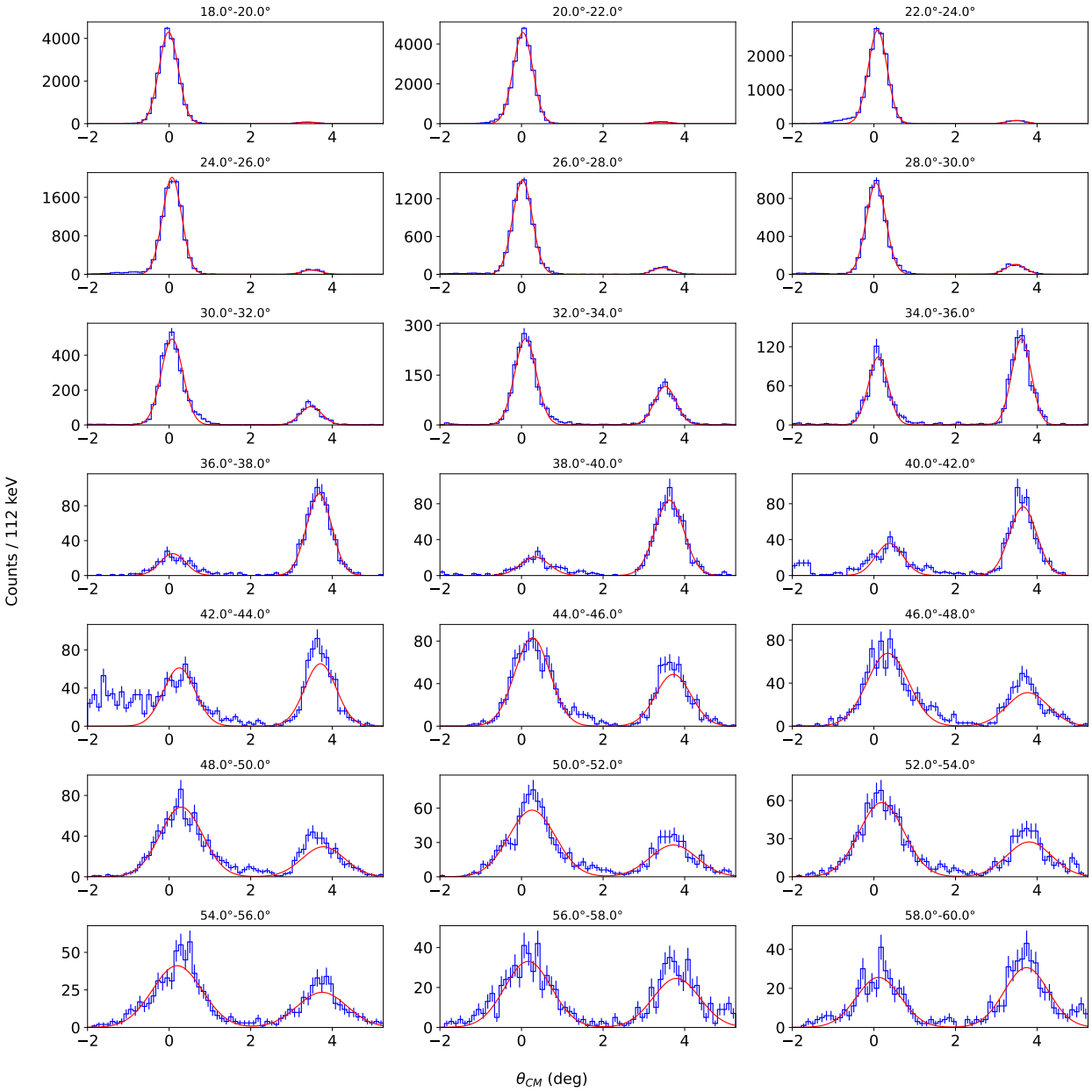

Figure 5.5 Total fit to each angular bin for the ^{10}Be(d, d') reaction. The fit includes the elastic and first inelastic states of ^{10}Be.

^{10}Be and ^{11}Be populated in this experiment with their efficiency factors applied (see Section 4.3).

The horizontal error bar of each bin results from the uncertainty in the reconstruction of θ_{CM} (see Section 4.4). The vertical error results from propagating various uncertainties through Eq. 1.5 using the error propagation formula. For each bin, these include the statistical uncertainty of its counts along with the error from its efficiency factor given by Eq. 4.19. The error on the number of beam particles I was less than 1% and I was so large that its contribution to the total

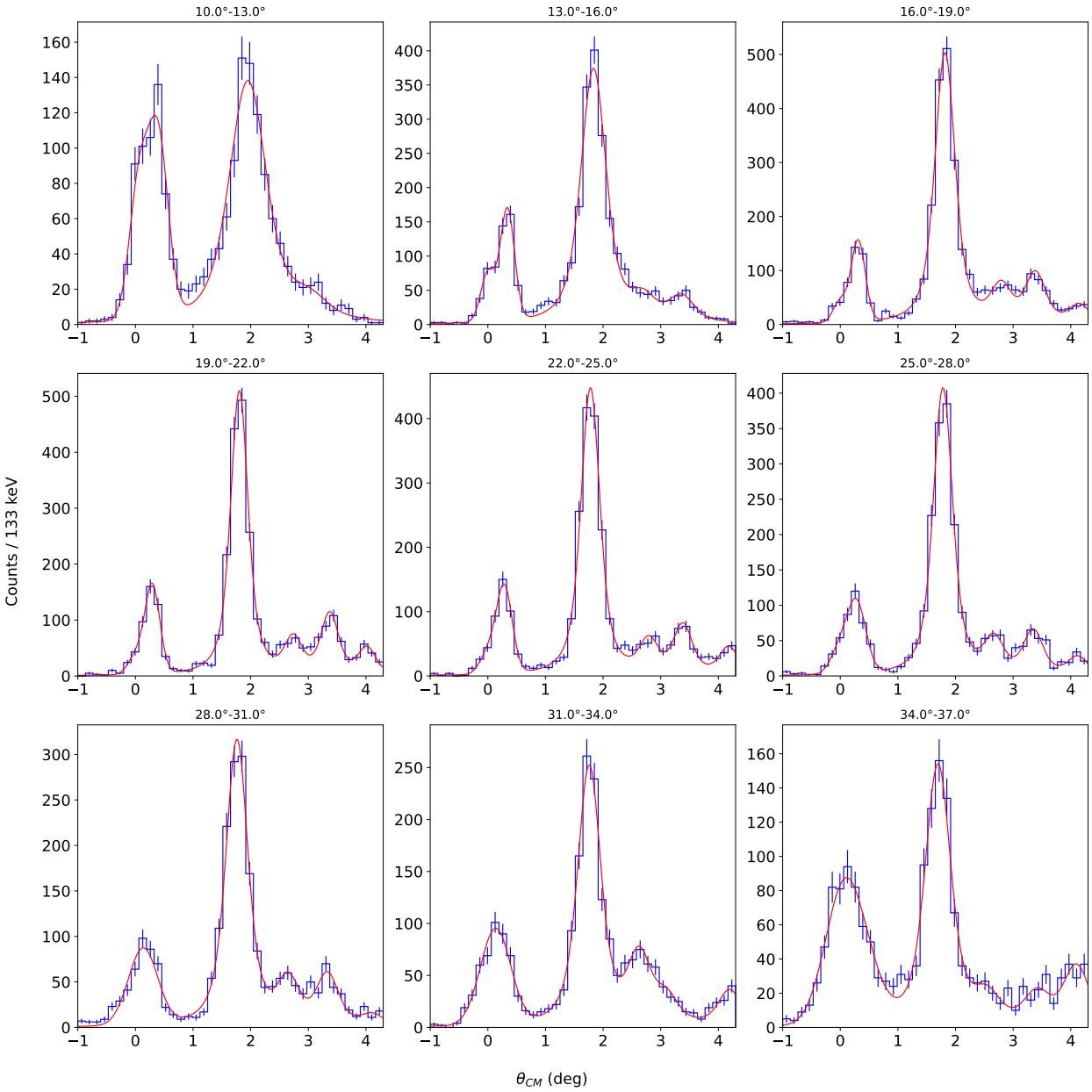

Figure 5.6 Total fit to each angular bin for the ^{10}Be(d, p) reaction. The fit includes the first five states of ^{11}Be and a term for the states above 3.40 MeV.

vertical error was negligible, thus it was safely ignored. The areal density of the target nuclei n was calculated using the ideal gas law and depended on the pressure and temperature of the AT-TPC active volume. The pressure was kept constant via continuous feedback from the vacuum system and assigned no error. The temperature was assumed to be 273.15 K but was not measured, so no error was assigned.

The vertical error bars also take into account the sensitivity of the bin to a gate on the minimized

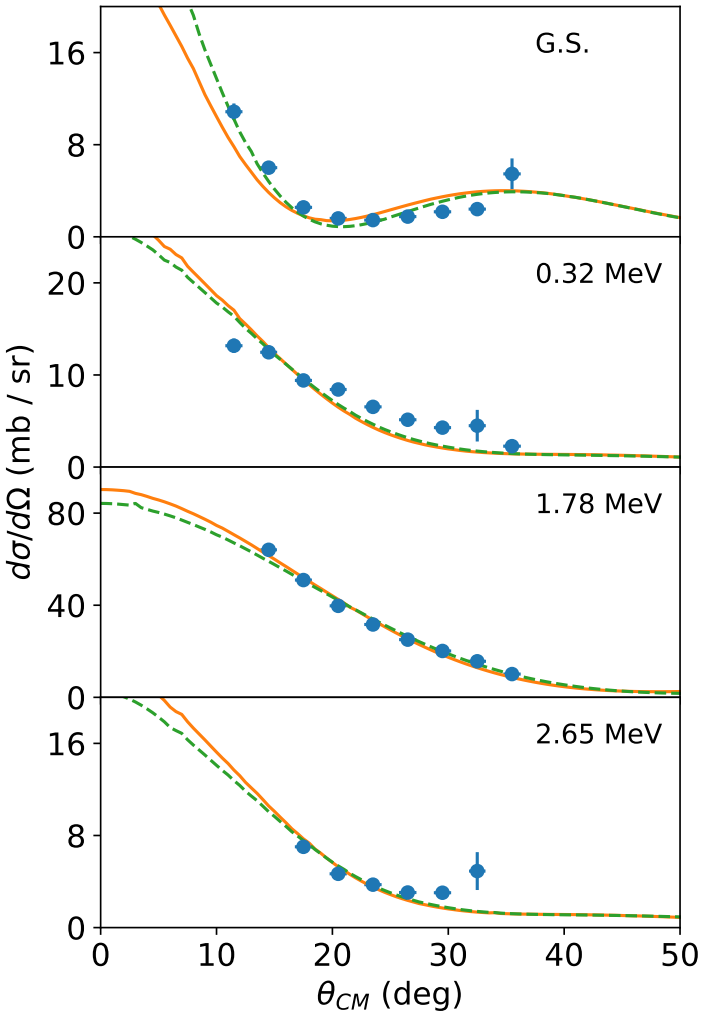

Figure 5.7 Measured angular distributions for the first four states of ^{11}Be compared to DWBA calculations. The calculations used the beam energy at the center of the AT-TPC and were scaled by their spectroscopic factors. The orange solid lines use the DA1p OMP, while the green dotted lines use the An Cai OMP. The elastic fit calculations are not shown because they are nearly identical to the An Cai.

objective function value d_{avg}, although the final distributions included no such gate. This was done to find regions of the distributions where the optimizer performs poorly (see Section 5.1). Fig. 5.10 shows the histograms of d_{avg} for the ^{10}Be and ^{11}Be events. The gate was set such that $d_{avg} \leq 10^{-4}$ m. The resulting gated angular distributions were subtracted from the ungated

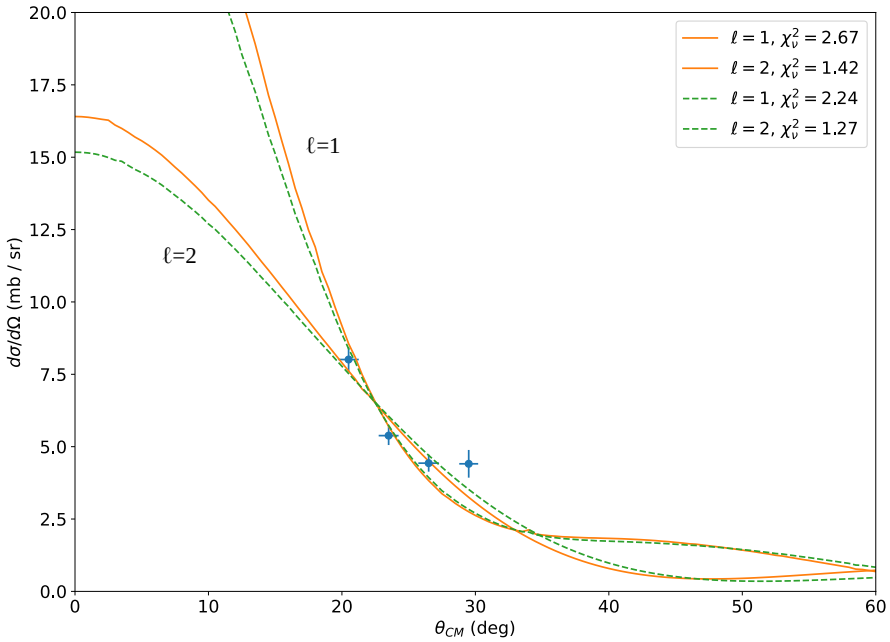

Figure 5.8 Measured angular distribution for the 3.40 MeV state of ^{11}Be compared to DWBA calculations. The calculations used the beam energy at the center of the AT-TPC and were scaled by their spectroscopic factors. The orange solid lines use the DA1p OMP, while the green dotted lines use the An Cai OMP. The elastic fit calculations are not shown because they are nearly identical to the An Cai. The two different bands correspond to either negative ($\ell = 1$) or positive ($\ell = 2$) parity. Because the points measured are few and not near a minima, the parity cannot be definitely determined from the shape. The reduced chi-square values do favor a positive assignment, however.

distributions. Their differences were added in quadrature to the other aforementioned errors.

The number of bins in each distribution is not the same. This is primarily due to the efficiency of the detector not being constant for each reaction channel as illustrated in Figs. 4.1 and 4.2.

5.5 Extraction of spectroscopic factors

Spectroscopic factors were derived for the states of ^{11}Be from their measured angular distributions and theoretical DWBA calculations with Eq. 1.12. The DWBA calculations were performed with the finite-range code PTOLEMY [33] using the AV18 deuteron wave function [34]. These calculations require the excited states of ^{11}Be to be bound, which only its ground and 0.32 MeV states are. The unbound states were given a -200 keV binding energy to extend these DWBA calculations by a simple, but by no means completely correct, method. The Koning-Delaroche [35] global optical model potential (OMP) was used in the outgoing channel. The DA1p [36] and An Cai

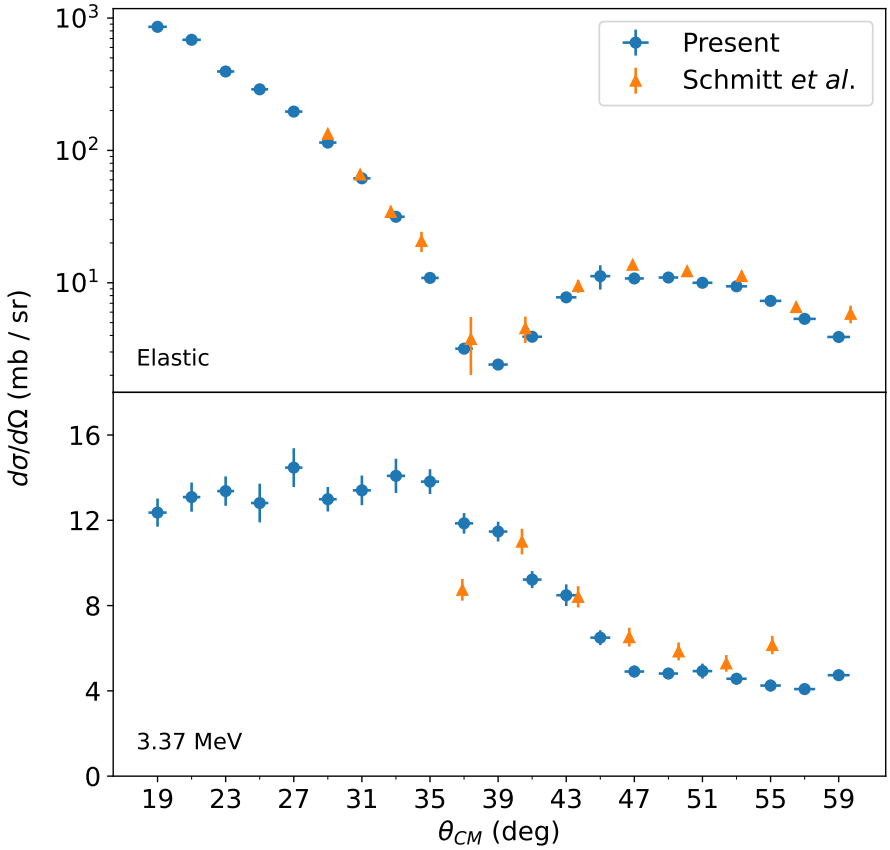

Figure 5.9 Measured angular distributions for the elastic and first inelastic states of ^{10}Be compared to those measured by Schmitt *et al.* [1].

[37] OMPs were used for the incoming channel. Because the ^{10}Be(d, d') reaction was measured simultaneously, the elastic and inelastic cross sections were also used to extract an OMP. PTOLEMY cannot do a simultaneous fit to both states, so Table 5.1 presents the optimized parameters fit to only the elastic channel. These fits used the DA1p parameters as initial values. Fig. 5.11 shows one of the fit OMPs to the measured elastic angular distribution.

The beam energy for the DWBA calculations is complicated by the fact that the beam particle lost energy traversing the large AT-TPC active volume to reach its reaction vertex. The ^{10}Be beam energy varied from 9.3 MeV/u at the entrance window to 8.1 MeV/u at the micromegas. This energy difference affects the amplitude and shape of the calculated angular distributions, and the question

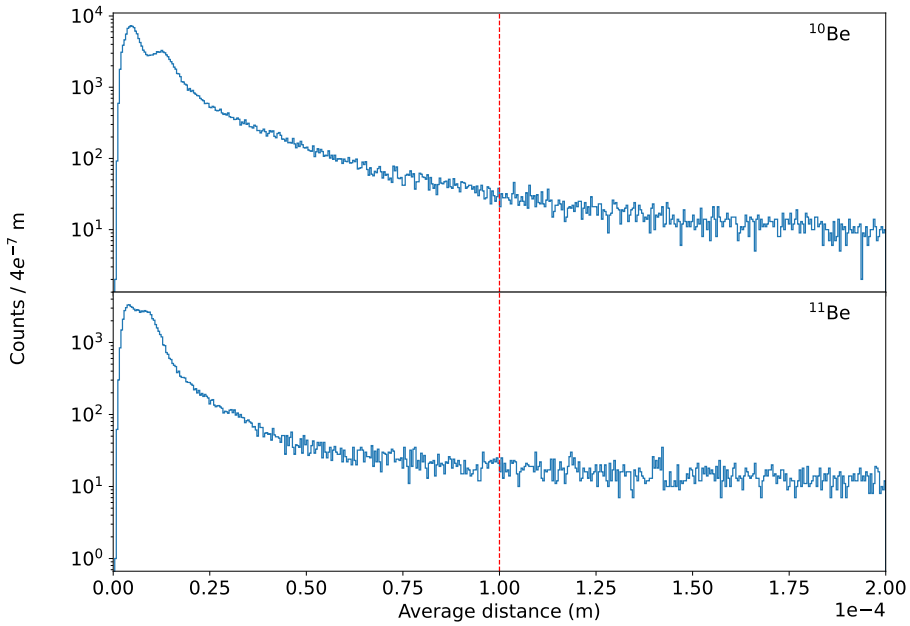

Figure 5.10 Histograms of the minimized objective function value for all ^{10}Be events (top) and ^{11}Be events (bottom). The red dotted line is where the gate was made for the sensitivity analysis.

Beam energy (MeV/u)	V_v (MeV)	r_v (fm)	a_v (fm)	W_v (MeV)	r_w (fm)	a_w (fm)	W_s (MeV)	r_s (fm)	a_s (fm)
9.3 (window)	96.207	2.146	0.822	3.336	3.568	1.206	2.903	4.097	0.610
8.7 (midpoint)	97.554	2.247	0.717	10.576	3.342	0.659	3.355	4.058	0.870
8.1 (micromegas)	101.220	1.857	0.836	6.157	1.859	0.622	2.135	4.520	0.964

Table 5.1 OMPs determined from fitting the elastic scattering angular distribution at different ^{10}Be beam energies corresponding to the indicated locations in the AT-TPC. There were no real nor imaginary spin-orbit potentials and r_c was fixed to 2.801 fm.

becomes what energy should be used. This is directly related to the fact that the AT-TPC actually probes both the angular and energy dependencies of the cross section simultaneously. The best way to handle the explicit energy dependence would be to the bin cross section in both angle and energy (or, equivalently, z-vertex position). This was not possible for this experiment because the statistics were too low. Therefore, the angular distributions reported by this thesis include events with beam energies from the entire range of the detector and are energy integrated. Thus, no beam energy will be entirely correct for the extraction of spectroscopic factors.

With this important limitation understood, we make the compromise of taking the beam energy

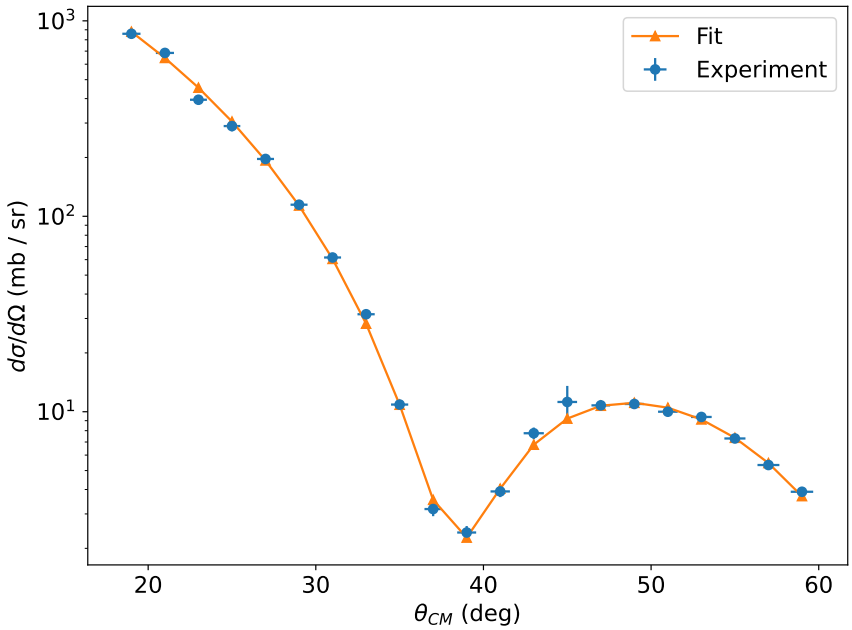

Figure 5.11 Elastic angular distribution plotted with its fit that used the beam energy at the middle of the At-TPC.

at the center of the AT-TPC to capture the "average" behavior. This can be crudely justified: if the cross section changes slowly as a function of energy, we should expect that roughly half the events will be within the first and last halves of the AT-TPC. To provide bounds on the spectroscopic factors, DWBA calculations were also performed with the beam energies at the beginning and end of the detector. Thus, three DWBA calculations for each state were fit to its measured angular distribution with a scaling factor (the spectroscopic factor) that was optimized by a least-squares algorithm. Table 5.2 presents the spectroscopic factors for the states of ^{11}Be whose angular distributions were measured by this thesis experiment. The DWBA calculations for the midpoint of the AT-TPC, with their spectroscopic factors applied, are plotted on the angular distributions in Figs. 5.7 and 5.8. These figures do not plot the calculations from the OMP found by fitting the elastic channel because, once scaled by their spectroscopic factors, they are nearly identical to those from the An Cai OMP.

5.6 Discussion of results

The average derived ^{11}Be spectroscopic factors from Table 5.2 can be compared to those in Table 5.3, which lists the factors found from other experiments and predicted from shell model

E_x (MeV)	ℓ	$n\ell j$	DA1p	An Cai	Elastic fit	Average
0	0	$1s_{1/2}$	$0.92^{+0.15}_{-0.18}$	$1.00^{+0.18}_{-0.20}$	$1.03^{-0.23}_{-0.51}$	$0.98^{+0.03}_{-0.30}$
0.32	1	$0p_{1/2}$	$0.71^{+0.08}_{-0.08}$	$0.55^{+0.08}_{-0.07}$	$0.66^{+0.14}_{-0.09}$	$0.64^{+0.10}_{-0.08}$
1.78	2	$0d_{5/2}$	$0.82^{+0.06}_{-0.06}$	$0.65^{+0.07}_{-0.07}$	$0.77^{+0.07}_{-0.06}$	$0.75^{+0.07}_{-0.07}$
2.65	1	$0p_{3/2}$	$0.29^{+0.04}_{-0.04}$	$0.23^{+0.04}_{-0.04}$	$0.26^{+0.08}_{-0.03}$	$0.26^{+0.06}_{-0.04}$
$3.40^{(-)}$	1	$0p_{3/2}$	$0.47^{+0.08}_{-0.08}$	$0.36^{+0.07}_{-0.06}$	$0.41^{+0.17}_{-0.03}$	$0.41^{+0.10}_{-0.06}$
$3.40^{(+)}$	2	$0d_{3/2}$	$0.22^{+0.02}_{-0.02}$	$0.17^{+0.02}_{-0.02}$	$0.21^{+0.03}_{-0.01}$	$0.20^{+0.02}_{-0.02}$

Table 5.2 Spectroscopic factors extracted from the measured angular distributions using DWBA calculations for neutrons with transferred angular momentum ℓ to the single-particle state $n\ell j$. The listed optical model potentials were used in the incoming channel. The reported spectroscopic factors used the beam energy at the midpoint of the detector while their upper and lower limits used the beam energies at the window and micromegas, respectively.

			S_{th}		
E_x (MeV)	J^π	S_{exp}	WBT	YSOX	FSU
0	$1/2^+$	0.72 ± 0.04 [1], 0.77 [9], 0.73 ± 0.06 [10]	0.45	0.77	0.79
0.32	$1/2^-$	0.62 ± 0.04 [1], 0.96 [9], 0.62 ± 0.15 [10]	0.46	0.72	0.67
1.78	$5/2^+$	0.58(8) [8], 0.50 [9]	0.45	0.70	0.56
2.65	$3/2^-$	≈ 0.12 [8]	0.09	0.11	0.14
3.40	$3/2^-$	≈ 0.05 [8]	< 0.01	< 0.01	0.02
	$3/2^+$	0.10(1) [8]	0.05	0.16	0.02

Table 5.3 Spectroscopic factors from other experiments and those theoretically calculated using shell-model interactions. The factors reported from [1] are an average of those found. The author thanks Alex Brown for providing the WBT, Cenxi Yuan for the YSOX, and Rebeka Lubna for the FSU calculations.

calculations. Within the given range, the factor for the ground state is in agreement with the previous measurements. In the DWBA calculations, the shape of the ground state distribution changed significantly as a function of the incident energy, resulting in the large range of values. The 0.32 spectroscopic factor is also in agreement with the literature. However, those for the 1.78 MeV, 2.65 MeV, and 3.40 MeV states are all larger than the reported values.

In general, all the derived factors are larger than the values predicted by the WBT shell model interaction. However, the spectroscopic factors of the first four states are in reasonable

agreement with the YSOX and FSU interactions. The spectroscopic factor for the 3.40 MeV state is complicated. Not enough points near a minima were measured by the experiment to determine the parity from the shape of the distribution. The reported reduced chi-squared values are close when fitting the DWBA calculations for the midpoint of the AT-TPC to the data, although the positive parity assignment is preferred (see Fig. 5.8). Spectroscopic factors were then derived for this state for each parity. Two observations are made. First, the negative parity results in a seemingly much too large factor when compared to previous measurements and theory. Second, the factor for the positive parity is near that predicted by the YSOX interaction. Both of these results, while not as direct as a measurement of the shape of the angular distribution, are consistent with a positive parity assignment to the 3.40 MeV state. Of the three shell-model interactions, the YSOX interaction does the best in reproducing the experimentally derived spectroscopic factors.

With the experimentally derived spectroscopic factors, the ESPE of the $0d_{3/2}$ orbital in ^{11}Be can be roughly estimated. Since only one $3/2^+$ state is definitively observed up to 4 MeV, only a lower limit can be provided for the ESPE. The assumption is made that the unobserved spectroscopic strength is in the 3.89 MeV state. Performing the spectroscopic weighted average of the energies of the 3.40 MeV and 3.89 MeV states yields $3.79^{-0.01}_{+0.01}$ MeV (the superscript used the spectroscopic factor at the window while the subscript used the factor at the micromegas). This same procedure can be done for the ESPE of the $0d_{5/2}$ orbital producing $2.32^{-0.15}_{+0.14}$ MeV. The difference between these two ESPEs yields the strength of the spin-orbit splitting between the $0d$ orbitals in ^{11}Be, which is $1.48^{+0.14}_{-0.13}$ MeV.

This splitting can be compared to the ^{11}Be isotone ^{13}C. Most of the ^{13}C $0d_{5/2}$ strength resides in its 3.85 MeV and 6.86 MeV states [38]. Considering only them, the spectroscopic factors of Darden *et al.* yield a $0d_{5/2}$ ESPE of 4.51 MeV [38]. Darden *et al.* also measured all the $0d_{3/2}$ strength in the 8.40 MeV state for a $0d_{3/2}$ ESPE of 8.40 MeV. The spin-orbit splitting of the $0d$ orbitals in ^{13}C is found to be 3.89 MeV. Although this experiment could only measure a lower limit, the orbital splitting in ^{11}Be appears much smaller. This might be evidence for a reduction of the $0d$ splitting in the $N = 7$ isotones. A similar phenomenon has been reported for the $0p$ orbitals in

the $N = 17, 19, 21$ isotones [39].

CHAPTER 6

CONCLUSION

This thesis experiment successfully measured the ^{10}Be(d, p) reaction with the AT-TPC. Importantly, it marks the detector's first measurement of a transfer reaction in inverse kinematics. Angular distributions for the first five states of ^{11}Be were measured along with those from elastic and inelastic scattering on the deuterium gas. This is a highlight of AT-TPC transfer reaction studies: the incoming elastic and inelastic channels are recorded for free to constrain the OMP of the incoming channel for reaction calculations. Incidentally, this ^{10}Be(d, d') data also led to the identification of a new 1^- resonance at 7.27 MeV in ^{10}Be [40]. It can be seen in Fig. 5.2 as the hot band near 40° under 5 MeV.

Comparisons of the measured ^{11}Be angular distributions with theoretical DWBA calculations revealed nuclear structure details such as spectroscopic factors, which were compared to those in the literature and calculations from various theoretical shell-model interactions. The derived factors generally agree with the literature and calculations of the YSOX interaction. Despite the inability to definitively assign a parity to the 3.40 MeV state in ^{11}Be, evidence was produced in support of a positive parity. This would place the 3.40 MeV state as the second member of a $K^P = 1/2^+$ rotational ground state band, as predicted by *ab initio* calculations from Caprio *et al.* [14], and a lower limit of $3.79^{-0.01}_{+0.01}$ MeV on the $0d_{3/2}$ ESPE. The simultaneous measurement of the majority of the $0d_{5/2}$ strength allowed a lower limit on the spin-orbit splitting of the $0d$ orbitals in ^{11}Be to be calculated, which was found to be less than its $N = 7$ isotone ^{13}C. This might be evidence for the evolution of the spin-orbit splitting of these isotones.

The success of this experiment has paved the way for a new era of AT-TPC transfer experiments. Some of these have already been completed, such as ^{15}C+d and ^{15}C+p measurements at Argonne National Laboratory, and some are yet to come. However, it also provides a means for future improvements. Ultimately, the angular distribution of the 3.40 MeV state is too limited. A lack of statistics cut off larger CM angles where the cross section is small. This cutoff was worsened by the inability of the Spyral analysis to measure protons scattered near 90°. Small CM angles also

faced restrictions. The beam energy of this experiment was too low to allow for the protons at the smaller CM angles to have sufficient energy to exit the beam region of the AT-TPC and be detected. A higher beam energy would also have allowed for the population of higher-lying states for a better determination of the ESPEs of the $0d$ orbitals.

Except for analyzing protons nearly perpendicular to the beam, the other two problems have straightforward solutions. They would be fixed by increasing the requested beam time with a beam of higher energy. Unfortunately, beam time is a valuable commodity in high demand. That said, there may be an avenue to increase the effective statistics of the AT-TPC given the same beam time. The AT-TPC was limited to events with only one incoming beam particle (see Section 2.3). This resulted in a significant loss of 66% of all the recorded experimental data. Even reducing this loss by a factor of two would have nearly doubled the amount of data used in this thesis experiment's analysis. The implementation of auxiliary detectors might be able to achieve this goal. Currently, the use of a 0° silicon detector on the beam axis for this purpose is being investigated. An increase in the statistics would also have allowed for a more accurate extraction of spectroscopic factors. The cross sections could then be binned as a function of energy instead of having their energy dependence integrated out (see Section 5.5).

^{11}Be is a nucleus that exhibits some of the most interesting known phenomena in nuclei, including a neutron halo ground state and level inversion. This nucleus is deserving of a more advanced theoretical analysis than what has been provided in this thesis to capture these features. Such an analysis should go beyond DWBA calculations to include deuteron breakup and continuum effects, both of which can be modeled in adiabatic distorted wave approximation calculations. The continuum effects can also be introduced in coupled channels Born approximation calculations, with the measured elastic and inelastic distributions fit to determine the OMP for the incoming channel. With the angular distributions measured by this thesis, these advanced calculations can be done and are presently being explored by colleagues. The results will be published in a future paper, along with more in-depth comparisons to *ab initio* no-core shell model calculations.

Beyond the work presented here, it is my sincere hope that a future experiment is done to

provide a definitive assignment to the parity of the 3.40 MeV state of ^{11}Be. If it were to use the AT-TPC, we now know exactly how to accomplish this measurement.

BIBLIOGRAPHY

[1] K. T. Schmitt, K. L. Jones, S. Ahn, D. W. Bardayan, A. Bey, J. C. Blackmon, S. M. Brown, K. Y. Chae, K. A. Chipps, J. A. Cizewski, K. I. Hahn, J. J. Kolata, R. L. Kozub, J. F. Liang, C. Matei, M. Matos, D. Matyas, B. Moazen, C. D. Nesaraja, F. M. Nunes, P. D. O'Malley, S. D. Pain, W. A. Peters, S. T. Pittman, A. Roberts, D. Shapira, J. F. Shriner, M. S. Smith, I. Spassova, D. W. Stracener, N. J. Upadhyay, A. N. Villano, and G. L. Wilson, "Reactions of a ^{10}be beam on proton and deuteron targets," *Phys. Rev. C*, vol. 88, p. 064612, Dec 2013.

[2] J. Bradt, D. Bazin, F. Abu-Nimeh, T. Ahn, Y. Ayyad, S. Beceiro Novo, L. Carpenter, M. Cortesi, M. Kuchera, W. Lynch, W. Mittig, S. Rost, N. Watwood, and J. Yurkon, "Commissioning of the active-target time projection chamber," *Nuclear Instruments and Methods in Physics Research Section A: Accelerators, Spectrometers, Detectors and Associated Equipment*, vol. 875, pp. 65–79, 2017.

[3] K. Krane, *Introductory Nuclear Physics*. Wiley, 1987.

[4] K. Miura, T. Tohhei, T. Nakagawa, A. Satoh, T. Ishimatsu, T. Kawamura, K. Furukawa, M. Kabasawa, Y. Takahashi, H. Orihara, T. Niizeki, K. Ishii, and H. Ohnuma, "The 31p(d, n)32s reaction at 25 mev," *Nuclear Physics A*, vol. 467, no. 1, pp. 79–92, 1987.

[5] E. Pollacco, G. Grinyer, F. Abu-Nimeh, T. Ahn, S. Anvar, A. Arokiaraj, Y. Ayyad, H. Baba, M. Babo, P. Baron, D. Bazin, S. Beceiro-Novo, C. Belkhiria, M. Blaizot, B. Blank, J. Bradt, G. Cardella, L. Carpenter, S. Ceruti, E. De Filippo, E. Delagnes, S. De Luca, H. De Witte, F. Druillole, B. Duclos, F. Favela, A. Fritsch, J. Giovinazzo, C. Gueye, T. Isobe, P. Hellmuth, C. Huss, B. Lachacinski, A. Laffoley, G. Lebertre, L. Legeard, W. Lynch, T. Marchi, L. Martina, C. Maugeais, W. Mittig, L. Nalpas, E. Pagano, J. Pancin, O. Poleshchuk, J. Pedroza, J. Pibernat, S. Primault, R. Raabe, B. Raine, A. Rebii, M. Renaud, T. Roger, P. Roussel-Chomaz, P. Russotto, G. Saccà, F. Saillant, P. Sizun, D. Suzuki, J. Swartz, A. Tizon, A. Trifiró, N. Usher, G. Wittwer, and J. Yang, "Get: A generic electronics system for tpcs and nuclear physics instrumentation," *Nuclear Instruments and Methods in Physics Research Section A: Accelerators, Spectrometers, Detectors and Associated Equipment*, vol. 887, pp. 81–93, 2018.

[6] M. Baranger, "A definition of the single-nucleon potential," *Nuclear Physics A*, vol. 149, no. 2, pp. 225–240, 1970.

[7] R. Casten, *Nuclear Structure from a Simple Perspective*. Oxford University Press, 2001.

[8] H. T. Fortune and R. Sherr, "Neutron widths and configuration mixing in ^{11}Be," *Phys. Rev. C*, vol. 83, p. 054314, May 2011.

[9] B. Zwieglinski, W. Benenson, R. Robertson, and W. Coker, "Study of the 10be(d, p)11be reaction at 25 mev," *Nuclear Physics A*, vol. 315, no. 1, pp. 124–132, 1979.

[10] D. Auton, "Direct reactions on 10be," *Nuclear Physics A*, vol. 157, no. 1, pp. 305–322, 1970.

[11] G.-B. Liu and H. T. Fortune, "^{9}Be(t,p)^{11}be and the structure of ^{11}Be," *Phys. Rev. C*, vol. 42, pp. 167–173, Jul 1990.

[12] Y. Hirayama, T. Shimoda, H. Izumi, A. Hatakeyama, K. Jackson, C. Levy, H. Miyatake, M. Yagi, and H. Yano, "Study of 11be structure through β-delayed decays from polarized 11li," *Physics Letters B*, vol. 611, no. 3, pp. 239–247, 2005.

[13] N. Fukuda, T. Nakamura, N. Aoi, N. Imai, M. Ishihara, T. Kobayashi, H. Iwasaki, T. Kubo, A. Mengoni, M. Notani, H. Otsu, H. Sakurai, S. Shimoura, T. Teranishi, Y. X. Watanabe, and K. Yoneda, "Coulomb and nuclear breakup of a halo nucleus ^{11}Be," *Phys. Rev. C*, vol. 70, p. 054606, Nov 2004.

[14] M. A. Caprio, P. J. Fasano, P. Maris, A. E. McCoy, and J. P. Vary, "Probing ab initio emergence of nuclear rotation," *The European Physical Journal A*, vol. 56, p. 120, Apr. 2020.

[15] H. G. Bohlen, W. von Oertzen, R. Kalpakchieva, T. N. Massey, T. Dorsch, M. Milin, C. Schulz, T. Kokalova, and C. Wheldon, "Band structures in light neutron-rich nuclei," *Journal of Physics: Conference Series*, vol. 111, p. 012021, may 2008.

[16] E. K. Warburton and B. A. Brown, "Effective interactions for the 0p1s0d nuclear shell-model space," *Phys. Rev. C*, vol. 46, pp. 923–944, Sep 1992.

[17] C. Yuan, T. Suzuki, T. Otsuka, F. Xu, and N. Tsunoda, "Shell-model study of boron, carbon, nitrogen, and oxygen isotopes with a monopole-based universal interaction," *Phys. Rev. C*, vol. 85, p. 064324, Jun 2012.

[18] R. S. Lubna, K. Kravvaris, S. L. Tabor, V. Tripathi, A. Volya, E. Rubino, J. M. Allmond, B. Abromeit, L. T. Baby, and T. C. Hensley, "Structure of ^{38}Cl and the quest for a comprehensive shell model interaction," *Phys. Rev. C*, vol. 100, p. 034308, Sep 2019.

[19] G. McCann and N. Turi, "Attpc/spyral: v0.18.0 - update numba, spyral-utils," Feb. 2025.

[20] J. W. Bradt, *Measurement of isobaric analogue resonances of ^{47}Ar with the active-target time projection chamber*. PhD thesis, Michigan State U., 2017.

[21] P. Virtanen, R. Gommers, T. E. Oliphant, M. Haberland, T. Reddy, D. Cournapeau, E. Burovski, P. Peterson, W. Weckesser, J. Bright, S. J. van der Walt, M. Brett, J. Wilson, K. J. Millman, N. Mayorov, A. R. J. Nelson, E. Jones, R. Kern, E. Larson, C. J. Carey, İ. Polat, Y. Feng, E. W. Moore, J. VanderPlas, D. Laxalde, J. Perktold, R. Cimrman, I. Henriksen, E. A. Quintero, C. R. Harris, A. M. Archibald, A. H. Ribeiro, F. Pedregosa, P. van Mulbregt, and SciPy 1.0 Contributors, "SciPy 1.0: Fundamental Algorithms for Scientific Computing in Python," *Nature Methods*, vol. 17, pp. 261–272, 2020.

[22] R. J. G. B. Campello, D. Moulavi, and J. Sander, "Density-based clustering based on hierarchical density estimates," in *Advances in Knowledge Discovery and Data Mining* (J. Pei, V. S.

Tseng, L. Cao, H. Motoda, and G. Xu, eds.), (Berlin, Heidelberg), pp. 160–172, 2013.

[23] L. McInnes, J. Healy, and S. Astels, "hdbscan: Hierarchical density based clustering," *The Journal of Open Source Software*, vol. 2, mar 2017.

[24] G. McCann. Personal communication, 2023.

[25] F. Pedregosa, G. Varoquaux, A. Gramfort, V. Michel, B. Thirion, O. Grisel, M. Blondel, P. Prettenhofer, R. Weiss, V. Dubourg, J. Vanderplas, A. Passos, D. Cournapeau, M. Brucher, M. Perrot, and E. Duchesnay, "Scikit-learn: Machine learning in Python," *Journal of Machine Learning Research*, vol. 12, pp. 2825–2830, 2011.

[26] J. Dopfer. Personal communication, 2024.

[27] A. Prochazka and A. Hollands, "pycatima." https://github.com/hrosiak/pycatima.

[28] R. H. Byrd, P. Lu, J. Nocedal, and C. Zhu, "A limited memory algorithm for bound constrained optimization," *SIAM Journal on Scientific Computing*, vol. 16, no. 5, pp. 1190–1208, 1995.

[29] G. McCann and Z. Serikow, "Attpc/attpc_engine: v0.9.0 - critical bugfix, angular distributions," Mar. 2025.

[30] H. Schreiner, J. Pivarski, and S. Chopra, "vector," Jan. 2025.

[31] G. F. Knoll, *Radiation Detection and Measurement*. John Wiley, 2010.

[32] J. Giovinazzo, T. Goigoux, S. Anvar, P. Baron, B. Blank, E. Delagnes, G. Grinyer, J. Pancin, J. Pedroza, J. Pibernat, E. Pollacco, A. Rebii, T. Roger, and P. Sizun, "Get electronics samples data analysis," *Nuclear Instruments and Methods in Physics Research Section A: Accelerators, Spectrometers, Detectors and Associated Equipment*, vol. 840, pp. 15–27, 2016.

[33] M. H. Macfarlane and S. C. Pieper, "Ptolemy: a program for heavy-ion direct-reaction calculations. [cross sections, dwba]," tech. rep., Argonne National Lab., Ill. (USA), 04 1978.

[34] R. B. Wiringa, V. G. J. Stoks, and R. Schiavilla, "Accurate nucleon-nucleon potential with charge-independence breaking," *Phys. Rev. C*, vol. 51, pp. 38–51, Jan 1995.

[35] A. Koning and J. Delaroche, "Local and global nucleon optical models from 1 kev to 200 mev," *Nuclear Physics A*, vol. 713, no. 3, pp. 231–310, 2003.

[36] Y. Zhang, D. Y. Pang, and J. L. Lou, "Optical model potential for deuteron elastic scattering with $1p$-shell nuclei," *Phys. Rev. C*, vol. 94, p. 014619, Jul 2016.

[37] H. An and C. Cai, "Global deuteron optical model potential for the energy range up to 183 mev," *Phys. Rev. C*, vol. 73, p. 054605, May 2006.

[38] S. Darden, S. Sen, H. Hiddleston, J. Aymar, and W. Yoh, "Study of (d, p) reactions to unbound states of 13c and 17o," *Nuclear Physics A*, vol. 208, no. 1, pp. 77–92, 1973.

[39] J. Chen, B. Kay, C. Hoffman, T. Tang, I. Tolstukhin, D. Bazin, R. Lubna, Y. Ayyad, S. Beceiro-Novo, B. Coombes, S. Freeman, L. Gaffney, R. Garg, H. Jayatissa, A. Kuchera, P. MacGregor, A. Mitchell, W. Mittig, B. Monteagudo, A. Munoz-Ramos, C. Müller-Gatermann, F. Recchia, N. Rijal, C. Santamaria, M. Serikow, D. Sharp, J. Smith, J. Stecenko, G. Wilson, A. Wuosmaa, C. Yuan, J. Zamora, and Y. Zhang, "Evolution of the nuclear spin-orbit splitting explored via the 32si(d,p)33si reaction using solaris," *Physics Letters B*, vol. 853, p. 138678, 2024.

[40] J. Chen, Y. Ayyad, D. Bazin, W. Mittig, M. Z. Serikow, N. Keeley, S. M. Wang, B. Zhou, J. C. Zamora, S. Beceiro-Novo, M. Cortesi, M. DeNudt, S. Heinitz, S. Giraud, P. Gueye, C. R. Hoffman, B. P. Kay, E. A. Maugeri, B. G. Monteagudo, H. Li, W. P. Liu, A. Muñoz, F. Ndayisabye, J. Pereira, N. Rijal, C. Santamaria, D. Schumann, N. Watwood, G. Votta, P. Yin, C. X. Yuan, and Y. N. Zhang, "Near-threshold dipole strength in ^{10}Be with isoscalar character," *Phys. Rev. Lett.*, vol. 134, p. 012502, Jan 2025.